Very High Cycle Fatigue Behavior of Riblet Structured High Strength Aluminum Alloy Thin Sheets

Sebastian Stille

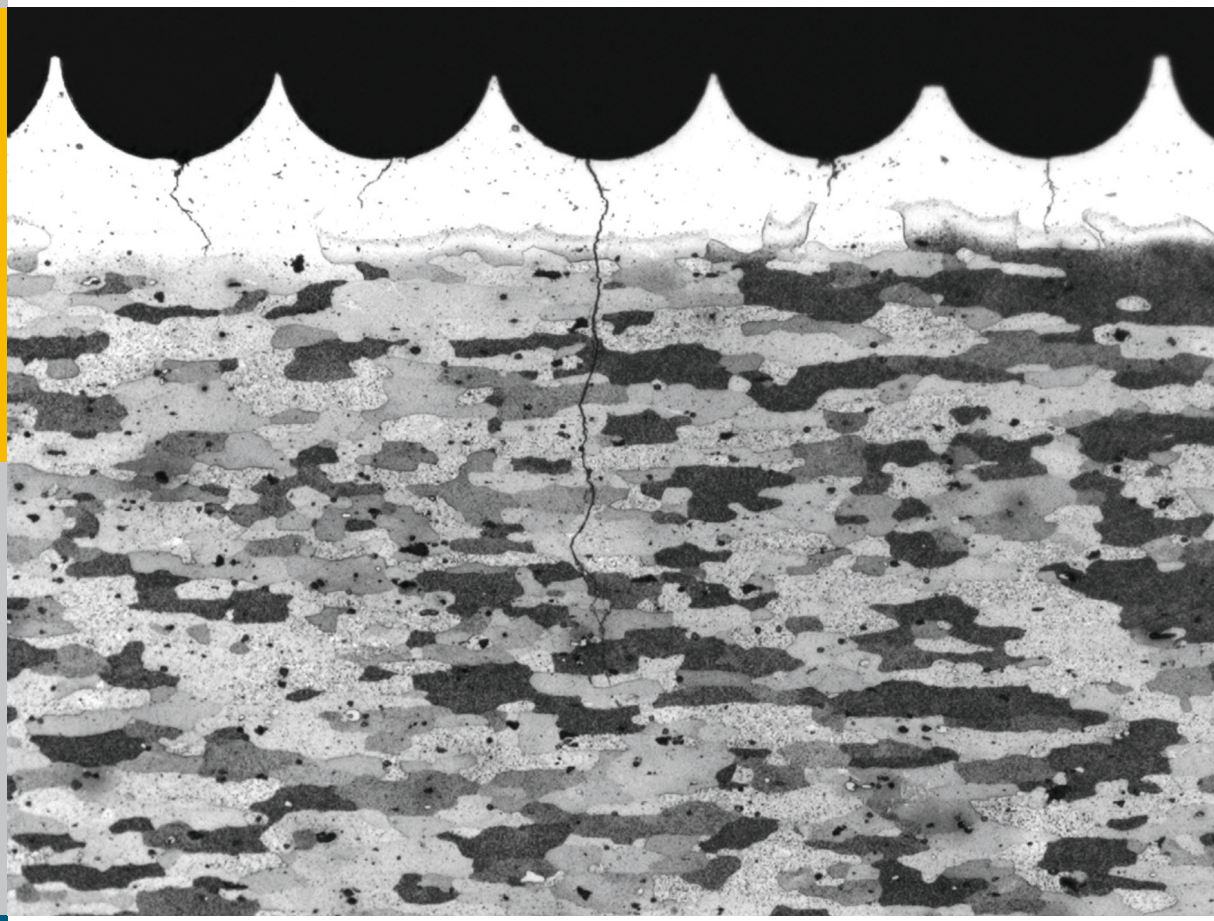

Member of the Helmholtz Association

Energie & Umwelt / Energy & Environment
Band / Volume 262
ISBN 978-3-95806-054-8

JÜLICH FORSCHUNGSZENTRUM

Schriften des Forschungszentrums Jülich
Reihe Energie & Umwelt / Energy & Environment Band / Volume 262

Forschungszentrum Jülich GmbH
Institute of Energy and Climate Research (IEK)
Microstructure and Properties of Materials (IEK-2)

Very High Cycle Fatigue Behavior of Riblet Structured High Strength Aluminum Alloy Thin Sheets

Sebastian Stille

Schriften des Forschungszentrums Jülich
Reihe Energie & Umwelt / Energy & Environment Band / Volume 262

ISSN 1866-1793 ISBN 978-3-95806-054-8

Bibliographic information published by the Deutsche Nationalbibliothek.
The Deutsche Nationalbibliothek lists this publication in the Deutsche Nationalbibliografie; detailed bibliographic data are available in the Internet at http://dnb.d-nb.de.

Publisher and Distributor: Forschungszentrum Jülich GmbH
Zentralbibliothek
52425 Jülich
Tel: +49 2461 61-5368
Fax: +49 2461 61-6103
Email: zb-publikation@fz-juelich.de
www.fz-juelich.de/zb

Cover Design: Grafische Medien, Forschungszentrum Jülich GmbH

Printer: Grafische Medien, Forschungszentrum Jülich GmbH

Schriften des Forschungszentrums Jülich
Reihe Energie & Umwelt / Energy & Environment, Band / Volume 262

D 82 (Diss. RWTH Aachen University, 2015)

ISSN 1866-1793
ISBN 978-3-95806-054-8

The complete volume is freely available on the Internet on the Jülicher Open Access Server (JuSER) at www.fz-juelich.de/zb/openaccess.

Abstract

Fatigue testing was performed on two age hardened high strength aluminum alloys (AA 2024 T351 and AA 7075 T6) at ultrasonic frequencies of around 20 kHz in fully reversed axial loading ($R = -1$). Tests were carried out on flat and riblet structured thin sheets in order to evaluate their usability for a novel technique for aerodynamic drag reduction as well as for gaining further insight into the relevant degradation and failure mechanisms. The studied riblets were of semi-circular geometry and produced by a flat rolling process which was developed at the Institute of Metal Forming (RWTH Aachen University). Important aspects of the present work are the influence of commercially pure CP Al claddings – which are frequently used for the prevention of corrosion – as well as of different riblet dimensions on the fatigue performance.

Whereas the bare material shows a continuous transition from high cycle fatigue (HCF) to very high cycle fatigue (VHCF), for clad sheets a sharp transition from HCF failure (up to some 10^6 cycles) to run-outs (at $\geq$ some 10^9 cycles) is observed. Particularly in the megacycle regime, the fatigue life of the structured bare material is – compared to the non-structured case – significantly reduced by stress concentrations induced by the surface structure. However, the fatigue performance of clad material is not negatively affected by the riblets. In this case, the threshold value at which the transition from HCF failure to run-outs occurs was even higher than in the flat case. The transition stress differs with cladding thickness as well as with riblet geometry. Fatigue cracks are – even in the case of run-outs – always initiated at the surface of the clad layer and grow easily to the substrate. Specimens only fail, if the threshold for further crack growth into the substrate is exceeded. The fatigue limit of both, the flat and riblet structured clad material can thus be described by a fracture mechanics approach using a Kitagawa-Takahashi diagram.

In the case of structured clad material, the threshold for fatigue failure is not only directly affected by the remaining thickness of the cladding below the riblet structure. Finite element (FEM) simulations demonstrate that due to plastic deformation a stress redistribution in the CP Al layer occurs which modifies the effective stress at the interface (cladding / substrate). The effective interface stress is thus as well a function of cladding thickness, which therefore, besides the direct effect, also indirectly influences the stress intensity of through-cladding cracks. Further FEM simulations demonstrate that riblets can be optimized with respect to VHCF performance, if the thickness of the clad layer below the riblet valleys is around 25% of the riblet diameter.

The failure mechanisms of both tested alloys are similar to each other. Further aspects covered in this work are a detailed analysis of material changes induced by

the structuring process and the development of a bending testing setup in which the loading conditions resemble the exposure during use in active drag reduction systems.

Inhaltsangabe

Die vorliegende Arbeit behandelt das Ermüdungsverhalten zweier ausscheidungsgehärteter, hochfester Aluminium-Legierungen (AA 2024 T351 und AA 7075 T6). Ermüdungsversuche wurden mittellastfrei ($R = -1$) bei einer Ultraschallfrequenz von ca. 20 kHz an flachen sowie ribletstrukturierten Blechen durchgeführt. Ziel der Arbeit ist zum einen eine Abschätzung der Verwendbarkeit derartiger Bleche im Zusammenhang mit einer neuartigen Methodik zur aktiven Luftwiderstandreduktion, zum anderen das Verständnis der relevanten Schädigungs- und Versagensmechanismen. Die untersuchten Ribletstrukturen haben eine halbkreisförmige Geometrie und wurden in einem am Institut für Bildsame Formgebung (RWTH Aachen) entwickelten Flachwalzprozess hergestellt. Wichtige Aspekte dieser Studie sind der Einfluss dünner Reinaluminium-Plattierschichten, wie sie üblicherweise zum Korrosionsschutz verwendet werden, sowie die Auswirkungen unterschiedlicher Ribletabmessungen auf das Ermüdungsverhalten.

Während unplattiertes Material einen gleichmäßigen Übergang vom Hochzyklus (HCF)- in den Ultrahochzyklus (VHCF) -bereich zeigt, wird für plattierte Proben ein scharfer Übergang zwischen HCF-Versagen (bis zu einigen 10^6 Lastwechseln) zu Durchläufern (bis $\geq$ mehrere 10^9 Lastwechsel) beobachtet. Insbesondere im HCF-Bereich wird die Ermüdungsfestigkeit des ribletstrukturierten, unplattierten Materials – im Vergleich zum Nichtstrukturierten – durch den Kerbeffekt der Oberflächenstruktur deutlich abgesenkt. Die Ermüdungsfestigkeit von plattiertem Material leidet jedoch keineswegs unter der Ribletstruktur, da in diesem Falle der Spannungsschwellwert für Materialversagen im Vergleich zum unstrukturierten Falle sogar leicht angehoben wird. Die Übergangsspannung hängt dabei sowohl von der Plattierschichtdicke, als auch von den Ribletabmessungen ab. Ermüdungsrisse werden – selbst bei Versuchen ohne Materialversagen – stets an der Oberfläche initiiert und breiten sich sehr einfach bis zur Grenzfläche (Substrat/Plattierung) aus. Materialversagen tritt nur dann auf, wenn die Schwelle für weiteres Risswachstum über die Grenzfläche hinaus überwunden wird. Das Ermüdungsverhalten sowohl von flachem, als auch von ribletstrukturiertem Material kann somit in einem bruchmechanischen Ansatz mithilfe eines Kitagawa-Takahashi-Diagramms beschrieben werden.

Neben dem direkten Einfluss der Plattierschichtdicke auf das Ermüdungsverhalten plattierten Materials kommt es zu einem weiteren, indirekten Einfluss der Plattierschichtdicke auf die effektiv am Grenzbereich (Substrat/Plattierung) herrschende Spannung, welcher in einer Spannungsumverteilung aufgrund plastischer Deformation der Plattierschicht begründet ist. Dieser Zusammenhang wird mittels finiter Elemente (FEM)-Simulationen eingehend untersucht. Weitere FEM-Berechnungen belegen, dass die Ribletstruktur hinsichtlich ihrer Ermüdungseigenschaften im VHCF-

Bereich optimiert werden kann, indem die unter den Riblettälern verbleibende Restdicke der Reinaluminiumschicht auf etwa 25% des Ribletdurchmessers eingestellt wird.

Die Versagensmechanismen beider untersuchten Legierungen ähneln sich stark. Weitere in dieser Arbeit angesprochene Aspekte sind Materialbeeinflussungen, welche aufgrund des Strukturierungsprozesses entstehen, sowie die Entwicklung einer Prüfeinrichtung für Wechselbiegeversuche, bei denen die Lastaufbringung einer Verwendung in aktiven Systemen zur Luftwiderstandsreduktion nachgebildet wird.

Acknowledgments

Firstly, I would like to thank Prof. Beck as well as Prof. Singheiser for the opportunity to work on this project. Furthermore, I am very grateful to Prof. Beck for the supervision and the support during this work. I would also like to thank Ms. Pöplau (IBF, RWTH Aachen University) for the structuring of the sheet material, Dr. Schiek and Mr. Silex (ZEA-2, FZ Jülich) for the corporation regarding bending testing, and finally Prof. Mayer and Dr. Schuller (BOKU Vienna) for helpful discussion and technical support concerning ultrasonic fatigue testing. This work was financially supported by the German Research Foundation (DFG, FOR 1779).

List of own related publications

Parts of the present work were published in international journals and presented on international conferences.

1. S. Stille, T. Beck, L. Singheiser, *Fatigue behavior of riblet structured high strength aluminum alloy thin sheets at very high cycle numbers*, submitted to Key Engineering Materials.

2. S. Stille, T. Beck, L. Singheiser, *Very high cycle fatigue behavior of riblet structured high strength Al alloy thin sheets*, 6th International Conference on Very High Cycle Fatigue, 15.–18. October 2014, Chengdu, China

3. S. Stille, T. Beck, L. Singheiser, *Influence of riblet geometry on fatigue life of surface structured AA 2024 thin sheets*, International Journal of Fatigue **68**, pp. 48–55 (2014).

4. J. Pöplau, S. Stille, T. Romans, T. Beck, L. Singheiser, G. Hirt, *The influence of process parameters on the forming of riblets during riblet rolling*, Key Engineering Materials **611–612**, pp. 715–722 (2014).

5. S. Stille, J. Pöplau, T. Beck, M. Bambach, G. Hirt, L. Singheiser, *Very high cycle fatigue behavior of riblet structured Alclad 2024 thin sheets*, International Journal of Fatigue **63**, pp. 183–190 (2014).

6. S. Stille, T. Beck, L. Singheiser, *Very high cycle fatigue behavior of riblet structured high strength Al alloy thin sheets*, 13th International Conference on Fracture, pp. 5160–5167, 16.–21. June 2013, Beijing, China

7. S. Kovacs, S. Stille, D. Ernstes, T. Beck, *Upgrading of an ultrasonic fatigue testing machine by means of early stage damage detection*, MP Materials Testing **55**, pp. 78–83 (2013).

Contents

1 Introduction and objectives

Drag reduction of modern transport systems, e.g. aircrafts, is beneficial for economical as well as for ecological reasons. In this regard, the total drag of an aircraft in cruise can be broken down into 5 basic contributions, as illustrated in Fig. 1.1. Having the highest contribution with 55% of the total drag, the viscous part according to Schrauf et al. [1] also has the highest potential for drag reduction of approx. 15%, achievable by laminar flow technology or turbulence and separation control techniques.

One promising approach to reduce the viscous drag of modern planes is the reduction of the frictional drag of their surfaces [1, 2]. Therefore, frictional drag reduction by passive and active methods has been subject of numerous studies since the 1960s [2]. One prominent example for passive methods are riblet structured surfaces [3, 4], which modify the turbulent boundary layer and thereby reduce the skin friction by up to 10 % [4]. The influence of the riblet geometry on drag reduction was studied in detail by Bechert et al. [4]: The highest efficiency is reached for a blade-like shape, followed by semi-circular, scalloped and sawtooth shaped riblets. For each given geometry, drag reduction is most efficient at a certain, well defined Reynolds number [4]. Consequently, riblet dimensions have to be adapted to the cruising speed of the aircraft and are therefore of limited flexibility if planes travel at different velocities during flight.

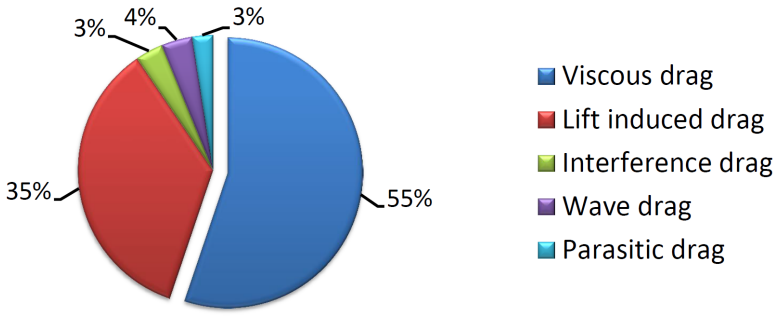

Figure 1.1: Drag breakdown of modern airplanes according to Schrauf et al. [1].

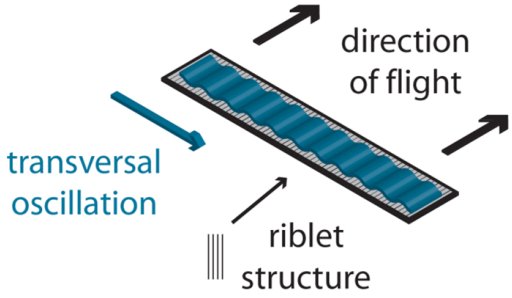

Figure 1.2: Illustration of loading conditions in an drag reduction system which combines active and passive methods.

During the last decade, active drag reduction by a transverse traveling surface wave has been investigated in detail [5]. In this approach, the surface oscillation reduces the movement of turbulent cells and thus stabilizes near-wall streaks [6, 7]. As reported by Itoh et al. [8], a drag reduction of 7.5% was achieved in wind channel experiments on a flat plate.

However, the surface oscillation with amplitudes of few 1/10 mm at frequencies of some 100 Hz raises the question of very high cycle fatigue (VHCF) failure as a possible technical limitation to this approach. The present work is part of a study funded by the German Research Foundation (FOR 1779) which aims for the combination of both, riblet structures as well as transverse traveling surface waves (cf. Fig. 1.2). Besides the aerodynamics of such an arrangement, the question of very high cycle fatigue has to be addressed in order to ensure safety and service reliability of such novel drag reduction systems. It is therefore required to evaluate the effects of structured surfaces on fatigue life of materials relevant for aircraft construction.

This study focuses on the fatigue properties of two high strength aluminum alloys: AA 2024 T351 and AA 7075 T6. Because of their high strength and their low density, wrought aluminum alloys of the 2000 and 7000 series are used extensively in the construction of airfoils and fuselages. Their fatigue properties were studied in detail several decades ago, e.g. by Schijve et al. [9] and Edwards et al. [10]. Nevertheless, these studies did not cover the VHCF regime which has been explored in the last 15 years after ultrasonic fatigue testing became more prevalent. The VHCF behavior of AA 2024 was subject to several studies [11–14], where a continuously decreasing S/N-curve up to 10^{10} cycles and thus no fatigue limit in the VHCF regime could be found. The same is true for AA 7075 as was proven e.g. by Mayer

et al. [15]. Therefore, VHCF testing is required in order to evaluate the influence of riblet surface structures on fatigue properties in the VHCF regime.

Due to their high sensitivity to corrosion, both tested alloys are frequently cladded with a layer of commercially pure (CP) aluminum. A negative consequence of this cladding is a significant reduction in fatigue performance as was demonstrated in [9, 10] for the range up to around $2x10^7$ load cycles. Nevertheless, the effect of claddings on the VHCF regime still remains an open question.

Therefore, beside the influence of riblet structures on the VHCF life, also the influence of CP Al claddings on thin sheets needs to be evaluated for both materials. These data provide an adequate basis for comparison of flat and riblet structured clad sheets. The same reference measurements are performed for bare material. Subsequently, a detailed analysis of the underlying damage mechanisms is conducted for all specimen types by optical and electron microscopy of fracture surfaces as well as of polished cross sections. The analysis is supported by finite element calculations. Furthermore, it is complemented by a study of material changes due to the riblet structuring process. Finally, the development of a bending fatigue setup ensures the comparability of the axial fatigue data with flexural loading in above mentioned active drag reduction systems.

2 Basics of fatigue

The term *fatigue* refers to material degradation during cyclic loading. It is therefore an important aspect with regard to service and safety of a variety of technical components. Hence, first considerations of fatigue date back to the 19th century [16]. Compared with this long timespan up to now, the so called *very high cycle fatigue* regime is a quite young field of research which emerged to a larger scale during the 1990s. Nevertheless, it has attracted considerable attention till today and has been subject of several international conferences [17]. To date, a variety of summarizing review papers appeared in literature which focus on different aspects of very high cycle fatigue [17–25]. The following chapter gives an introduction to the underlying theory of metallic fatigue in general and of the gigacycle regime in particular.

2.1 Fatigue of metals

In the course of service life, a large variety of technical components is exposed to cyclic loading. As a result, the material faces several structural changes within time. Figure 2.1 summarizes the typical stages of fatigue failure according to Mughrabi

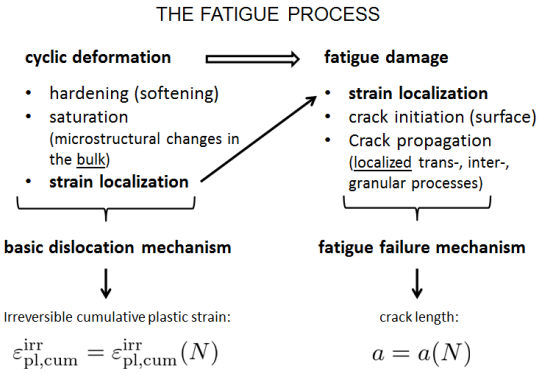

Figure 2.1: The different stages of the fatigue process according to Mughrabi [26]: cyclic deformation and fatigue damage. $\epsilon^{\mathrm{irr}}_{\mathrm{pl,cum}}$ is the irreversible fraction of cumulative plastic strain.

[26], which can briefly be summarized as follows: Within a relatively short time-span compared to the total lifetime, cyclic hardening (or softening) occurs which is followed by a saturation [27]. During further loading, microstructural changes, like the movement of dislocations, occur which cause strain localization followed by micro crack initiation. Subsequently, these micro cracks further propagate and induce fatigue failure.

Depending on the applied stress amplitude and hence the resulting lifetime, one distinguishes between different regimes, which are referred to as *low cycle fatigue* (LCF), *high cycle fatigue* (HCF) and *very high cycle fatigue* (VHCF). The boundary between these regimes cannot strictly be assigned to a particular number of load cycles and depends on the material of interest. Typically, the boundary between LCF and HCF is at $\approx 10^5$ - 10^6 load cycles. Above 10^7 - 10^8 load cycles, one usually refers to the term VHCF.

In the LCF region, fatigue life is controlled by the macroscopic plastic strain amplitude. Typically, fatigue failure is induced by the formation of persistent slip bands (PSBs) which raise the surface roughness and thus locally increase the stress concentration. Consequently, fatigue cracks are initiated at the surface. The S/N-curve follows the Manson-Coffin law [28, 29], which reads as

$$\frac{\Delta\epsilon_{pl}}{2} \propto (N_f)^c \,, \tag{2.1}$$

with ϵ_{pl}: plastic strain amplitude, N_f: number of load cycles to failure, and c: material depended constant.

If the applied stress does not exceed the threshold for PSB formation, cyclic loading cannot result in the failure mechanism outlined above, which then leads to a horizontal S/N-curve in the HCF region. The corresponding threshold stress level is referred to as the conventional fatigue strength of the material.

2.2 Very high cycle fatigue

As pointed out by Bathias [18], the horizontal limit in the HCF region is not necessarily an ultimate one. Material failure is found as well at much higher numbers of load cycles. In this context, one usually distinguishes between two types of materials [17]. Type I materials are single phase and do not contain inclusions, whereas type II materials consist of multiple phases. Characteristic S/N-curves for both types are schematically drawn in Fig. 2.2. Whereas the characteristic trend in the LCF and HCF regime is the same for both, there are distinct differences in the VHCF regime.

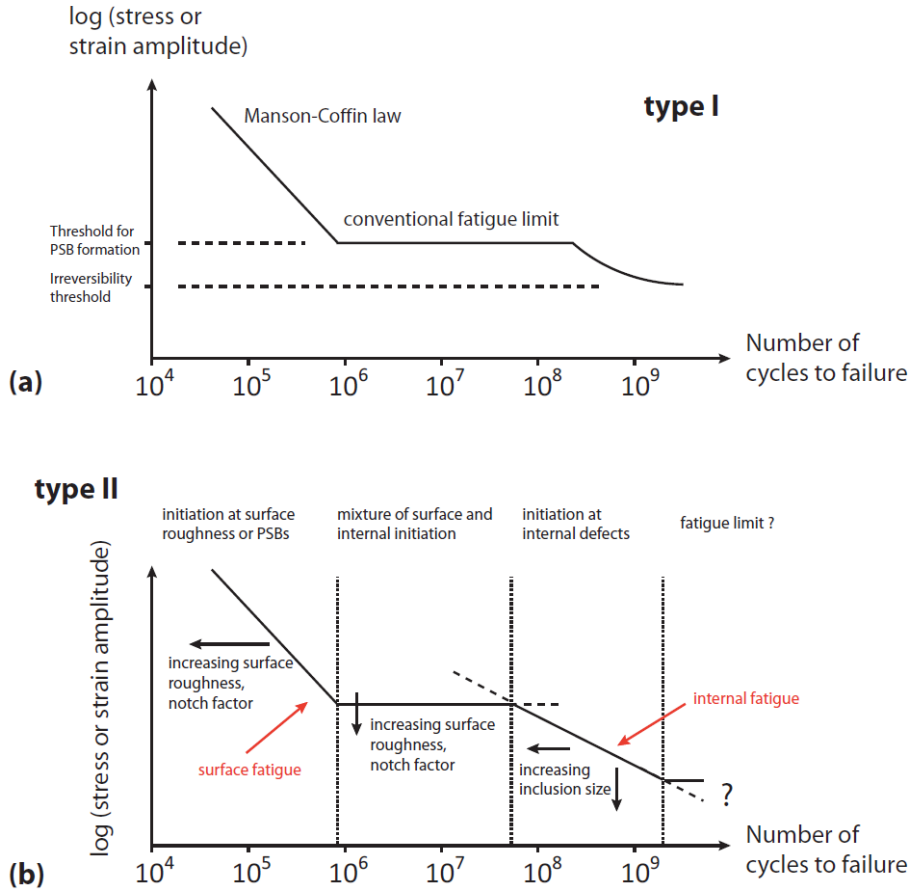

Figure 2.2: Schematic S/N-curves (a) type I materials [30]. (b) type II materials [20, 31, 32]. Position and slope of the curves depend on different influencing factors, the most important are mentioned in the graph.

The VHCF behavior of type I materials (cf. Fig. 2.2a) can be described using a model proposed by Mughrabi [17]. Below the PSB threshold, the applied stress is obviously insufficient to induce PSBs. Nevertheless, an accumulation of irreversible strain leads to an increase of surface roughness, which evolves with the number of load cycles and finally induces a local stress concentration which exceeds the PSB threshold. Such slip bands will only extend to a modest depth into the material. However, the cyclic strain becomes more localized. Consequently, the surface profile at the PSB site becomes gradually more accentuated during cyclic loading which

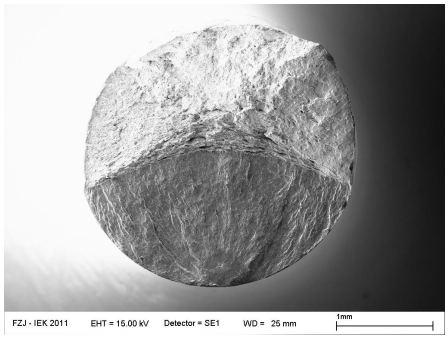

(a) Overview of the fracture surface. Crack initiation took place in the bottom part of the crack plane which exhibits a typical fish eye crack.

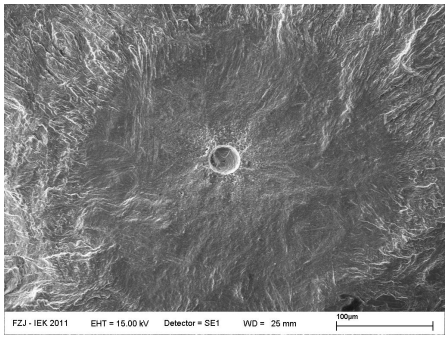

(b) Crack initiation region with optical dark area around the critical inclusion.

Figure 2.3: Fracture surface with typical fish-eye crack in a martensitic steel (X10CrNiMoV12-2-2) [33].

will extend the PSB deeper into the material and thus will lead to fatigue crack initiation. Nevertheless, if the applied stress lies below a certain irreversibility threshold, this mechanism can not occur and a true, ultimate fatigue limit can be expected.

The typical S/N-curve for type II materials is illustrated in Fig. 2.2b. In contrast to type I materials, fatigue cracks in the VHCF regime are typically initiated at internal defects like non-metallic inclusions. Therefore, a further decreasing S/N-curve is found above 10^7 load cycles. The transition from surface to internal fatigue is a characteristic feature of the VHCF behavior of type II materials. As presented in Fig. 2.2b, position and slope of the S/N-curve depend on the size of the critical inclusion.

If internal failure occurs, the fracture surfaces often show a so-called 'fish-eye crack', which is predominantly observed in high strength steels [20, 23]. Figure 2.3 presents an exemplary fracture surface of a martensitic steel. The critical inclusion is surrounded by an 'optical dark area' (ODA), in literature sometimes also referred to as 'fine granular area' (FGA) or 'granular bright facet' (BGF). The formation mechanisms of ODAs are still not completely clarified. According to Murakami [34–36], non-metallic inclusions trap hydrogen in their vicinity which locally causes hydrogen embrittlement and thus leads to a rougher fracture surface near the inclusion. Another theory on ODA formation is the one from Shiozawa et al. [37] which ascribe ODA formation to the dispersive initiation of micro-cracks by decohesion of spherical carbides from the matrix around a non-metallic inclusion. During cyclic

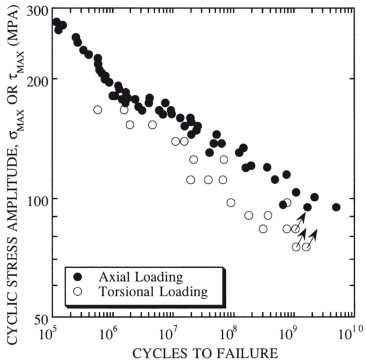

(a) S/N-curve for AA 2024 T351 [11].

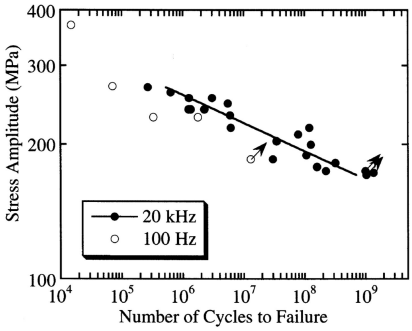

(b) S/N-curve for AlZnMgCu1.5 T6 [15] (similar to AA 7075).

Figure 2.4: S/N-curves for of two Al-sheet alloys.

loading, the micro-cracks coalesce with each other and form the ODA. Sakai [21] suggests the formation of a fine granular layer around the inclusion due to intensive polygonization. The number of micro-debondings is then increased gradually during cyclic loading and coalescence occurs. Subsequently, the micro-debondings are entirely spread over the fine granular layer and a penny-shape crack is formed around the interior inclusion. Finally, Grad et al. [38] propose that during cyclic loading, grain refinement in the inclusion's vicinity locally lowers the stress intensity threshold for crack propagation (cf. section 2.4, pp. 12 ff.). This way the crack can grow along the FGA until it finally reaches the global stress intensity threshold value.

2.3 Fatigue of aluminum sheet alloys

High strength aluminum sheet alloys are a typical type II material. Their fatigue behavior has been subject to various studies, dating back several decades. Grosskreutz and Shaw [39] stated that for $N_f \approx 10^5$ - 10^6 fatigue crack nucleation in AA 2024 and AA 7075 occurs between surface inclusions, which are basically hard intermetallic compounds containing primarily Fe and Si, and the surrounding matrix. Systematic measurements of the S/N-curves of high strength aluminum alloys were performed up to $N_f \approx 10^7$ by Schijve and Jacobs [9], Williams and Sova [40], and Edwards et al. [10] in the subsequent years.

After ultrasonic fatigue testing systems became more prevalent in the late 1990s, further studies were performed, exceeding the previous limitations of testing cycles.

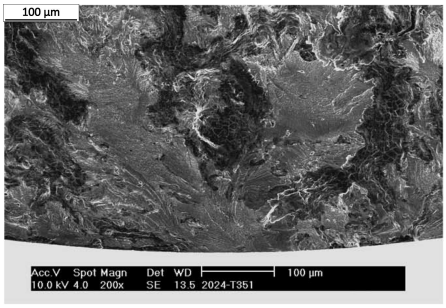

(a) Fracture surface produced by tension-compression ultrasonic cycling. ($\tau_{max} = 130$ MPa, $N = 2.32\text{x}10^8$ cycles). The image shows the crack initiation area.

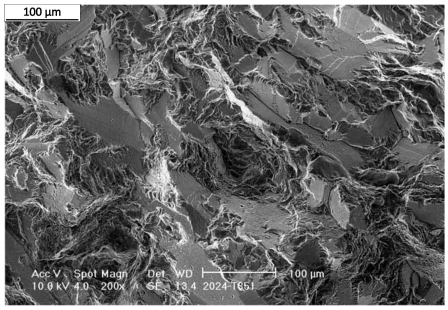

(b) Magnification of (a) at a distance of 1 mm from the crack initiation site.

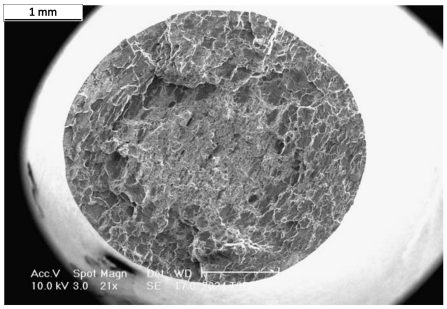

(c) Circumferential fatigue crack with depth 1–1.2 mm produced by cyclic torsion ($\tau_{max} = 150$ MPa, $N = 1.94\text{x}10^6$ cycles) and static fracture (center area).

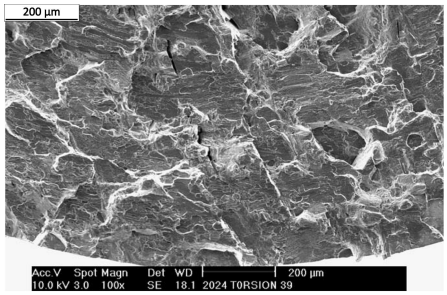

(d) Fracture surface produced by ultrasonic cyclic torsion at low stress ($\tau_{max} = 81.6$ MPa, $N = 1.06\text{x}10^9$ cycles).

Figure 2.5: Fracture surfaces for AA 2024 T351 under different loading conditions [41]. (a) and (b) Axial loading. (c) and (d) Torsional loading.

First fatigue tests on AA 2024 up to 10^{10} load cycles were performed by Mayer and Stanzl-Tschegg [11, 42, 43]. Fatigue failure was observed beyond a few 10^7 load cycles, which is the ultimate cycle number in most earlier studies on fatigue life. Consequently, the S/N-curve does not approach a horizontal limit but is decreasing up to at least 10^{10} load cycles. Ultrasonic fatigue testing on AA 7075 was performed in another study by Mayer at al. [15]. Similarly, no fatigue limit was found up to 10^9 load cycles. S/N-curves for both alloys are presented in Fig. 2.4.

Whereas the early work by Grosskreutz and Shaw [39] on AA 2024 argues that the formation of slip bands has no significant influence on fatigue crack initiation for

$N_f \approx 10^5$ - 10^6, Marines et al. [19] demonstrated that for $N_f < 10^6$, crack initiation in AA 2024 is related to slip bands whereas for $N_f > 10^6$ it is related to inclusions. Mayer et al. [14] stated that cracks in AA 2024 in the VHCF regime are initiated at or slightly below the surface at broken constituent particles or at agglomerations of fractured particles. For AA 7075, fatigue cracks originate as well basically from surface near constituent particles as proven by Harlow et al. [44].

Contrary to high-strength steels, the aluminum alloys studied in this work do not show fish-eye cracks. Typical fracture surfaces of AA 2024 T351 for different load types are presented in Fig. 2.5. The following descriptions are mainly from the study by Mayer [41], where also the images were taken from. (a) and (b) show a fracture surface for axial loading. The crack initiation area (a) exhibits a transcrystalline fracture with low ductility. No crack initiation with a path in direction of maximum shear is visible but the crack initiation fracture surface is oriented perpendicular to the specimen's axis, i.e. along the maximum normal stress. Furthermore, crack initiation is at the surface, which, according to [41], was found in numerous other investigated specimens that failed in the regime of load cycles between 10^5 and 10^9. A typical feature of the fracture surfaces are oxides close to the initiation location, which appear black in the image. Figure 2.5b presents a magnification of the fracture surface at a distance of 1 mm from the crack initiation site. Crystallographic cleavage fracture is visible, which is not oberserved at the crack initiation location. Furthermore, the fracture surface appears much rougher in high magnification.

At torsional loading (cf. Fig. 2.5c and d), the fracture has similar features as in axial loading, even though the fracture surface looks different than before. The fatigue fracture regime in (c) is almost circular-symmetric starting from the surface. The center region shows static fracture, which was obtained by rupturing the specimen after testing. Figure 2.5d shows in more detail the fatigue fracture surface of a specimen which failed at relatively low stress amplitude. The fracture surface reflects the preferential growth of fatigue cracks in the directions of maximum shear: Mainly transgranular crack propagation in circumferential direction as well as cracks in longitudinal direction (perpendicular to the fracture surface) are visible.

Fracture surfaces for AA 7075 T651 are presented in the study by Bonakdar et al. [45]. They are much more cleavaged, showing a more brittle fracture behavior compared to AA 2024. On page 16 of the present work, two fracture surfaces of AA 7075 T6 for different environmental conditions from [15] are provided in Fig. 2.11.

Due to their constituent elements, the 2000 and 7000 aluminum alloy series are quite sensitive to corrosion and therefore frequently combined with a thin clad layer of commercially pure (CP) aluminum. The influence of the claddings on fatigue life was already investigated in the above mentioned early studies by Schijve and Jacobs

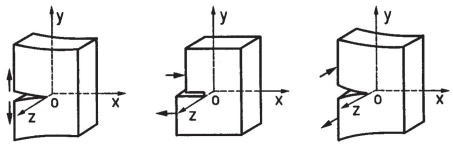

Figure 2.6: The three basic modes of crack extension [47]. (left) Opening, mode I (center) Sliding, mode II (right) Tearing, mode III.

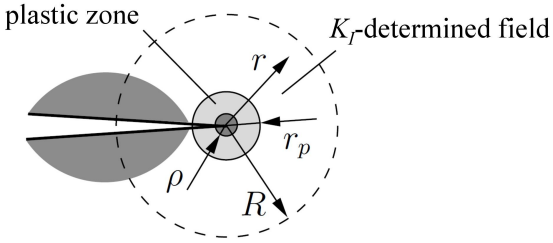

Figure 2.7: Dimensions for validity of LEFM, including the concept of stress intensity factors: Crack tip with plastic zone [48].

[9], Williams and Sova [40], and Edwards et al. [10], which found a significantly reduced fatigue performance compared to bare sheets. A detailed analysis of the different stages of fatigue of clad AA 2024 sheets was performed by Hunter and Fricke [46], which demonstrated that fatigue cracks are, at an early stage of around 1 % of fatigue life, initiated in the cladding and subsequently grow into the substrate where they induce failure.

2.4 Fracture mechanics and fatigue crack growth

In fracture mechanics, one distinguishes between 3 basic crack extensions modes, i.e. opening (mode I), sliding (mode II) and tearing (mode III). A graphical illustration of the modes is provided in Figure 2.6. More complex loading can be described by superpositions of the basic modes. If the plastic zone at the crack tip is small compared to the crack dimensions, the conditions for linear elastic fracture mechanics (LEFM) hold and cracks can be characterized by their stress intensity factor. The validity of the stress intensity field described by LEFM – as illustrated in detail in Fig. 2.7 – is limited to distances $r_p < r < R$ from the crack tip, where r_p is the size of the plastic zone and R the outer range, beyond which higher order terms are no longer negligible. Considering the size of the plastic zone, the condition for applying LEFM can be expressed as $r_p \ll R$.

For a mode I crack (crack tip opening), the stress intensity is calculated as

$$K_I = Y\sigma\sqrt{\pi a}, \tag{2.2}$$

with Y: geometry factor, σ: applied stress normal to the crack direction, and a: crack length. A detailed introduction into the theory of fracture mechanics as well as a

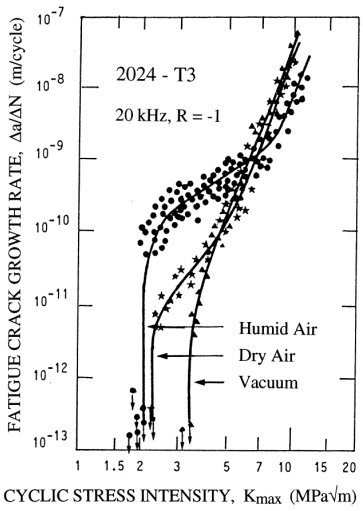

(a) AA2024 T351 [11].

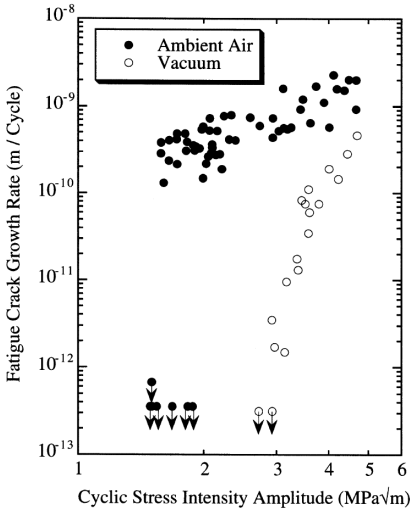

(b) AlZnMgCu1.5 T6 [15] (similar to AA 7075).

Figure 2.8: Fatigue crack growth curves and influence environment at ultrasonic testing frequency.

list of geometry factors can be found in [47–50]. Experiments on crack growth of AA 2024 T3 and AA 7075 T6 were performed already in the study of Paris et al. [51], where the so called Paris law was developed for mode I cracks, which describes the medium range of fatigue crack growth curve as

$$\frac{da}{dN} = C\,(\Delta K)^m\,, \tag{2.3}$$

with C and m: material depending constants. More recently, fatigue crack growth data for AA 2024 T3 were provided by Mayer [43] and Stanzl-Tschegg [11], as presented in Fig. 2.8a. This curve shows typical fatigue crack growth for metals. As can be seen, for a finite crack growth rate, a certain threshold value ($K_{\mathrm{max,\,th}}$) has to be overcome. For medium stress intensities, according to the Paris law, the curve is linear in the double-logarithmic plot. For higher stress intensities, crack propagation accelerates strongly until unstable crack propagation as the fracture toughness (K_{c}) is reached. Measurements on AlZnMgCu1.5 T6 were performed in another study by Mayer [41]. A similar behavior, but a much higher scatter of the threshold value $K_{\mathrm{max,\,th}}$ was observed (cf. Fig. 2.8b).

Whether fatigue cracks propagate or not can be illustrated by a plot of stress amplitude vs. crack length (cf. Fig. 2.9). This kind of graph is, in the case of double-

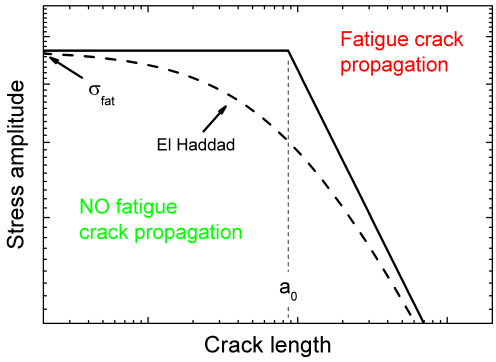

Figure 2.9: Kitagawa-Takahashi diagram, which separates the σ-a space into two regions. For short cracks and low stress amplitudes, fatigue cracks do not propagate. For longer cracks and higher loadings, crack propagation induces fatigue failure.

logarithmic axes, referred to as Kitagawa-Takahashi diagram [52]. It separates the region of fatigue crack growth from the region without fatigue failure. For cracks shorter than an material dependent, intrinsic crack length a_0, the region without failure is limited by the fatigue strength of the material. The intrinsic crack length is calculated as

$$a_0 = \frac{1}{\pi}\left(\frac{K_{\mathrm{max,th}}}{Y\sigma_{\mathrm{fat}}}\right)^2. \tag{2.4}$$

For microstructurally long cracks ($a > a_0$), the threshold level for fatigue crack growth is

$$\sigma_{\mathrm{th}} = \frac{K_{\mathrm{max,th}}}{Y\sqrt{\pi a}}, \tag{2.5}$$

i.e. the stress threshold is decreasing for longer cracks (cf. Fig. 2.9). The region between short and long crack growth can be described by the approximation proposed by El Haddad et al. [53]. The threshold level for crack growth is then

$$\sigma_{\mathrm{th}} = \frac{K_{\mathrm{max,th}}}{Y\sqrt{\pi(a+a_0)}}, \tag{2.6}$$

where a_0 is calculated according to equation 2.4.

2.5 Factors influencing fatigue behavior

Fatigue performance is influenced by a variety of factors, which will be discussed in the following. When comparing data from different setups, similar conditions for experimental conduction need to be ensured. If one considers for example the early contributions from the 1960s and 70s, the S/N-curves are generally lower

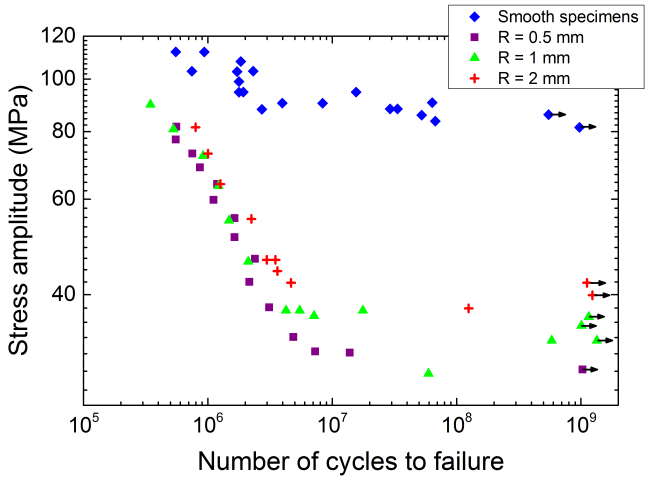

Figure 2.10: Notch effect on AA 2024 T4 for blunt notches with different radii. Experimental data from the study by Li et al. [12].

than in the more recent contributions. This can be attributed to improvements in testing methodology or sample preparation, but also to improvements of the alloy itself. Nevertheless, also a direct comparison of recently published S/N-data yields strong discrepancy for more or less comparable measurements. Consequently, possible influence factors have to be carefully controlled when conducting fatigue experiments and furthermore, own reference data should be acquired.

2.5.1 Notches

Since mechanical components usually are notched, the testing of notched specimens is an important aspect in fatigue research. The theoretical framework for the stress concentration in notched specimens was established by Neuber [54] in the 1930s. Likewise, notches already were an issue in the early contributions by Schijve and Jacobs [9], Williams and Sova [40], and Edwards et al. [10], where a significantly reduced fatigue strength of notched specimens was observed. Fatigue notch factors for sharp and blunt notches have been predicted analytically by Du Quesnay et al. [55]; for sharp notches based on short crack fracture mechanics, for blunt cracks based on Neuber's rule [54]. The predicted values are in good agreement with fatigue experiments on AA 2024 T351, provided in the same study. Whereas at the fatigue limit the fatigue notch factor increases with notch size for sharp notches, for blunt notches no notch-size effect was observed. More recently, Li et al. [12] measured S/N-curves for bluntly notched AA 2024 T4, which are presented in Fig. 2.10. Notches significantly reduce the fatigue performance of the specimens. Furthermore, contrary to the findings by Du Quesnay, a slight effect of the notch

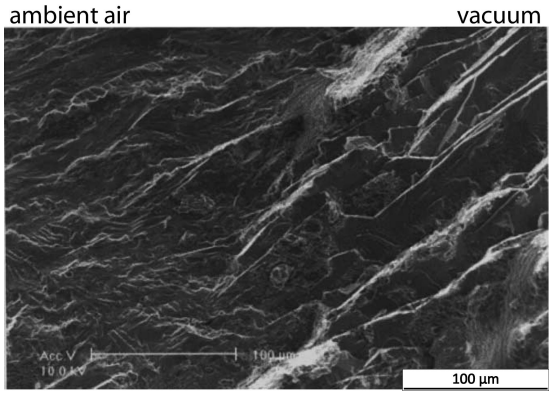

Figure 2.11: Influence of surrounding atmosphere on fracture surfaces of AA 7075 T6 at a cyclic stress intensity amplitude of 3.5 MPa$\sqrt{\text{m}}$ [15].

size could be observed. Talia and Talia [56] performed experiments on clad, surface scratched AA 2024 T3 sheet material up to 2x10^6 load cycles. Besides the fact that scratches significantly reduce fatigue lifetime also in this case a clear size effect of the notches was found.

One technically important reason for the occurrence of notches is localized corrosion (pitting), whose influence on fatigue was studied by Dolley et al. [57] on AA 2024 T3. Experiments on pre-corroded AA 7075 T6 were performed by Sakaran et al. [58], Wang et al. [59], as well as by Genel [60]. In all cases, a significant drop in lifetime occurred. Further publications with similar findings on notch effects on fatigue life of other aluminum alloys are e.g. the studies by Zimmermann and Christ [61], Pyttel et al. [62], and Berger et al. [63].

2.5.2 Surrounding atmosphere and testing frequency

Fatigue crack propagation rates might as well depend on the surrounding atmosphere. The surrounding atmosphere induces time dependent damage mechanisms at the crack tip, like surface diffusion of liquids or build up of a gaseous monolayer might have an influence [64]. As demonstrated by Stanzl-Tschegg [11] for AA 2024 tested at 20 kHz, these effects play a role exclusively in the threshold regime, i.e. for $\Delta a/\Delta N \leq 10^{-9}$ m/cycle, where the exposure times are sufficiently long for a detrimental interaction of the crack tip and the environment.

A similar study by Stanzl [65] on AA2024 T3, which compares fatigue crack growth rates in humid air ($\approx 50\%$ relative humidity), dry air (obtained by using liquid nitrogen as cooling trap and silicagel crystals) and vacuum ($P < 10^{-1}$ Pa) yields different crack propagation curves as presented in Fig. 2.8a. Both, the shape of the curves as well as the corresponding threshold values depend on the surrounding

atmosphere. Furthermore, fracture surfaces are less rough and show more signs of brittle failure after crack propagation in humid air than in vacuum [65]. Therefore, the higher fatigue crack growth rates in the plateau region are attributed to hydrogen embrittlement [65]. Comparing these data to fatigue experiments performed at 35 Hz [66], the plateau region in Fig. 2.8a lies lower by around one order of magnitude, which can be ascribed to surface diffusion of water vapour to the crack tip [11]. Crack propagation curves for AA 7075 T6 at ultrasonic frequencies in different environmental conditions (cf. Fig. 2.8b) yield a similar behavior as for AA 2024 [15].

The influence of the surrounding atmosphere raises the question of the comparability of ultrasonic and conventional fatigue tests. This is an important issue to address, since the loading frequency in most technical applications is clearly below the ultrasonic regime and fatigue tests are basically performed at higher frequencies in order to reach very high cycle numbers within a reasonable time. Nevertheless, as shown for example by Mughrabi [17, 30, 67], fatigue crack initiation becomes more and more important at larger fatigue lives. Therefore, fatigue life in the VHCF regime is dominated by crack initiation and not by crack propagation and thus fatigue testing at ultrasonic frequencies is comparable to testing at conventional frequencies. The compatibility of fatigue tests at conventional (35 Hz) and ultrasonic frequencies (20 kHz) was recently demonstrated e.g. by Xue et al. [68] for a cast Al-Si-Cu alloy.

2.5.3 Residual and mean stress

Plastic deformation during cold working usually induces residual stresses which can strongly influence fatigue life [69], as reviewed in various studies [70–72]. If components embody residual stress, loadings are superimposed to the residual stress field. This can be accounted for by a linear superposition approach, were the stress intensity factor calculates as

$$K_{\max} = (K_{\max})_L + (K)_R, \tag{2.7}$$

$$K_{\min} = (K_{\min})_L + (K)_R, \tag{2.8}$$

with $\left(K_{\max/\min}\right)_L$: stress intensity factor resulting from external loading and $(K)_R$: stress intensity factor associated with the initial pre-existing residual stress field [69]. This shift in stress intensity range shifts as well the stress ratio R, which is defined as

$$R = \frac{\sigma_{\min}}{\sigma_{\max}} = \frac{K_{\min}}{K_{\max}}. \tag{2.9}$$

If one considers crack propagation in residual stress fields, this quite simple superposition approach does not take into account stress redistribution caused by cracks

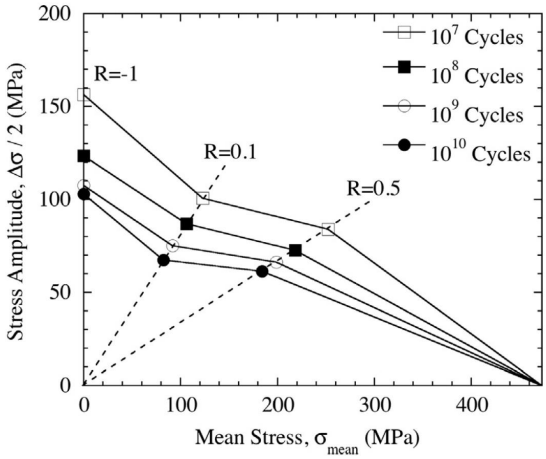

Figure 2.12: Haigh diagramm from the study of Mayer et al. [14] for AA 2024 T351 illustrating the influence of mean stress on fatigue life.

in the material. Nevertheless, as has been shown by LaRue and Daniewicz [69] by performing FEM simulations on AA2024 T351, this approach is quite accurate to describe the retardation of the crack growth due to residual stresses. Furthermore, the influence of stress redistribution induced by the crack itself has only a negligible effect on fatigue life [69, 73] and thus the superposition approach can be considered as a good approximation of the influence of residual stresses.

A quite general approach for taking into account residual stresses is the one from Smith, Watson and Topper [74], where residual stresses are considered as mean stress. This requires that residual stresses are stable during exposure to external loading. The corrected stress then calculates as

$$\sigma_{\text{S.W.T.}} = \sqrt{\sigma_a \left(\sigma_a + \sigma_m\right)}, \tag{2.10}$$

with σ_a: non-corrected stress amplitude and σ_m: residual stress. Nevertheless, this approach does not account for the material specific mean stress susceptibility. This can be done by performing fatigue experiments at different load ratios R. As illustrated in Fig. 2.12, the mean stress sensitivity is not constant but depends on the load ratio. Figure 2.12 is referred to as Haigh diagram [75].

2.5.4 Type of loading

As already indicated in the S/N-curve for AA2024 T351 in Fig. 2.4a, the type of loading which a component is exposed to influences fatigue life as well. As stated by Stanzl-Tschegg [11] and Mayer [43], torsional instead of axial loading reduces the fatigue lifetime by around one order of magnitude in the VHCF regime if one

directly compares the axial (σ_{max}) to the torsional stress amplitude (τ_{max}). Using the Mises criterion to calculate an equivalent stress level,

$$\sigma_{eq} = \sqrt{\sigma_{max}^2 + 3\tau_{max}^2}, \tag{2.11}$$

the lifetime for torsional loading is slightly higher than expected. This is confirmed by another detailed study on torsional fatigue of AA2024 T351 by Mayer [41], which found a 2-10x higher lifetime for torsional compared to tension-compression loading in measures of σ_{eq}. Reasons for this are discussed in detail in the associated references [11, 41, 43].

Beside torsional loading, there is a high relevance of bending, especially regarding the previously mentioned active drag reduction systems, where the material is exposed to flexural loading. Four-point bending testing of AA 2024 was performed by Shimokawa and Hamaguchi [76] up to 10^7 load cycles. The lifetime in the HCF regime is lower then for axial loading by up to one order of magnitude. Nevertheless, the characteristic shape of the S/N-curve, i.e. the change in slope between 10^5 and 10^6 load cycles, is also found when specimens are exposed to bending fatigue. The same is true for AA 2026, as proven by Li et al. [77] Furthermore, cracks are as well predominantly initiated at Fe-containing particles in or close to the surface [77] (cf. Grosskreutz and Shaw [39] and Mayer et al. [14] for axial loading). Further studies which performed bending testing on aluminum alloys are the one by Fawaz and de Rijck [78] and the one by Benachour et al. [79] which focus on crack growth rates. Suh et al. [80] recently found a lower fatigue strength for ultrasonic axial loading than for rotary bending fatigue testing at conventional frequencies for AA 7075 T651. The study by Wang et al. [81] evaluates the dynamic tensile fracture behavior of AA 2024 T4 and AA 7075 T6 at flexural loading. The authors found a higher crack initiation tolerance for AA 2024 compared to AA 7075 and a different damage distribution in both alloys. In total, it can be concluded that while the loading type has an influence on fatigue life, the underlying damage mechanisms are comparable for axial, torsional and flexural loading.

2.6 Statistical evaluation methods

As described above, beside the type of loading, fatigue life strongly depends on various factors like e.g. notches, surrounding atmosphere, but also on more factors that were not explicitly mentioned, like surface roughness, material homogeneity, temperature, etc. [83] These multiple influence factors cause a high scatter of the fatigue data, especially at very high cycle numbers. Therefore, statistical methods have to be applied to estimate the failure probability.

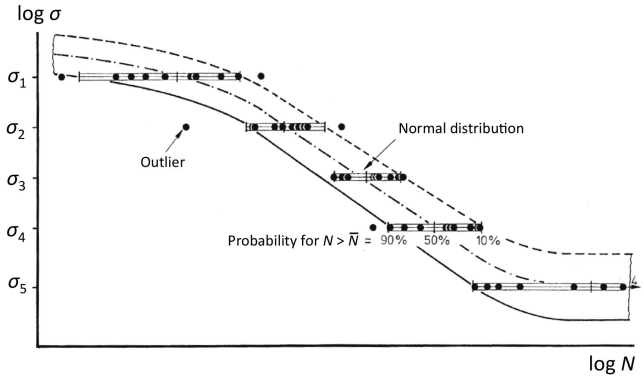

Figure 2.13: Statistical evaluation of fatigue tests according to Haibach [82]. $\bar{N}$ is the expected cycle number for failure for a certain stress amplitude.

For that purpose, fatigue experiments for different load amplitudes have to be performed. If one assumes a normal distribution for fatigue life on different load levels, one can deduce a set of S/N-curves for different failure probabilities [82]. In this context, the failure probability for a single load level is usually defined as

$$P = \frac{\text{number of failed specimens}}{\text{number of tested specimens}} \cdot 100\%. \tag{2.12}$$

This method is illustrated in Fig. 2.13. If the normal distribution does not lead to reasonable results, another useful concept is the $\arcsin\sqrt{P}$-method according to Dengel [84]. For this, a linear regression has to be performed according to

$$\sigma = a + b \cdot \arcsin\sqrt{P}, \tag{2.13}$$

where a and b are regression parameters. If the resulting fit is extrapolated to $P \to 0\%$, it specifies the fatigue limit for run-out specimens.

3 Testing methodology

3.1 Ultrasonic fatigue testing

One obstacle for material testing in the VHCF regime using conventional testing equipment is the extremely long duration of the experiments. An electro-mechanical fatigue testing machine operated at around 100 Hz would need roughly 3.8 months to reach 10^9 load cycles for one single measurement. To perform a VHCF study with significant statistics is thus impossible in reasonable time with conventional equipment. Therefore, testing is usually performed at ultrasonic frequencies. The first ultrasonic testing machine was constructed by Manson in the 1950s [85]. In subsequent decades, different setups were developed in different labs [85], like the one by Willertz [86] in the US, Stanzl-Tschegg [87] in Austria, Bathias [88] in France, Ishii [89] in Japan, Puskar [90] in Slovakia and Eifler [91] in Germany. Whereas the setups differ in details, they all have three main components in common [85]: a high frequency generator which generates sinusoidal electrical signals at a frequency of $\approx$ 20 kHz, a transducer which transforms the electrical signal into mechanical vibration, and a control unit.

The testing principle for axial loading is illustrated in Fig. 3.1. The setup creates a longitudinal standing wave with strain nodes at the connections of the different parts and maximum strain in the gauge length of the specimen. The mechanical vibration amplitude, generated by the transducer, is amplified by the horn due to the reduced cross section. The feedback signal of the oscillation is registered by an

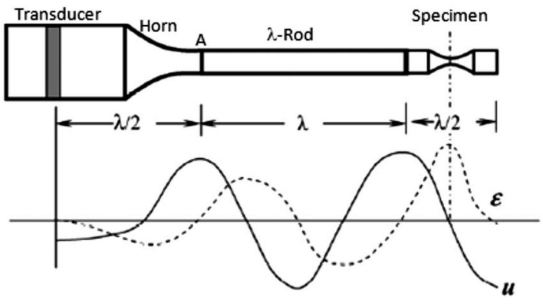

Figure 3.1: Principle of the ultrasonic fatigue testing equipment with distribution of displacement (u) and strain (ε) [92].

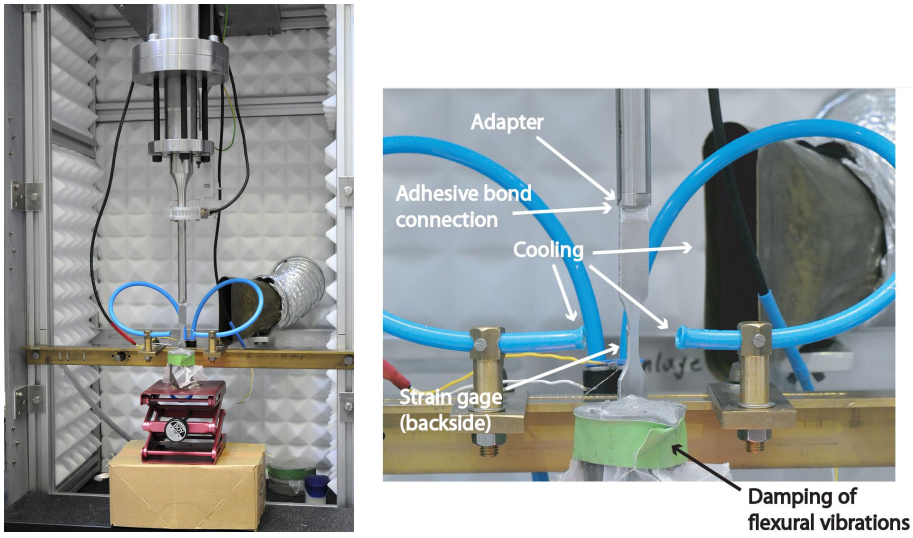

(a) Overview of the testing setup. **(b)** Details of the specimen during testing.

Figure 3.2: Ultrasonic fatigue testing system of type BOKU Vienna.

inductive displacement transducer ('A' in Fig. 3.1), which provides the input for the feedback control loop. Testing is performed in resonance frequency of the setup which is around 20 kHz. The feedback control keeps the excitation signal in phase with the feedback signal.

In this study, an ultrasonic fatigue testing machine developed at BOKU Vienna [87] was used. The setup is presented in Fig. 3.2. Since the system is designed to test rotationally symmetric solid specimens, an adapter, made of stainless steel, as illustrated in Fig. 3.3a was used for mounting the flat specimens into the setup. Sheet specimens were adhesively connected to the adapter. To avoid imprecise alignment of the specimen when mounted into the adapter, a simple setup for adjusting the sample orientation was used as illustrated in Fig. 3.4. For the adhesive connection, a commercially available two component epoxy glue was used. The glue was hardened at 70°C for 35 minutes. To exclude the risk of overaging, one specimen was kept at 80°C for one week and indentation measurements were performed before and after this treatment. Since no change in hardness was observed, the mounting procedure at elevated temperature was considered to not influence the subsequent fatigue experiments. The samples were laser cut to their final geometry (cf. Fig. 3.3b) with their longitudinal axis transversal to the rolling direction. The volume (surface) of the gage length was 80 mm^3 (112 mm^2). The flat back side of clad, riblet structured specimens was ground with abrasive paper (grade 120)

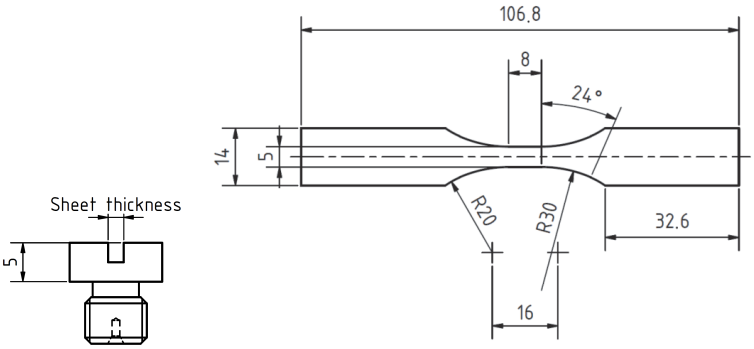

(a) Adapter. **(b)** Sheet specimen.

Figure 3.3: Sample geometry for ultrasonic fatigue testing.

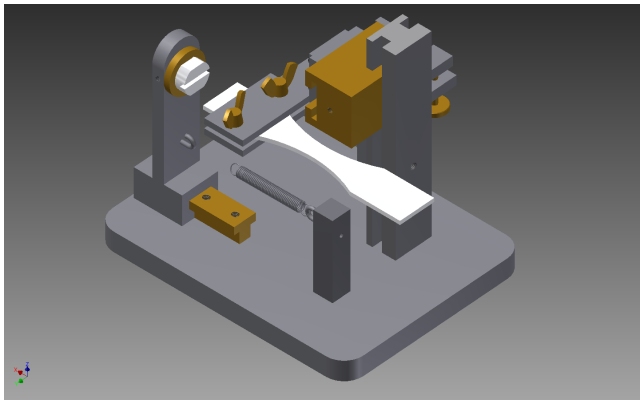

Figure 3.4: Specimen alignment setup for mounting into the adapter.

in order to remove the cladding on this side and hence avoid interference with fatigue behavior of the riblet structure on the front side. All flat specimens were mechanically polished along the longitudinal sample direction with abrasive paper up to grade 1000 in order to achieve a smooth surface. The small sides of all specimens were included in the polishing procedure. The resulting peak to peak roughness (R_z), measured with a profilometer, was (2.5 ± 0.4) μm. The relatively low scatter from 6 measurements was considered to have only a negligible influence on the fatigue life. Whereas AA 2024 specimens were polished by hand, for AA 7075 an improved mechanical procedure was applied which led to a comparable surface quality but induced much lower residual stresses. Clad and structured surfaces (with the only exception of the flat backside of riblet structured samples,

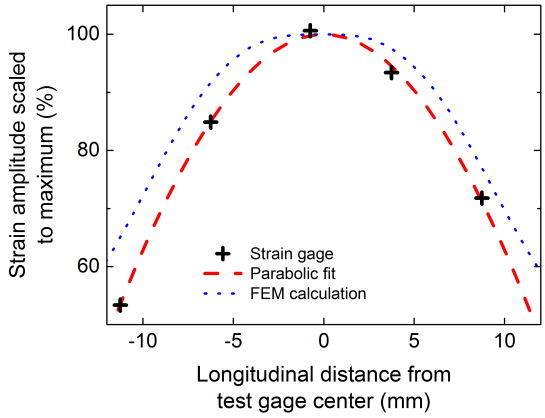

Figure 3.5: Strain distribution during ultrasonic fatigue testing.

see above) have not been polished after the fabrication process in order to preserve the surface layer.

Samples were calibrated using strain gages, which were removed after calibration. The fatigue testing was performed in displacement control. Since the applied load lies clearly below the yield strength of the tested material, a linear relationship between stress and strain according to Hooke's law was assumed:

$$\sigma = E\varepsilon, \tag{3.1}$$

with σ: stress, E: Young's modulus, and ε: strain. Flexural vibrations were damped effectively by immersing the bottom part of the sample in glycerin (cf. Fig. 3.2). The absence of bending during testing was ensured by observing the fast Fourier transform of the feedback signal of the oscillating system. The measurements were performed at room temperature. To avoid self-heating during testing, the specimen were continuously cooled down by compressed air. Furthermore, the measurements were performed in pulse-pause-mode with a typical pulse (pause) length of 100–990 ms (500 ms), depending on the applied load amplitude. All tests were performed below a temperature of 30°C.

Since the adapter has a much higher specific weight than the tested aluminum alloys, the $\lambda/2$-rod has been shortened to be partially replaced by the adapter. The resulting resonance frequency of the testing system was around 19.1 kHz. When strain amplitudes were measured at different specimen positions, a symmetric strain distribution along the samples direction with a maximum amplitude in the center of the gage length was observed (cf. Fig. 3.5). This is demonstrated by a parabolic fit to the strain data (red dashed line in Fig. 3.5).

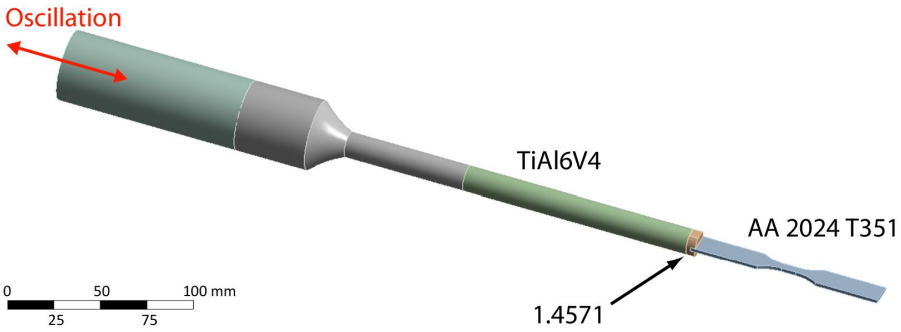

Figure 3.6: FEM model of the ultrasonic fatigue testing system. The model consists of the specimen, the adapter, the $\lambda/2$-rod and the horn.

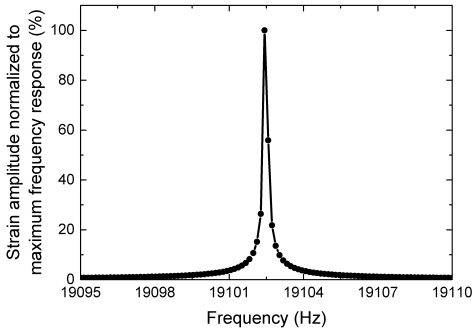

Figure 3.7: Frequency response for longitudinal excitation of the testing setup from the harmonic response analysis.

For a better understanding of the dynamics of the ultrasonic fatigue testing equipment, a finite element (FEM) model of the setup was designed using the commercially software ANSYS [93], which is presented in Fig. 3.6. The geometry was modeled in 3D with linear elastic material behavior. For meshing, tetragonal as well as hexagonal elements were used. The element size was 5 mm, for horn and $\lambda/2$-rod, 2 mm for the adapter, and 1 mm for the specimen. Calculations were performed for AA 2024 T351. In a first step, a modal analysis was conducted, calculating the first 100 normal modes of the configuration. Afterwards, these modes were superimposed in a harmonic response analysis whereat the setup was longitudinally excited as indicated in Fig. 3.6. The resulting response vs. excitation frequency is plotted in Fig. 3.7.

As can be seen, the calculated resonance frequency is in good agreement with the experimental value. If one now exposes the system to an oscillation at the calculated

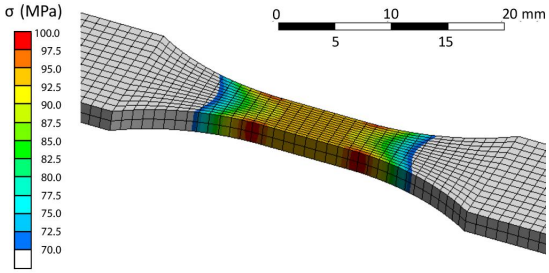

Figure 3.8: Stress distribution during maximum load, if the testing system is exposed to a longitudinal oscillation in resonance frequency.

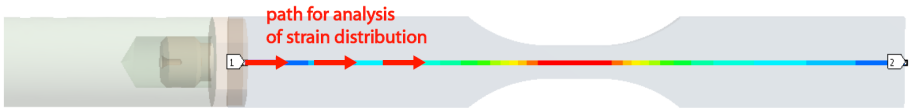

Figure 3.9: Path for the analysis of the strain distribution in the FEM simulation.

resonance frequency, the standing wave results in a stress distribution as presented in Fig. 3.8. Apparently, the stress is slightly increased at the small sides of the specimen, which demonstrates the usefulness of modeling the setup by FEM: If this region of peak stress would not be accounted for, cracks would always be initiated in this region of peak stress. This problem can be overcome by applying a higher force when polishing the relevant sample sites during the preparation procedure, which induces compressive residual stresses and thus shifts crack initiation to the specimen center.

The longitudinal stress distribution can as well be extracted from the FEM model. Therefore, strain values during maximum load were extracted along the path indicated in Fig. 3.9. The corresponding strain distribution is presented in Fig. 3.5 (blue dotted line). It is symmetric and has its maximum in the specimen center. Compared to the experimental values, the simulated strain amplitudes have a slightly broader distribution. Possible reasons for this are the adhesive bond connection, which is not accounted for in the FEM model or small remaining misfits when mounting the specimen into the adapter.

Beside strain distribution, another important issue is self-heating of the specimen during testing, which is usually induced by microplasticity, i.e. dislocation glide [94]. Fatigue experiments were performed nominally at room temperature. The pulse and pause length during testing were chosen according to the development of the resonance frequency for which a reference measurement was carried out. For this purpose, a thermocouple was connected to the gauge section of a specimen by conductive heat paste. The sample was then exposed to cyclic loading in continuous mode. In order to increase the specimen's temperature, the load amplitude was raised gradually. The self-heating lowered the resonance frequency as indicated in

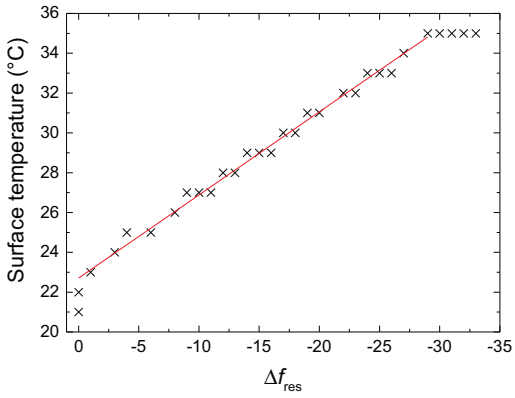

Figure 3.10: Self heating of the specimens during testing vs. resonance frequency.

Fig. 3.10. Up to around 35 °C, a linear relationship can be assumed. A fit yields a slope of the curve of

$$\frac{\Delta T}{\Delta f_{\mathrm{res}}} = -0.42\,\frac{^{\circ}\mathrm{C}}{\mathrm{Hz}}, \tag{3.2}$$

with T: temperature and f_{res}: resonance frequency. If the resonance frequency drops by more than 30 Hz, the surface temperature seems to remain constant. However, this constant temperature value is attributed to a less efficient contact between sample surface and thermocouple at higher vibrational amplitudes: When the oscillation amplitudes of the specimen are too high, the thermocouple is pushed away continuously from the specimen's surface. Nevertheless, if the drop in resonance frequency does not exceed 15 Hz, specimen temperatures will not exceed 30°C.

3.2 Bending fatigue

The type of loading in the previously described active drag reduction approach is not axial but bending loading. Therefore, bending fatigue tests are of high interest in order to compare axial with bending fatigue data.

Tests in this study were performed with a modified version of a setup which was developed at the Central Institute for Engineering, Electronics and Analytics (ZEA-2, FZ Jülich) and originally used to investigate aerodynamic drag reduction in a wind channel as described in [95, 96]. For fatigue testing, the setup was adapted to test narrow, strip-like specimens. The setup is presented in Fig. 3.11. It principally allows for the simultaneous testing of 7 specimens, which are fixed at both ends

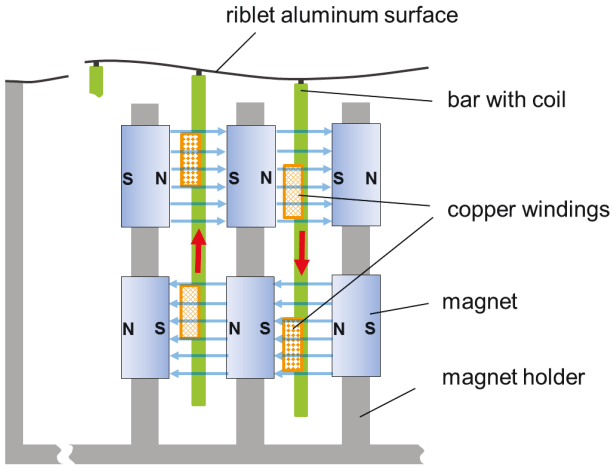

Figure 3.11: Setup for bending testing, using a modified version of a setup for wind channel experiments as described in [95, 96].

and actuated at 3 different points. The sinusoidal actuation was performed electromagnetically by using aircoils. The setup was calibrated by a laser vibrometer prior to testing. Specimens had a size of 120 mm x 5 mm and a thickness of 1.6 mm. The setup was controlled during testing using the software Matlab. The displacement amplitudes were found to be stable during cyclic loading. Tests were performed at testing frequencies of around 100 Hz.

In order to convert the displacement amplitudes into stress amplitudes, an FEM model was developed as presented in Fig. 3.12. Since the applied stress amplitudes were below the yield strength of AA 2024, the material was considered to be linear-elastic. The specimen was fixed in the setup at both ends with a distance of 19.5 mm to the outer actuation units. A displacement was set at 3 different sample locations (at 19 mm, 39 mm, and 69 mm from the left side), as indicated in Fig. 3.12a. The Oscillation of the inner and the two outer displacements was in opposite phase. Meshing was performed using cubic elements of 0.5 mm edge length. The mesh at sample parts which were subject to external displacements was refined to an edge length of 0.25 mm. The resulting stress distribution during maximum load is presented in Fig. 3.12b.

For setting the appropriate displacement amplitudes during testing, a parameter study was carried out, which is summarized in Fig. 3.12c and yielded a linear behavior of stress amplitude as a function of the displacement amplitude. Displacement amplitudes were measured from zero position. The analysis considered the normal stress at maximum loading. A fitting procedure yielded

$$\sigma(\mathrm{MPa}) = 1.30453\, x(\mu\mathrm{m}), \tag{3.3}$$

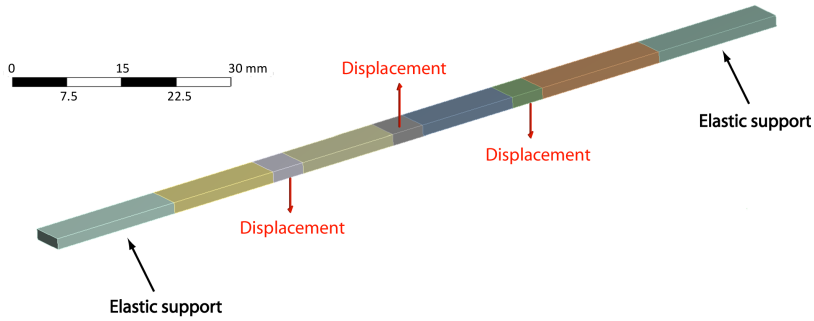

(a) FEM model of the bending testing setup.

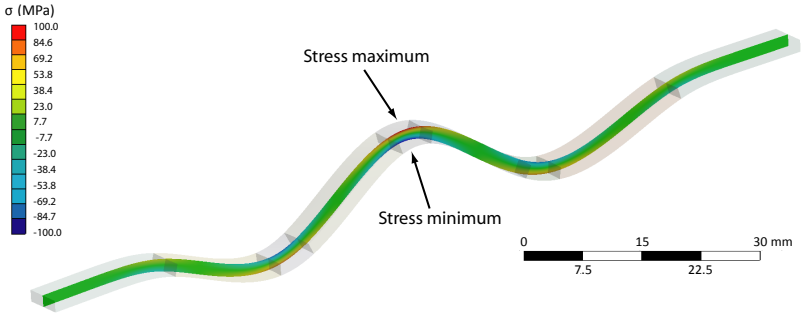

(b) Stress distribution during maximum load. The displacement in this graph is over scaled by a factor of 68. The stress amplitude was adapted to 100 MPa normal stress in this case.

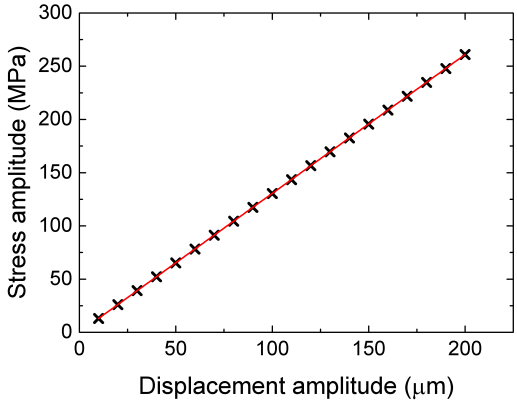

(c) Stress amplitude as a function of displacement amplitude during bending testing.

Figure 3.12: FEM calculation for adjustment of the displacement amplitude.

with σ: normal stress, and x: displacement. The bending testing setup was designed during this study at the Central Institute for Engineering, Electronics and Analytics (ZEA-2, FZ Jülich) and tested successfully during first measurements where a stable amplitude was observed at a testing frequency of around 100 Hz.

3.3 Micro indentation

Micro indentation measurements were performed on polished cross sections using a setup delivered by CSM equipped with a Berkovic type indenter. Polished cross sections were prepared using epoxy embedding at room temperature. The required flat surfaces were obtained by grinding in different steps up to grade 2500, subsequent mechanical polishing with diamond paste of 3 and 1 μm grain size, and finally chemical polishing. In order to achieve a sufficient lateral resolution, small testing forces were necessary to keep the size of the indentations – and therefore the influenced area of the sample surface – sufficiently small. For evaluating the influence of the small testing forces, an indentation series at 6 different load levels in the range from 1 to 50 mN was performed. For each force 10 measurements were carried out. A summary of this pretest is presented in Fig. 3.13 which shows a clear indentation size effect: Measurements at small testing forces result in higher measured hardness values – which can be assumed as an artifact – as well as a

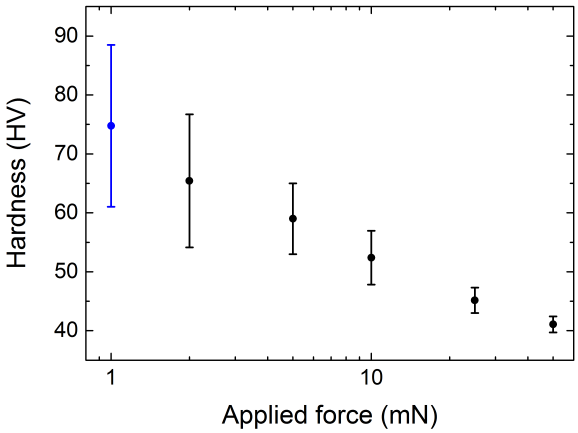

Figure 3.13: Measured hardness of the soft CP Al clad layer of Alclad 2024 as a function of applied testing force. A clear indentation size effect can be seen.

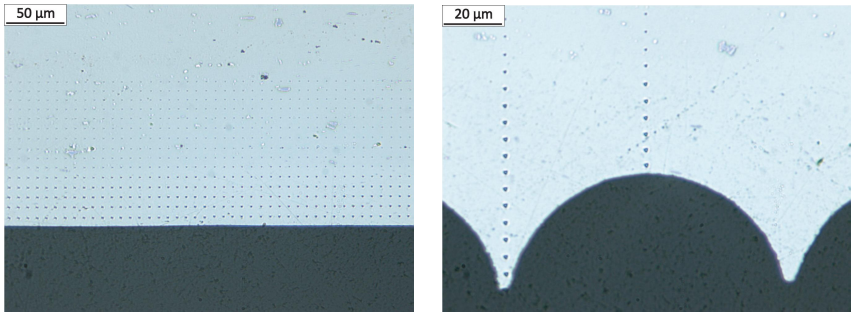

(a) Flat material. **(b)** Riblet structured material.

Figure 3.14: Indentations in flat and riblet structured material. The small testing force of 1 mN allows for a sufficient lateral resulution.

higher scatter of the data. This effect – which occurs in a variety of materials [97] – is also observed for the alloys studied in the present work, as reported by Iost and Bigot [98] who performed measurements on AA 2024 T351. Further discussions on the underlying mechanism of the indentation size effect in aluminum alloys are provided e.g. in [99–101].

In order to achieve a sufficient lateral resolution, a testing force of 1 mN was chosen in the present work. Indentations in flat material were performed within a dot-matrix (cf. Fig. 3.14a). In the case of riblet structured material, measurements were conducted on paths from the surface to the interior of the material, starting from the riblets' tops or bottoms (cf. Fig. 3.14b). In both cases, a distance of 5 μm was chosen between two indentations. The indentation size was between 1 and 2 μm in the clad layer and significantly smaller in the substrate as well as in bare material.

3.4 X-ray diffraction

Near-surface residual stresses were determined by X-ray diffraction (XRD), using the $\sin^2(\Psi)$-method according to Macherauch [102, 103]. Experiments were performed using an Phillips X'Pert diffractometer type MRD 3050/65 with an Cu-K_α X-ray tube. For the determination of residual stresses, the shift of the aluminum (4 2 2) diffraction peak was observed as a function of sample orientation assuming a bidirectional elastic residual stress state.

3.5 Scanning electron microscopy

Fracture surfaces as well as polished cross sections were examined using a Zeiss Merlin scanning electron microscope (SEM). The detection of secondary electrons (SE) was applied to study the sample topography. Electron backscatter diffraction (EBSD) was used to analyze the grain orientation. The chemical composition of different phases in the material as well as of inclusions was studied by energy dispersive X-ray spectroscopy (EDX).

3.6 Optical microscopy

Polished cross sections were studied using a Zeiss metallographic microscope. In order to improve the contrast between substrate and clad layer, specimens were etched according to Dix and Keller [104, 105] or Kroll [105].

4 Material

The two high strength wrought aluminum alloys AA 2024 and AA 7075 were invented in the 1930s (2024) and 1940s (7075) and – as mentioned earlier – became extensively used in airplane construction because of their high specific strength [106]. The following section summarizes the relevant material properties as well as a comprehensive characterization of the supplied material.

The high strength of both alloys results from precipitation hardening, i.e. the presence of precipitates hinders the movement of dislocations and therefore increases yield strength. A schematic overview of the required heat treatments is provided in Fig. 4.1. In a first step, the material is solution annealed, leading to a homogeneous solid solution. Subsequent quenching in water or air causes a disequilibrium state with the material being supersaturated by both substitution atoms and vacancies. During aging, the dissolved atoms form precipitates whereat the high concentration of vacancies facilitates diffusion. In the Al-Cu system, a sequence of four different precipitates occurs [107]: Guinier-Prestion zones (GPI), θ'' (GPII), θ', and θ. While GP zones form during aging at room temperature, the others require artificial aging. The strongest effect of precipitation hardening is achieved by GPII zones. In the Al-Zn-Mg system, at elevated temperature the GP zones transform into η' and subsequently into η ($MgZn_2$) phase precipitates [108].

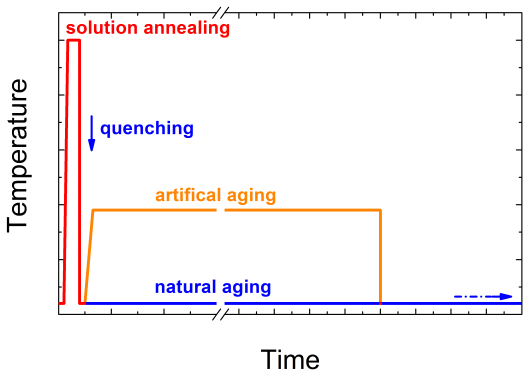

Figure 4.1: Schematic temperature profile for precipitation hardening of high strength aluminum alloys.

Table 4.1: Chemical composition of the substrate from inductively coupled plasma optical emission spectrometry (ICP/OES). Mass fractions $\geq 1\%$ are highlighted.

Element	Mass fraction (%)	
	AA 2024	AA 7075
Cr	-	0.20
Cu	4.58	1.18
Fe	0.21	0.098
Mg	1.48	2.07
Mn	0.47	0.015
Si	0.073	0.054
Ti	0.016	0.037
Zn	0.098	5.04

The chemical composition of both alloys was measured by inductively coupled plasma optical emission spectrometry (ICP/OES) and is summarized in Fig. 4.1. All element concentrations are within the respective ASTM standard for the alloys [109, 110]. Details on the effects of the different alloying constituents can be found e.g. in [111].

4.1 AA 2024

Most experiments in this study were performed on AA 2024 T351. The mechanical properties of this alloy are summarized in Tab. 4.2. The Young's modulus was determined by pulse excitation measurements. Yield stress and ultimate tensile strength were taken from tensile tests. The resulting stress-strain-curves for different sheet orientations with respect to the rolling direction are presented in Fig. 4.2, where 3 measurements were performed for each sheet orientation. In general, the material strength is higher in longitudinal (L-direction). Since riblets produced by the later described rolling process are always oriented along the rolling direction, the load in the previously described system for aerodynamic drag reduction is always in T-direction. (Riblets are normal to the load direction.) For tensile testing, the specimens had to be slightly notched in order to keep the extensometer in a defined position. Therefore, the elongation at fracture can not be taken from the stress-strain-curves. Nevertheless, the remaining parameters are reliable. Hardness measurements in this chapter were performed at a testing force of 5 N.

As described in the next chapter, the riblet rolling process in some cases requires assistance by heat treatments. Therefore, a closer attention should be payed to material changes which occur during these processes. Relevant process parameters for the heat treatments are provided e.g. in [112]. The parameters chosen for this study are summarized in Tab. 4.4. The aging conditions for the T6 state were

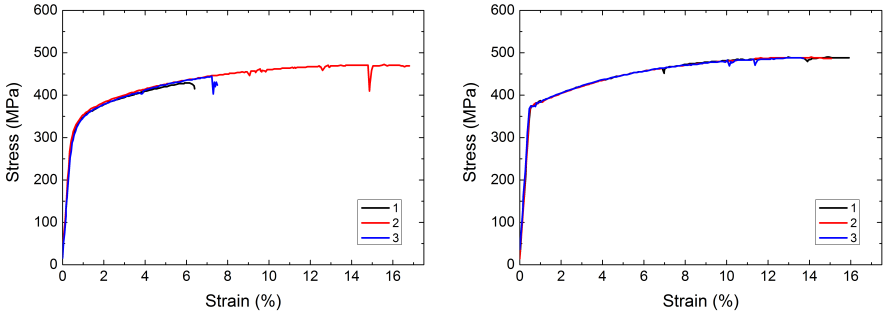

(a) T-direction. **(b)** L-direction.

Figure 4.2: Tensile testing of 2 mm thick AA 2024 sheets.

Table 4.2: Key mechanical properties of AA 2024.

Young's modulus	72.5 GPa
Yield strength, 0.2%, T-direction	319 MPa
Yield strength, 0.2%, L-direction	376 MPa
Ultimate tensile strength, T-direction	431 MPa
Ultimate tensile strength, L-direction	488 MPa
Hardness	137 HV0.5

Table 4.3: Heat treatments for precipitation hardening. Parameters were chosen according to [112]. Artificial aging to the T6 state was performed according to [113].

Temper	
O (soft annealed)	Annealing at 400°C for 2.5 h, slow cool down (30°C/h) to 250°C.
T4	Solution annealing at 500°C for 80 min, quenching in water, natural aging for 8 d.
T6	Solution annealing at 500°C for 80 min, quenching in water, artificially aging at 205°C for 3 h.

Table 4.4: Mechanical properties of the AA 2024 material after heat treatments.

Temper	Tensile strength	Hardness
T351	431 MPa	(127 ± 3) HV0.5
O	198 MPa	(58 ± 1) HV0.5
T4	442 MPa	(137 ± 4) HV0.5
T6	434 MPa	(144 ± 4) HV0.5

chosen according to the study by Alexopoulos [113] who compared a variety of ageing conditions, i.e. different temperatures and aging durations, for AA 2024. As the material was received in the T351 state, it was considered to be the initial state for the heat treatments. All heat treatments therefore had to start with a sufficiently long solution annealing process. To ensure an sufficiently long holding time, the pretests were carried out with clad sheets, since it requires longer holding times than bare material [112]. If the process successfully works, the same parameters can be used for both, clad and bare material, since a longer solution annealing than required does not harm the bare sheets [112]. After the treatments, the different states were compared by tensile testing, indentation measurements, as well as by EBSD imaging of the microstructure.

The results of mechanical testing are presented in Tab. 4.4. One tensile test was conducted for each heat treatment in T-direction, whereas five indentations were performed to quantify the hardness. While the soft annealed state shows – as expected – a much smaller tensile strength and hardness than the age hardened material, all 3 precipitation hardened material states are comparable regarding their tensile strength and hardness. In the T4 state, the tensile strength is only slightly higher than for the T351 and the T6 temper. Referring to the hardness, the T6 is slightly harder than T4 which is slightly harder than T351. Considering the limited statistics, it can be stated that the mechanical properties are in a reasonable range and that the chosen parameters for age hardening were appropriate.

Figure 4.3 summarizes topographic and EBSD measurements of polished cross sections of the different tempers. Whereas the age hardened states have a similar appearance, the soft material shows an accumulation of precipitates at the grain boundaries. The larger bright phases in all four images are basically Cu rich phases, as determined by EDX. The EBSD maps are comparable for all four measurements. Generally, the grain size of the cladding is much larger than the one of the substrate.

An overview of the as-received flat precursor materials is presented in Tab. 4.5, the respective polished cross sections are shown in Fig. 4.4. Beside the bare material, two different types of clad sheets were studied. A short introduction to

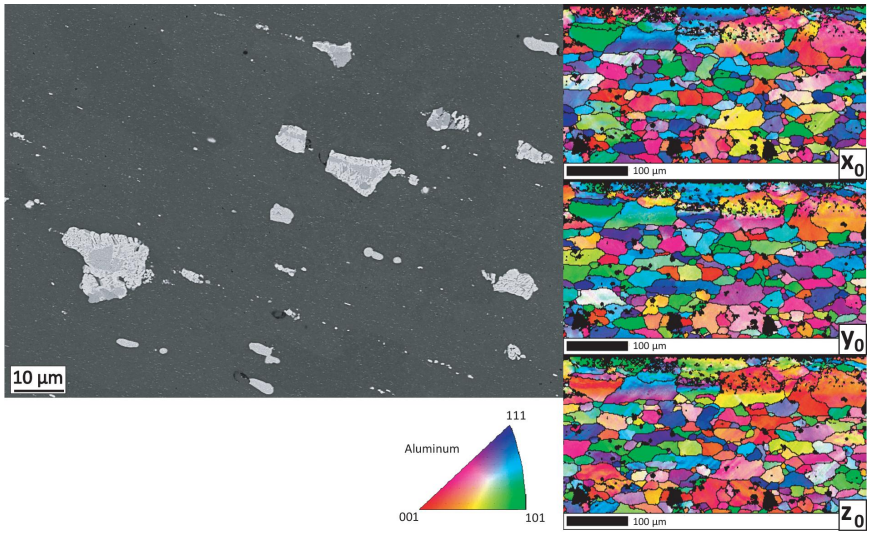

(a) As-received Alclad 2024 (T351).

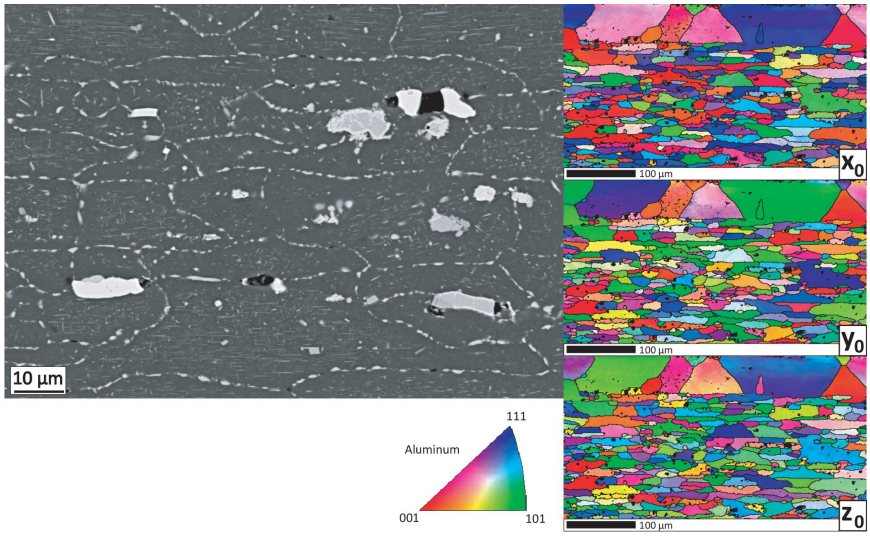

(b) Soft annealed Alclad 2024 (O).

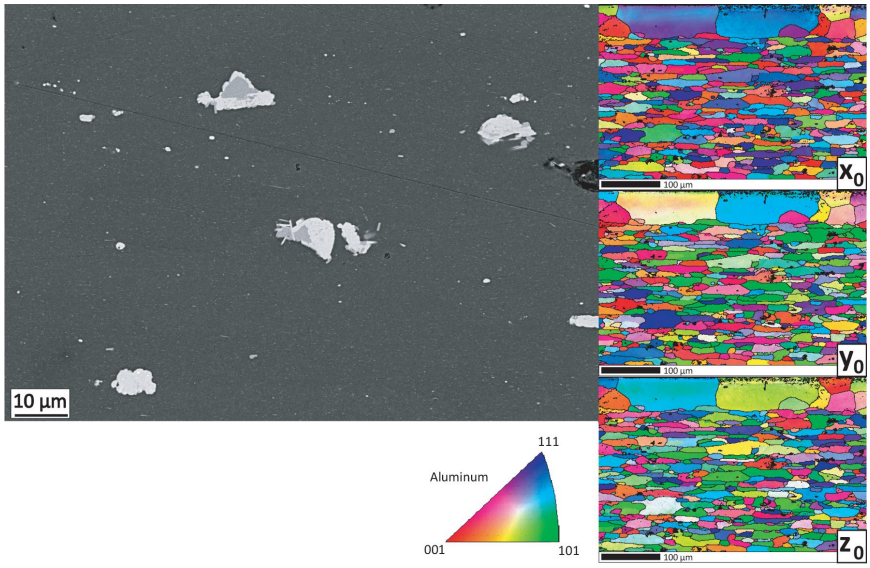

(c) Precepitation hardened Alclad 2024 (T4).

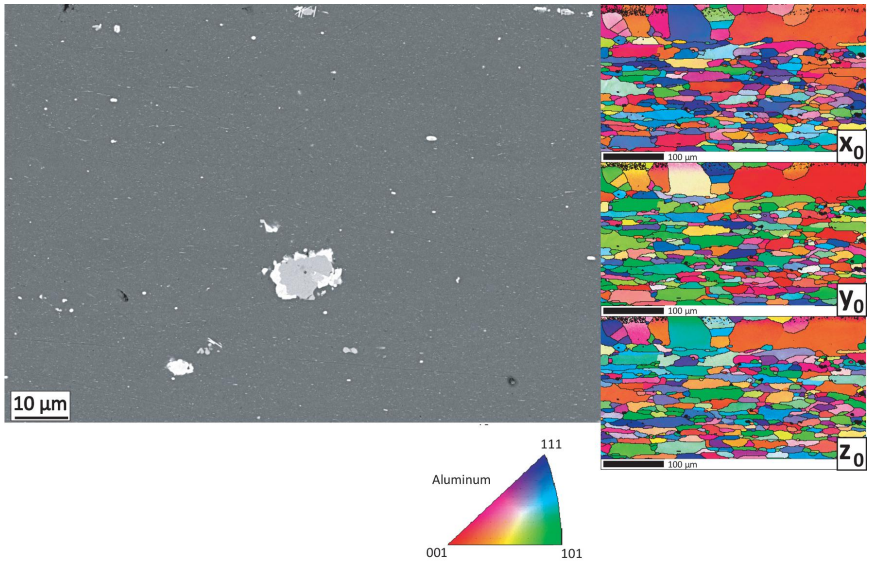

(d) Precepitation hardened Alclad 2024 (T6).

Figure 4.3: Electron microscopy on polished cross sections of the Alclad 2024 substrate after different heat treatments.

Table 4.5: Key parameters of the studied AA 2024 material. Per cent values for the cladding thickness are relative thickness values with respect to total sheet thickness.

Material	Temper	Sheet thickness	Cladding thickness
Bare material	T351	2 mm	-
Clad material	T351	2 mm	(59 ± 4) μm / 2.9%
Clad material	T351	1.6 mm	(69 ± 3) μm / 4.1%

Figure 4.4: Polished cross sections of studied AA 2024 specimens. (a) 2 mm thick bare sheet. (b) 2 mm thick clad sheet. (c) 1.6 mm thick clad sheet.

claddings can be found later in this chapter. In order to evaluate different material parameters, two different sheet thicknesses with two different cladding thicknesses were evaluated. The 2 mm thick clad sheets have a relatively thin clad layer (2.9%), whereas at the 1.6 mm thick sheets it is relatively thick (4.1%). The cladding thickness was measured on different positions on polished cross section images (e.g. Fig. 4.4).

4.2 AA 7075

Characterization of the AA 7075 material was conducted comparable to the AA 2024 alloy, including determination of Young's modulus, tensile testing, and hardness measurements. The stress-strain-curves are provided in Fig. 4.5, for both L- and T-direction. A summary of the key results is provided in Tab. 4.6. The material shows a significantly higher yield and tensile strength than AA 2024. While for AA 2024, we found a significant difference in strength for the different sheet orientations, this effect is not observed in AA 7075, where both, yield and ultimate tensile strength are comparable for both directions.

The material was available only on the Alclad version, as indicated in Tab. 4.5 and in Fig. 4.6. For experiments on bare material, the cladding was removed mechanically

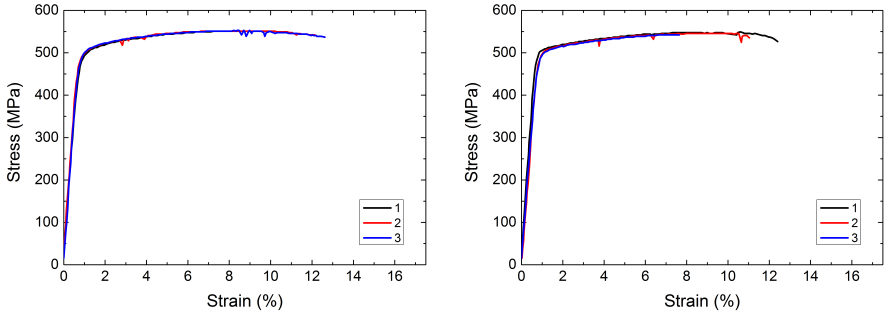

(a) T-direction. **(b)** L-direction.

Figure 4.5: Tensile testing of 2 mm thick AA 7075 sheets.

Table 4.6: Key mechanical properties of AA 7075.

Young's modulus	70.9 GPa
Yield strength, 0.2%, T-direction	487 MPa
Yield strength, 0.2%, L-direction	494 MPa
Ultimate tensile strength, T-direction	551 MPa
Ultimate tensile strength, L-direction	547 MPa
Hardness	187 HV0.5

by grinding with sand paper.

4.3 Claddings

Whereas Aluminum alloys of the 1000, 3000, 5000, 6000, and 8000 series show a relatively good resistance to corrosion in marine, urban and industrial environments [114], AA 2024 and AA 7075 are quite sensitive to different forms of corrosion [115]. A detailed study of the electrochemical characteristics of intermetallic phases in

Table 4.7: Key parameters of the studied AA 7075 material. Per cent values for the cladding thickness is relative thickness values with respect to total sheet thickness.

Material	Temper	Sheet thickness	Cladding thickness
Clad material	T6	2 mm	(67 ± 4) μm / 3.2%

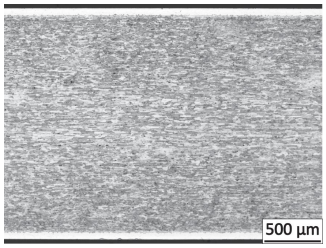

Figure 4.6: Polished cross sections of studied AA 7075 specimens. The sheets were clad and of 2 mm thickness.

aluminum alloys was conducted by Birbilis and Buchheit [116]. Both, AA 2024 and AA 7075 contain a high amount of Cu which, incorporated in intermetallic phases, is cathodic with respect to the matrix and thus promotes the dissolution of the surrounding matrix [115, 116]. On the other hand, Mg and Zn rich intermetallics are usually anodic with respect to the matrix and hence dissolve first, which leads to localized corrosion [115, 116]. To prevent corrosion damage, the aluminum alloys studied in the present work are frequently cladded with a thin layer of commercially pure (CP) Al of few 10 μm thickness to separate the reactive phases from harmful environmental influences.

For deposition of protective coatings, there exists a variety of processes like physical or chemical vapor deposition [117, 118], thermal spraying [115, 119, 120], laser cladding [121–123], explosive welding [124–126], or roll welding [127–129]. In this work, the material was cladded by the latter technique, namely hot roll bonding. In roll bonding, both layers are jointly passed through a pair of rolls which imposes a sufficiently high pressure to bond the material by adhesion [129, 130]. The bond strength of such a joint approaches the strength of the surface material, if the surface expansion is large enough to cause the oxide layer to break-up and to allow the fresh metal in between the cracks to weld [129, 131]. As demonstrated by Yan and Lenard [129], the bonding process can be facilitated if carried out at elevated temperatures.

The manufacturing process of multi-layered aluminum alloy sheets is referred to as *Alclad* process and is described in detail in the study by Liu et al. [127]: The center layer, termed *core*, is usually prepared from cast ingot, whereas the outside layers, termed *liner*, are rolled plates. The liner-core-liner assembly is heated up in a furnace and then hot rolled in multi-passes to bond the different layers together. A comprehensive literature overview on influencing factors on the bonding quality, like surface cleaning, rolling pressure, temperature, speed, and friction at the interface is provided as well in [127, 128]. The hot roll bonding process is considered the most economical and therefore the primary method for large-scale manufacturing

of Alclad material [127, 128].

5 Riblet rolling

The efficiency of a riblet structure with respect to drag reduction strongly depends on its geometry. In this study, a semi-circular riblet shape was chosen since it offers a good compromise between drag reduction properties and producibilty. The sheets were structured in a flat rolling process which allows for riblet production on a larger industrial scale. Riblet rolling was performed by the Institute of Metal Forming (IBF, RWTH Aachen University). Details on the rolling process can be found in [132, 133].

5.1 Rolling procedure

An overview of the rolling process is presented in Fig. 5.1. Before rolling, a fine high-strength steel wire is tightly wound around the upper roll to structure it with the negative riblet imprint. Afterwards, the riblet structure is formed into the sheet by riblet rolling. A detailed study of influencing factors during riblet rolling is provided by Pöplau et al. [134].

In total, four different riblet geometries were produced, as summarized in Tab. 5.1. Polished cross sections of structured material are provided in Fig. 5.2. Alclad 2024 specimens were riblet rolled in the as-received state (T351). 2 mm thick clad sheets were structured with a riblet diameter of 80 μm, whereas for 1.6 mm thick clad sheets a diameter of 300 μm was chosen. Sheets with 300 μm riblets had to be stretched after rolling to remove a rolling induced longitudinal curvature of the

Table 5.1: Key parameters of the studied specimens.

Material	Temper	Sheet thickness	Cladding thickness	Riblet diameter
AA 2024	T351 / T4	2 mm	-	100 μm
Alclad 2024	T351	2 mm	(59 $\pm$ 4) μm	80 μm
Alclad 2024	T351	1.6 mm	(69 $\pm$ 3) μm	300 μm
Alclad 7075	T6	2 mm	(67 $\pm$ 4) μm	100 μm

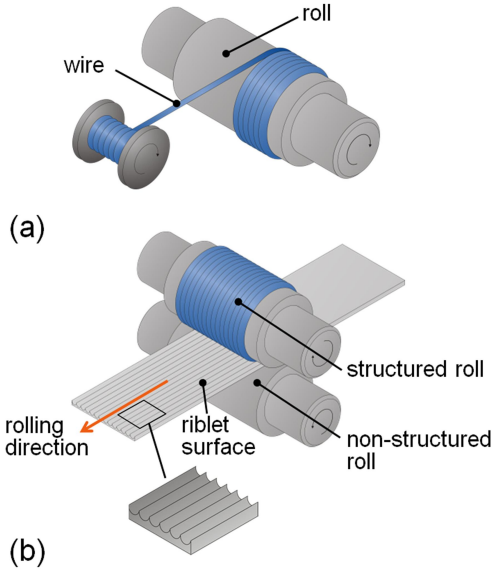

Figure 5.1: Rolling procedure for semicircular riblet geometry [134, 135]. (a) Preparation of the rolling equipment. (b) Rolling procedure.

sheets. Alclad 7075 was structured with a riblet diameter of 100 μm, as well in the as-received state (T6).

Contrary to the well suited rolling behavior of the clad material, the bare material is much harder than the CP Al cladding. Consequently, rolling of bare material in the T351 temper led to poor riblet geometry and high wear of the rolling equipment. To overcome this problem, sheets were rolled in the soft-annealed O state. The respective heat treatment was performed by annealing at 400°C for 3 hours and subsequently controlled cooling (30°C/h) to 250°C. Afterwards, the furnace was turned off, leading to a faster cooling rate down to room temperature. In this soft material state (O) riblet rolling was performed with satisfying riblet quality. Subsequently, the material was precipitation hardened to the T4 state by solution annealing at 500°C for 80 minutes, quenching in water and natural aging for 8 days. The T4 state was chosen because it does not require additional cold working after the riblet structuring process. As stated before (cf. Tab. 4.4, p. 36), the T4 and the T351 state can be considered comparable.

The chosen riblet dimensions are in the range of practical relevance for active drag reduction systems [95, 96]. The choice of specimen types allows for comparison between bare and clad material with different riblet dimensions. Furthermore, considering clad material, it provides a solid basis for evaluating the general influence of (i) CP Al claddings, (ii) cladding thickness, (iii) sheet thickness, and (iv) core material (AA 2024 vs. AA 7075). In a first step before fatigue testing, material

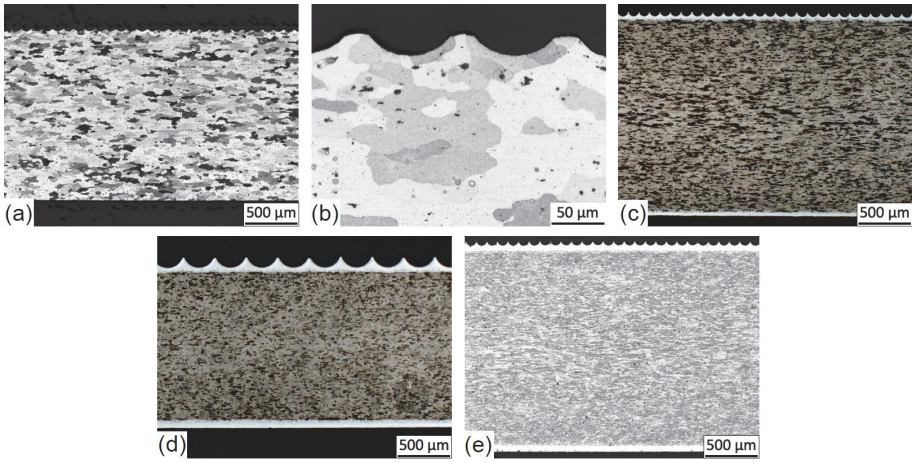

Figure 5.2: Polished cross sections of riblet structured material. (a) and (b) 2 mm thick AA 2024 T4. (c) 2 mm thick Alclad 2024 T351. (d) 1.6 mm thick Alclad 2024 T351. (e) 2 mm thick Alclad 7075 T6.

changes due to the rolling process were analyzed by micro indentation and residual stress measurements which will be discussed in the following.

5.2 Micro indentation

Micro indention of flat and riblet structured bare AA 2024 yielded a homogeneous hardness distribution as presented in Fig. 5.3. There is no evidence for a dependency of hardness as a function of distance to the outer edge neither for the flat, nor for the riblet structured case. The structured material is with 215 HV slightly harder than the flat material with 194 HV. Considering the different states of the specimens (T351 for clad vs. T4 for riblet structured material) this small difference is attributed to the slighty higher hardness of the T4 compared to the T351 state (cf. Tab. 4.4, p. 36). Since the material was heat treated after the structuring process, the absence of work hardening in the riblet structured case is not surprising.

Hardness measurements for Alclad 2024 are summarized in Fig. 5.4. Indentations on structured material were started from riblets tops and bottoms. The distance from the outer edge was defined as the distance from the riblet tops in both cases. The most obvious feature in both graphs is the clearly different hardness if one compares the clad layer with the substrate. The riblet structuring itself only slightly

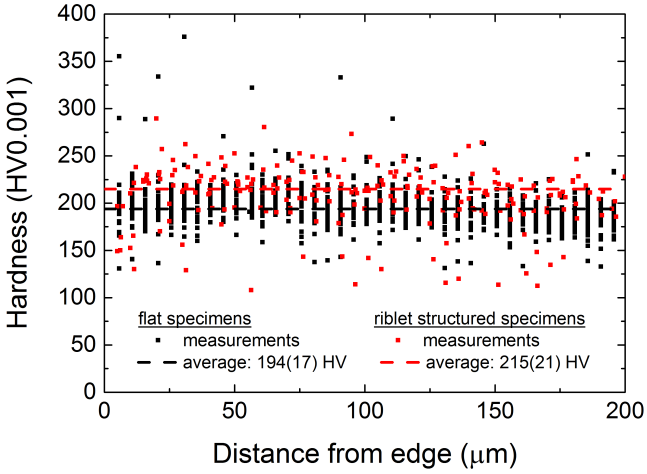

Figure 5.3: Micro indentation measurements of flat and riblet structured bare AA 2024.

rises the hardness of both, the cladding and the substrate. For the 2 mm thick sheet, the cladding hardness changes from 68 to 78 HV. For the 1.6 mm thick sheets this change is from 75 to 83 HV. Considering the quite large scatter of the measurements, measured values for flat and structured material overlap in the range of one standard deviation and thus this change is not considered to be significant. The same is true for the work hardening of the substrate below the clad layer. The change from 223 to 232 HV (2 mm thick sheets) and from 219 to 246 HV (1.6 mm thick sheets) is clearly within the standard deviations. Therefore it can be concluded, that Alclad 2024 material does not show a significant raise in hardness due to work hardening during riblet rolling. Furthermore, another measurement on a riblet structure in Alclad 2024 on a semi-circular path a few μm below the surface (cf. Fig. 5.6) yielded a homogeneous hardness distribution along different positions on the structured surface.

In the case of Alclad 7075 (Fig. 5.5), the difference in hardness is only slightly larger than in the Alclad 2024 case. The raise in micro hardness of the clad layer is with a change from 71 to 93 HV slightly outside the range of one standard deviation. Nevertheless, the hardening of the substrate from 279 to 296 HV very clearly does not exceed one standard deviation.

A summary of the micro indentation measurements is provided in Tab. 5.2. Considering the results for all sample types, it can be concluded that there is generally

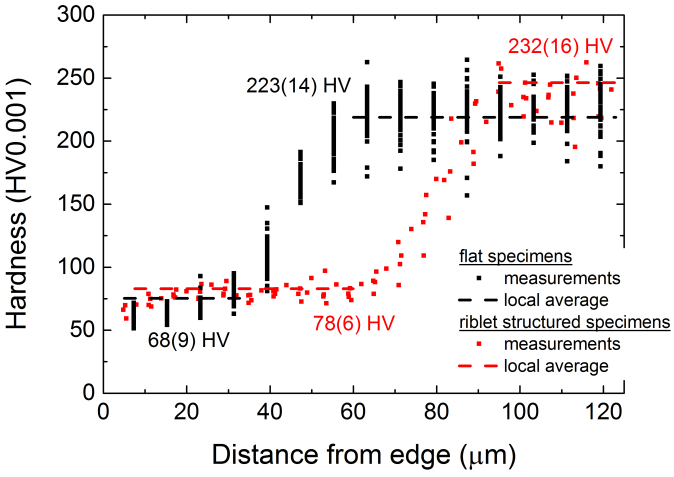

(a) 2 mm thick sheets with a riblet diameter of 80 μm.

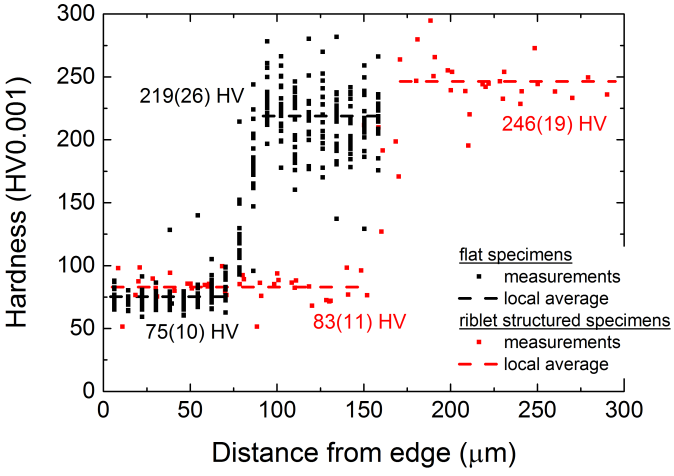

(b) 1.6 mm thick sheets with a riblet diameter of 300 μm.

Figure 5.4: Micro indentation measurements of flat and riblet structured Alclad 2024.

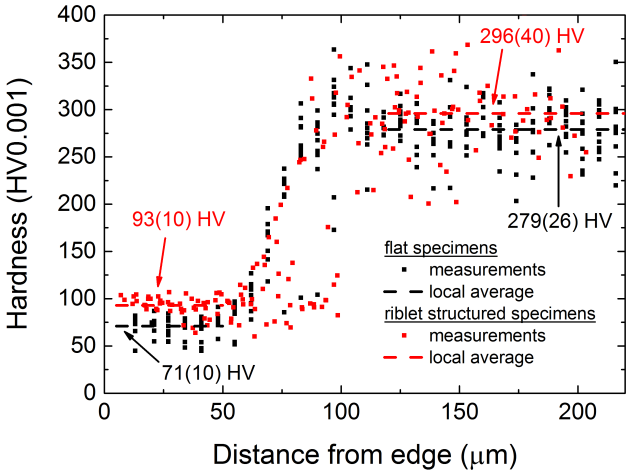

Figure 5.5: Micro indentation measurements of flat and riblet structured Alclad 7075.

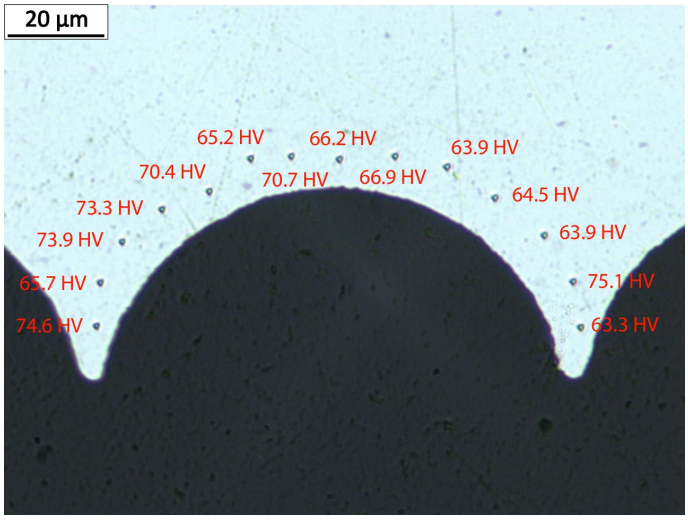

Figure 5.6: Lateral hardness distribution in the riblet structured case for Alclad 2024.

Table 5.2: Vickers hardness from micro-indentation tests at a testing force of 1 mN. N is the number of indentations.

		Hardness (HV0.001)	N
AA 2024	**2 mm thick bare sheets**		
	Flat material	194 ± 17	1,143
	Riblets	215 ± 21	184
	2 mm thick clad sheets		
	Flat clad layer	68 ± 9	200
	Riblets	78 ± 6	47
	Substrate before riblet rolling	223 ± 14	381
	Substrate after riblet rolling	232 ± 16	22
	1.6 mm thick clad sheets		
	Flat clad layer	75 ± 10	171
	Riblets	83 ± 11	39
	Substrate before riblet rolling	219 ± 26	174
	Substrate after riblet rolling	246 ± 19	26
AA 7075	**2 mm thick clad sheets**		
	Flat clad layer	71 ± 10	59
	Riblets	93 ± 10	45
	Substrate before riblet rolling	279 ± 26	129
	Substrate after riblet rolling	296 ± 40	59

no significant work hardening of the material due to the rolling process.

5.3 X-ray diffraction

While work hardening does not play a big role in the structuring process, the induced residual stresses are more considerable. The results of the corresponding XRD measurements are summarized in Table 5.3.

For the clad sheets, both 2024 and 7075, small compressive residual stresses were found in the clad layer. In those specimens, the riblet rolling generally increased the compressive stresses parallel to the rolling direction. For the 2 mm (1.6 mm) thick Alclad 2024 sheets, the measured residual stress changed from -17 to -44 MPa (-14 to -52 MPa), which means an increase by a factor of 2.6 (3.7). Normal to the rolling direction, a slight decrease in residual stresses from -17 to -13 MPa (-14 to -8 MPa) was observed. The same is true for Alclad 7075, where a change from -24

Table 5.3: Surface-near residual stresses determined in XRD experiments.

		Residual stress (MPa)
AA 2024	**2 mm thick bare sheets**	
	Flat material	-12 ± 8
	Flat material after mechanical polishing	-35 ± 7
	Riblets (parallel orientation)	-1 ± 7
	Riblets (normal orientation)	-
	2 mm thick clad sheets	
	Flat material	-17 ± 10
	Riblets (80 μm), parallel orientation	-44 ± 7
	Riblets (80 μm), normal orientation	-13 ± 1
	1.6 mm thick clad sheets	
	Flat material	-14 ± 9
	Riblets (300 μm), parallel orientation	-52 ± 11
	Riblets (300 μm), normal orientation	-8 ± 1
AA 7075	**2 mm thick bare sheets**	
	Flat material after mechanical polishing	1.5 ± 14.5
	2 mm thick clad sheets	
	Flat material	-24 ± 1
	Riblets (100 μm), parallel orientation	-60 ± 11
	Riblets (100 μm), normal orientation	-25 ± 3

to -60 MPa (factor 2.5) occurred parallel and from -24 to -25 MPa normal to the riblet structure. Nevertheless, since the yield strength of CP Al is only few 10 MPa (depending on the amount of deformation), the residual stresses are considered not to be stable during cyclic loading and therefore not to have an effect on fatigue behavior.

In the case of bare AA 2024 sheets, small compressive residual stresses were found as well. Theses stresses completely vanish during the heat treatment after the rolling procedure, which was expected since the material was solution annealed before and precipitation annealed after the structuring process. (Measurements normal to the riblets could not be performed due to a texture, which strongly affected the XRD measurement.) Nevertheless, a different aspect in this context are residual stresses induced by the sample preparation procedure (cf. p. 23) Since for fatigue testing non-structured, bare faces were polished by hand additional compressive stresses were induced. Theses residual stresses, which were measured to be -35 MPa, were found to be stable during cyclic loading during a fatigue experiment at 130 MPa

for $4.25 \text{x} 10^9$ load cycles in a run-out specimen. Therefore, residual stresses have to be taken into account for the bare material when dealing with results of fatigue testing on bare AA 2024.

For bare AA 7075, a different polishing procedure was applied since the clad layer had to be mechanically removed first. The applied procedure, which uses a polishing table, exerted a smaller pressure on the surface than the preparation by hand. As presented in Tab. 5.3, induced residual stresses are negligible in this case, considering the relatively large error bar.

6 Ultrasonic fatigue

The key aspect of this study is the material behavior under ultrasonic fatigue tests in the HCF and VHCF regimes. The following chapter gives an overview on the experimental results as well as a discussion of the findings. It begins with the fatigue behavior of bare material, followed by the clad versions. The focus of this study lies on the 2024 alloy. Nevertheless, also measurements on AA 7075 were performed to demonstrate the transferability of the results to other high strength Al alloys. Beside the S/N-curves, a detailed examination of the underlying damage mechanisms was conducted in this context.

6.1 Bare material

The following sections describe the fatigue behavior of both bare AA 2024 and AA 7075 material in the flat as well as in the riblet structured case.

6.1.1 AA 2024

The S/N-curve for bare AA 2024 is presented in Fig. 6.1 and compared with literature data. The material shows a continuous transition from the HCF to the VHCF regime without an ultimate fatigue limit. Fracture occurs even up to some 10^9 load cycles. The S/N-curve shows a relatively small scatter, which is comparable with that of corresponding literate data. Mayer et al. [14] performed experiments on cylindrical specimens (gage diameter = 4 mm) taken from a sheet of 16 mm thickness parallel to the rolling direction. These results are in perfect agreement with measurements from Stanzl-Tschegg [11] on similar specimens. However, the S/N-curve for sheet material lies above these literature values.

One possible reason for this is the much smaller sheet thickness resulting in a different microstructure. Furthermore, also the different sample orientation compared to the rolling direction could have an influence on fatigue strength. Measurements in the present work were performed in transversal direction to be consistent, since riblet structures – which are studied later on – are always oriented in rolling direction

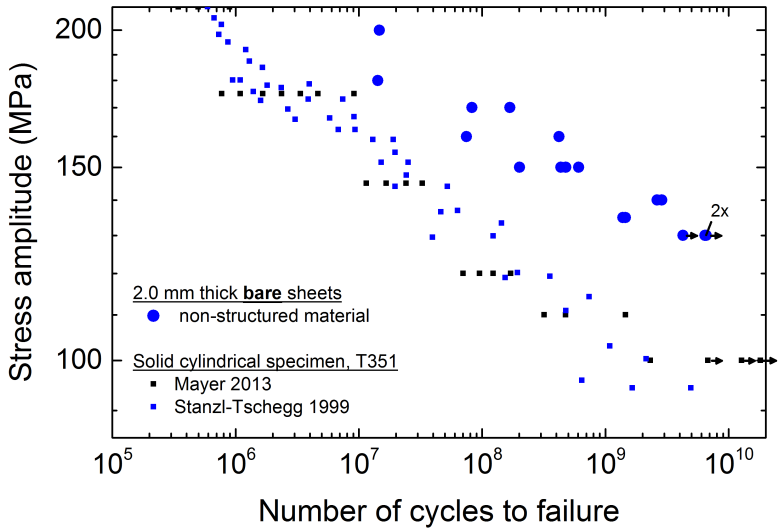

Figure 6.1: S/N-curve for flat AA 2024 bare sheets compared to literature data from Mayer [14] and Stanzl-Tschegg [11].

and load in active drag reduction systems is applied perpendicular to the riblet orientation. A third possible reason for the increased fatigue strength are the residual stresses after sample polishing (cf. p. 49). To estimate this influence, the Smith-Watson-Topper approach (cf. equation 2.10, p. 18) can be applied where residual stresses are considered as mean stress. As stated before, the residual stresses in flat bare material are stable during cyclic loading. The corrected data points (light blue points in Fig. 6.2) lie closer to the literature values.

Another option beside this quite general approach for the mean stress influence is the consideration of experimental data for the mean stress sensitivity from the study of Mayer et al. [14], who performed fatigue experiments on AA 2024 specimens at different load ratios. A Linear extrapolation of the values in the Haigh diagram (Fig. 9 in [14]) between $R = -0.1$ and $R = -1$ to $\sigma_m = -35$ MPa resulted in fatigue limits for 10^7, 10^8, 10^9, and 10^{10} load cycles which are indicated in Fig. 6.2 by horizontal red lines. Whereas the Smith-Watson-Topper approach shifts the experimental S/N-curve downward, the consideration of mean stress susceptibility shifts the literature values upwards. As can be seen, both approaches are in good agreement with each other and suggest that residual stresses cause around one half of the deviation between literature for cylindrical specimens and the results from the present study for flat AA 2024 sheet material.

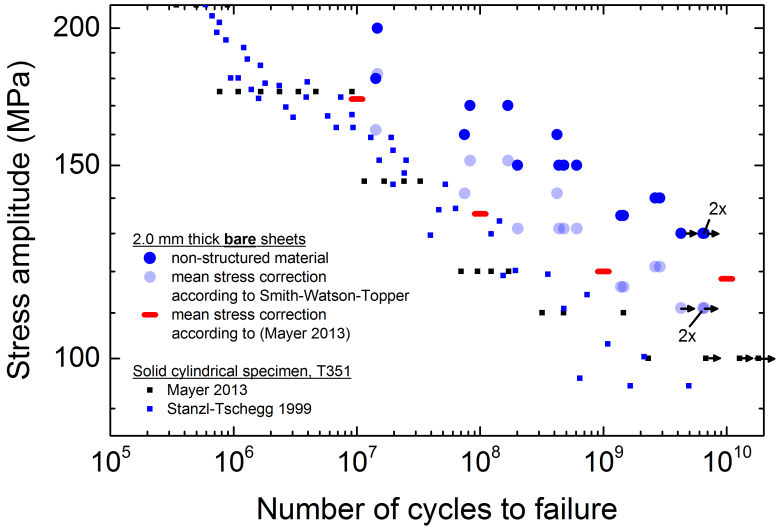

Figure 6.2: Correction of residual stress for flat AA 2024 bare sheets and comparison with literature data from Mayer [14] and Stanzl-Tschegg [11].

As a next step, the flat material is compared with the riblet structured one (riblet diameter = 100 μm). The respective S/N-data are summarized in Fig. 6.3 for both, riblets normal and parallel to the load direction. If riblets are oriented along the specimen, no notch effect occurs and the data are in good agreement with the mean-stress corrected values of the flat material. Nevertheless, riblets normal to the load direction show a distinct notch effect, which rises the local stress in the riblet valleys. Therefore, crack initiation in the HCF regime takes place in the riblet valleys and fatigue life is reduced by around one order of magnitude. However, in the gigacycle regime the notch effect does not have a strong influence. This becomes obvious, if a simple power-law is fitted to the S/N-data, i.e.

$$(\sigma_a)^n N_f = c, \tag{6.1}$$

with σ_a: stress amplitude, N_f: number of cycles for failure, and n, c: parameters of the power-law approximation. For the fitting procedure, the log of equation 6.1 was used. The results are summarized in Fig. 6.4 and in Tab. 6.1. As both fitting parameters are comparable, it is evident that riblets along sample direction do not affect fatigue behavior. Nevertheless, the S/N-curve for riblets perpendicular to the load direction declines much slower than the others pointing out the reduced sensitivity to notch effects at very high cycle numbers.

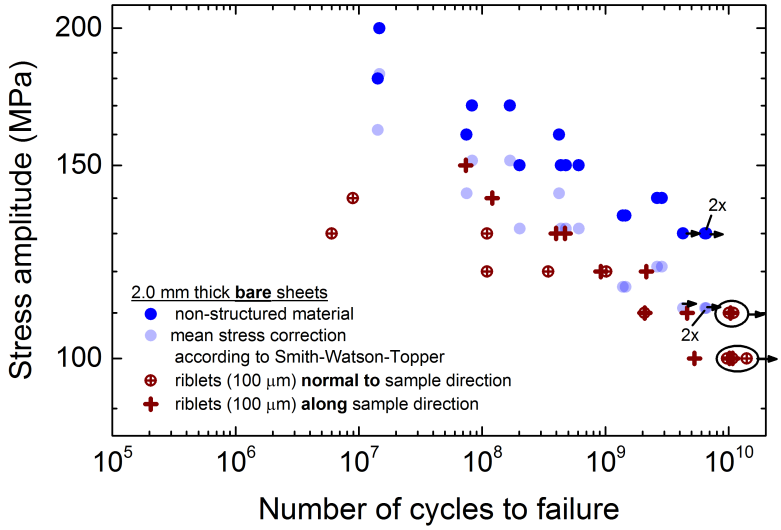

Figure 6.3: S/N data for flat and riblet structured bare AA 2024.

Table 6.1: Fit of power law to S/N data of bare AA 2024 material.

	n	$\log c$
Flat material	14.2 ± 1.7	89.4 ± 8.3
Riblets along load direction	13.5 ± 1.4	85.8 ± 6.8
Riblets normal to load direction	32.6 ± 8.4	176.0 ± 6.8

Table 6.2: Data for fatigue limit evaluation according to the arcsin $\sqrt{P}$-method.

	σ	$\sigma_{\text{S.W.T.}}$	# experiments	# fatigue failures
non-structured material	135 MPa	116.2 MPa	2	2
	130 MPa	111.1 MPa	3	0
riblets normal to sample direction	120 MPa	-	2	2
	110 MPa	-	3	1
	100 MPa	-	3	0
riblets along sample direction	120 MPa	-	2	2
	110 MPa	-	3	2
	100 MPa	-	3	1

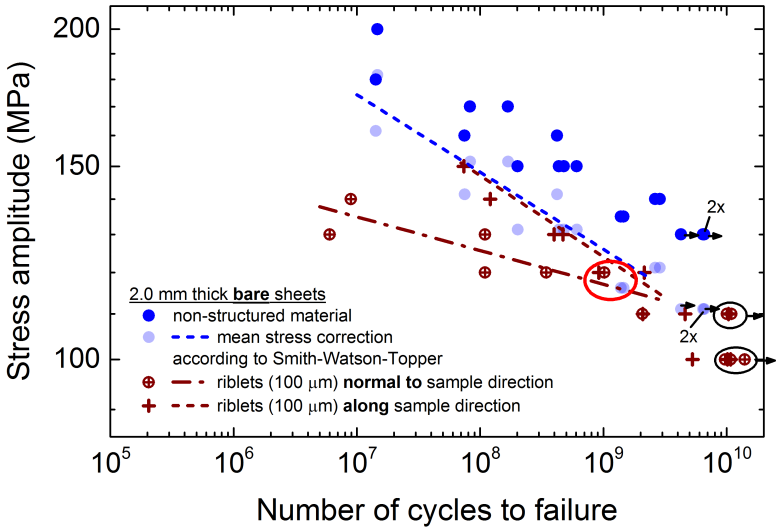

Figure 6.4: Fit of a simple power law (equation 6.1) to the S/N data for bare AA 2024 sheets.

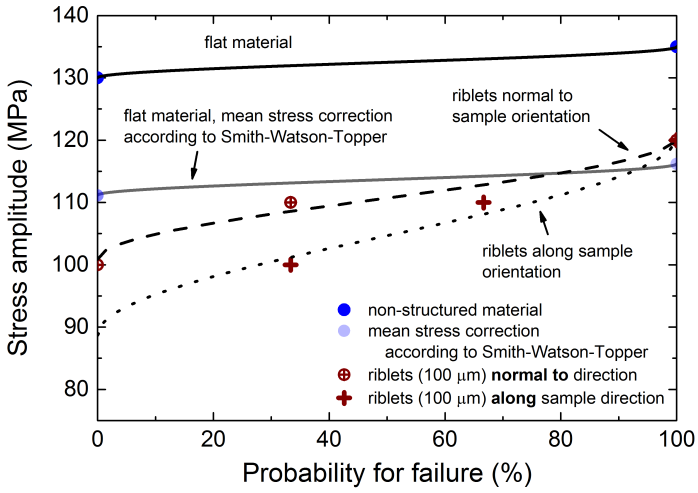

Figure 6.5: Statistical analysis according to the arcsin $\sqrt{P}$-method.

The reduced sensitivity to the notch effect becomes clear as well if one considers the failure probability according to the arcsin $\sqrt{P}$-method. The corresponding data are presented in Tab. 6.2 and graphically illustrated in Fig. 6.5. The stress level for 100% failure probability is nearly the same for flat and riblet structured material, irrespective of the riblet orientation. Nevertheless, if riblets are oriented along the load direction, i.e. in the absence of any geometrical notch effect, the failure probability at equal stress levels is even higher than for riblets normal to the load direction. Considering the limited statistics, it might appear to be doubtful that this effect will hold if significantly more measurements would be carried out in this region of the S/N-curve. Nevertheless, it clearly shows that – contrary to the HCF regime – the geometrical notch effect of the riblet structure does not govern VHCF life significantly.

Crack initiation in all specimens occurred at or near the specimens' surfaces. Typical surfaces planes are presented in Fig. 6.6 for flat and riblet structured material. In structured specimens, crack initiation always occurred on the riblet side. Cracks are of elliptical shape with quite low roughness compared to the tensile rupture which occurs when the two sides of the specimen are separated after testing. The characteristics of the fatigue crack are not influenced by the riblets and in both cases comparable with the observations by Mayer et al. [41] (cf. Fig. 2.5a, p. 10). In order to gain further insight on the failure mechanism, the surfaces of the gauge sections of the run-out specimens were carefully mapped by electron microscopy to identify possible crack initiation sites. At none of the specimens, microcracks could be observed. Therefore, a similar analysis was performed on failed specimens slightly above the fatigue limit (red encircled data points in Fig. 6.4). SEM pictures of the sample surfaces for a representative flat sample are given in Fig. 6.7a and b. Beside the fatal fracture, many other cracks were found in the gauge section of all four specimens, preferentially initiated at intermetallic phases which appear white in the images. EDX analyses at three different positions (indicated in Fig. 6.7b) are presented in 6.7c. The nearly identical EDX-patterns yield a chemical composition of the intermetallic phase of Al_2(Cu,Fe,Mn). The crack initiation at intermetallic phases at the surface agrees again with the findings of Mayer et al. [14].

Riblet structured specimens show a similar behavior, as presented in Fig. 6.8. Also the EDX spectra are comparable, even though a certain amount of oxygen was detected in addition, which could be attributed to the conducted T4 heat treatment in air. As can be seen in Fig. 6.7b for riblets along the load direction cracks are initiated all over the sample surface, which means also in the riblet tops. This is reasonable since there is no notch effect expected in this type of specimens. Nevertheless, also if riblets are oriented normal to the load direction, crack initiation is not limited to the riblet valleys but also occurs in the vicinity of the riblet tops close to intermetallic phases (cf. Fig. 6.7a). This fits well with the observation that there is no significant notch effect on the lifetime in the VHCF regime.

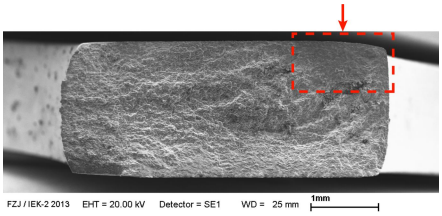

(a) Overview of fracture surface.

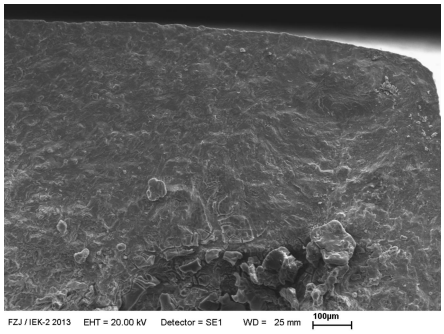

(b) Fatigue fracture from (a) at higher magnification.

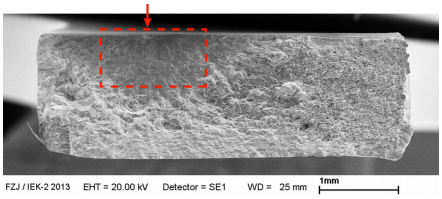

(c) Overview of fracture surface.

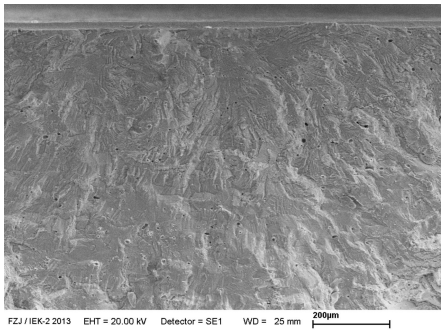

(d) Fatigue fracture from (c) at higher magnification.

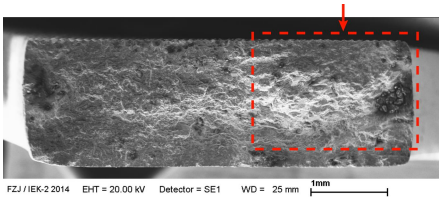

(e) Overview of fracture surface.

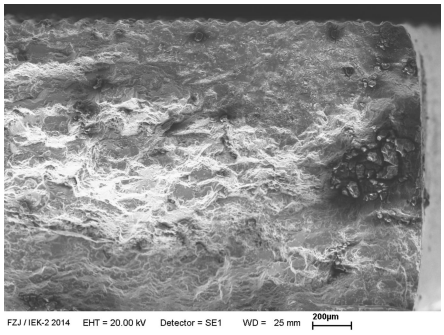

(f) Fatigue fracture from (e) at higher magnification.

Figure 6.6: Fracture surfaces of bare flat AA 2024 specimens. **(a)** and **(b)** Flat specimen tested at σ_a = 135 MPa ($\sigma_{\text{S.W.T.}}$=116.2 MPa), N_f = 1.38x10^9. **(c)** and **(d)** Structured specimen with riblets normal to load direction tested at σ_a = 110 MPa, N_f = 2.07x10^9. **(e)** and **(f)** Structured specimen with riblets along load direction tested at σ_a = 140 MPa, N_f = 1.21x10^8.

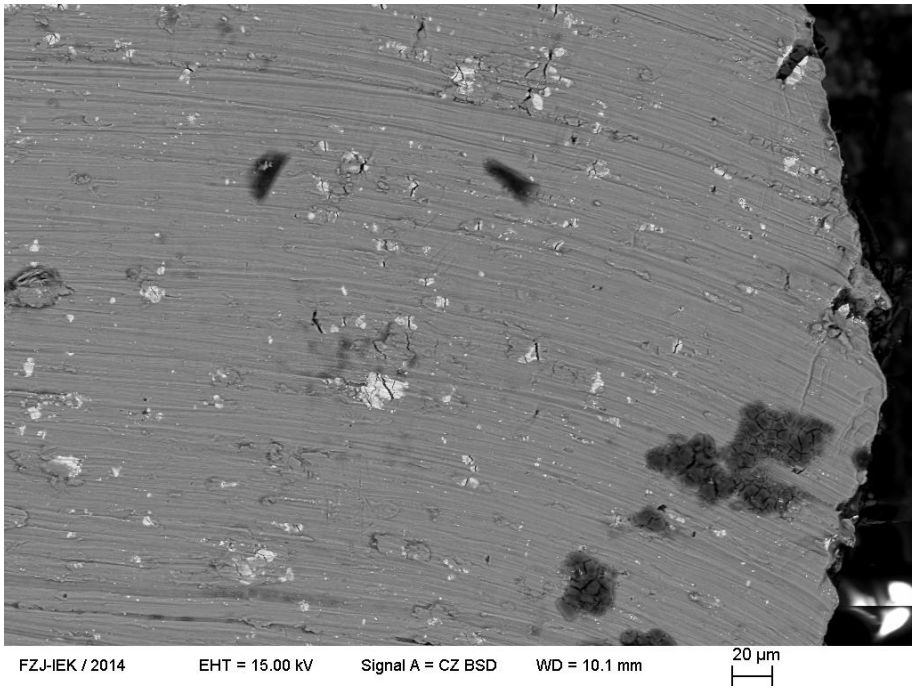

(a) Surface of the gauge length close to the fatigue fracture.

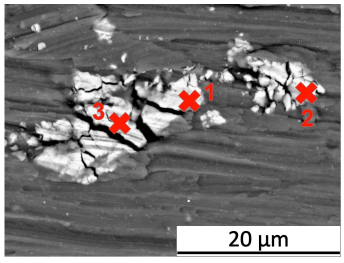

(b) Cracks at inclusions at higher magnification. The numbers indicate positions for EDX analysis.

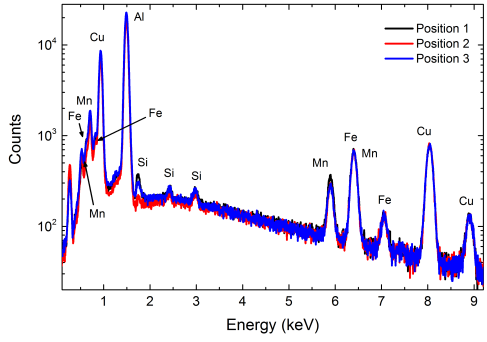

(c) EDX spectra of the surface inclusions, positions indicated in (b).

Figure 6.7: Analysis of crack initiation sites for a bare flat AA 2024 specimen tested at σ_a = 135 MPa ($\sigma_{\text{S.W.T.}}$=116.2 MPa), N_f = 1.38x10^9.

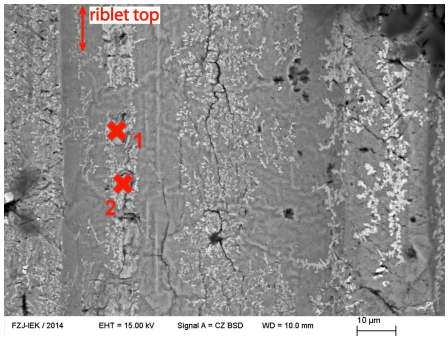

(a) Bare AA 2024 specimen with riblets normal to load direction, $\sigma_a = 120$ MPa, $N_f = 1.0\text{x}10^9$.

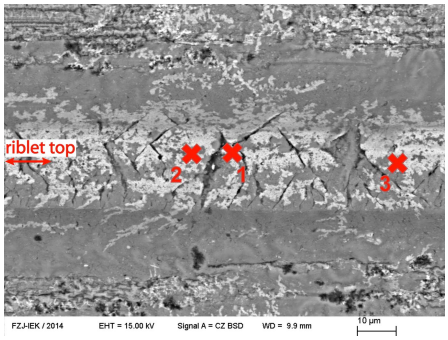

(b) Bare AA 2024 specimen with riblets along load direction, $\sigma_a = 120$ MPa, $N_f = 9.2\text{x}10^8$.

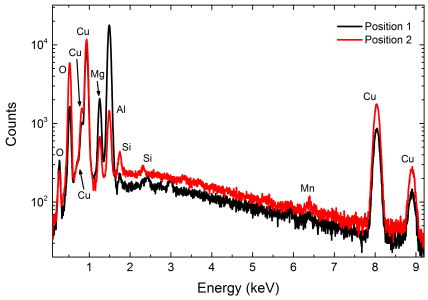

(c) EDX spectra for points indicated in (a).

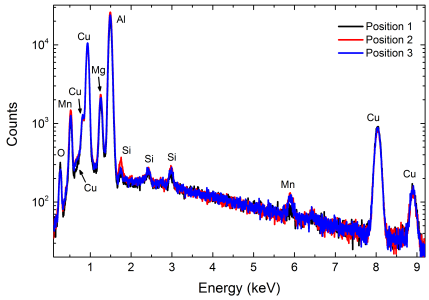

(d) EDX spectra for points indicated in (b).

Figure 6.8: Surface cracks at riblet structured bare AA 2024 specimens with different riblet orientation.

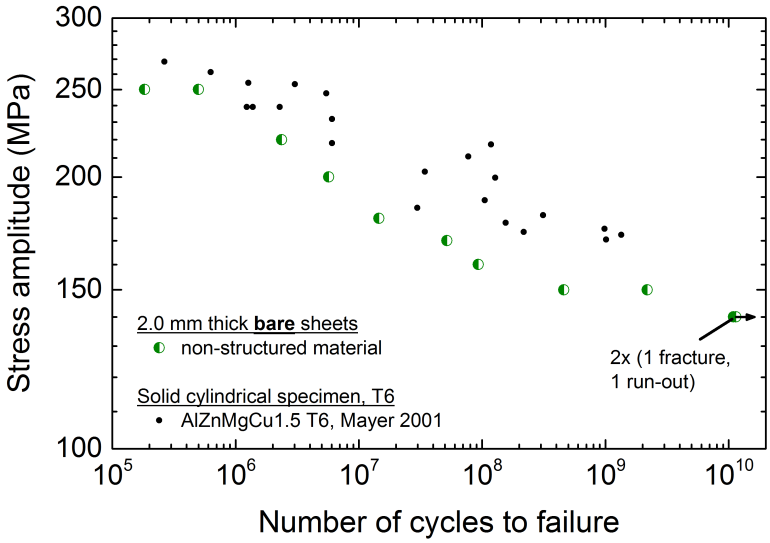

Figure 6.9: S/N-curve for flat AA 7075 compared to literature data for a similar alloy from Mayer et al. [15].

While the microcracks are possible crack initiation sites of macrocracks, they are of only very limited size. Polished cross sections were prepared from the same specimens and subsequently ground stepwise – where only a small amount of material was removed – in order to make the cracks visible. Despite careful preparation, in none of the four specimens any surface crack could be made visible. This leads to the conclusion, that fatigue life is dominated by one single fatal fracture which is in good agreement with the observation of single crack initiation on the fracture surfaces (cf. Fig. 6.6).

6.1.2 AA 7075

The S/N-data for flat AA 7075 bare sheets is presented in Fig. 6.9. As for AA 2024, a continuous transition from the HCF to the VHCF regime is observed. Furthermore, the scatter of the data is relatively small. The S/N-curve is slightly above the one for AA 2024 and slightly below measurements from Mayer et al. [15], who performed fatigue testing on the similar alloy AlZnMgCu1.5 on solid cylindrical specimens with a gauge diameter of 5 mm. Since specimens were prepared in another way than the 2024 material, residual stresses were only 1.5 MPa and can thus be neglected in this case. The fatigue limit for 10^{10} load cycles is around 140

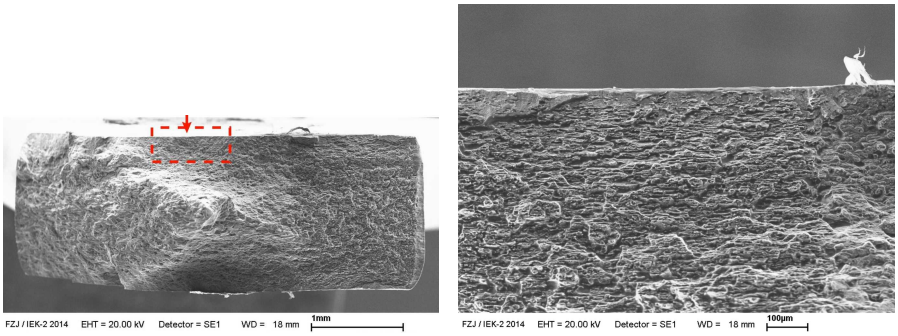

(a) Overview of fracture surface.

(b) Fatigue fracture from (a) at higher magnification.

Figure 6.10: Fracture surface of a bare AA 7075 specimen tested at $\sigma_a = 250$ MPa, $N_f = 1.83\text{x}10^5$.

MPa. As demonstrated in Fig. 6.10, fracture surfaces are less flat than for AA 2024. As for the 2024 alloy, fracture surfaces show only one single crack initiation site for all performed tests.

6.2 Clad material

Because of their high relevance in aerospace applications and easy producibilty in the applied flat rolling process – as stated earlier – three different types of clad sheets structured with a different riblet geometry were tested in the present work.

6.2.1 Alclad 2024

For Alclad 2024, two different types of clad sheets were studied. The sheets differed in thickness of the clad layer, in riblet dimensions, as well as in total sheet thickness (see Tab. 5.1, p. 43).

2 mm thick sheets

The first type of specimen was of 2 mm thickness with a relatively thin clad layer (cf. Fig. 4.4b, p. 39). The obtained S/N-curve for the non-structured material is presented in Figs. 6.11. The obtained data are in good agreement with the

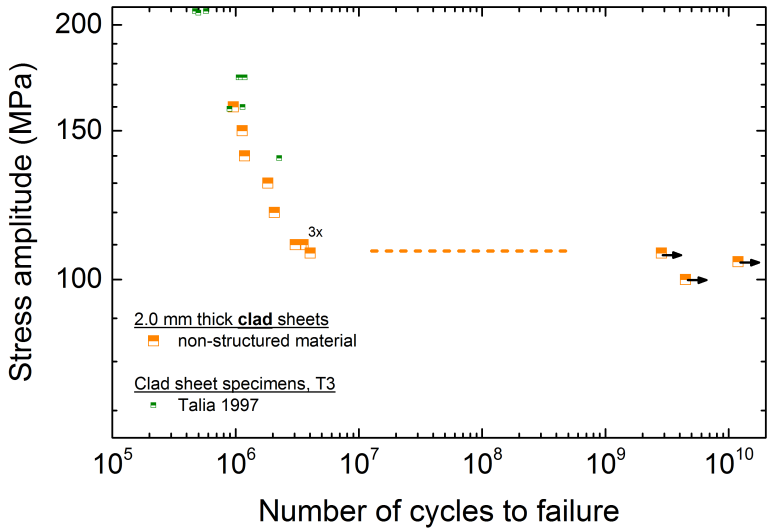

Figure 6.11: S/N-curve for 2 mm thick flat Alclad 2024 sheets and comparison to literature data from Talia and Talia [56].

study by Talia and Talia [56], who performed fatigue testing of Alclad 2024 sheets up to around 10^6 load cycles. The clad material generally shows a much shorter lifetime compared to bare material in the HCF regime. Furthermore, the S/N-curve decreases much faster. While for the bare specimens we found a continuous transition to longer lifetimes at lower stress levels (cf. e.g. Fig. 6.1), the clad material showed a sharp transition from early failure at around 3x10^6 load cycles to run-outs beyond several gigacycles at 107.5 MPa (orange dashed line).

The riblet structured specimens (riblet diameter = 80 μm), presented in Fig. 6.12, showed a similar behavior. In the regime of up to around 10^6 cycles to failure, lifetimes are comparable with the flat clad samples and a similar sharp transition from early failure to life beyond 10^9 cycles occured. However, in this case the transition threshold lied above the one of flat material (red dashed lines). This is at a first glance a surprising result since the notch effect of the riblets should result in a contrary behavior. The reasons for the opposite behavior are discussed below. Furthermore, the fatigue threshold level depended on the riblet orientation. It is higher for riblets in normal orientation (σ = 125 MPa) than for riblets along the specimens (σ = 115 MPa).

Representative fracture surfaces of failed specimens are presented in Fig. 6.13. Typically, cracks were initiated at the clad side, leaving an elliptical pattern with quite

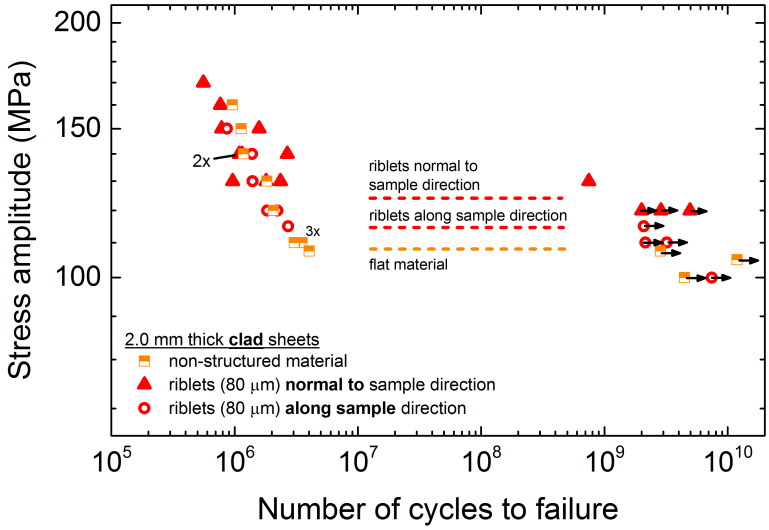

Figure 6.12: S/N-curve for 2 mm thick riblet structured Alclad 2024.

low roughness. Multiple crack initiation was observed in all conducted experiments.

If one compares run-outs with fractured specimens, as in Fig. 6.14, the failure mechanism for clad material becomes obvious. As stated in various studies on clad material [9, 10, 46, 136], cracks are observed to be initiated at the surface of the cladding and subsequently grow to the interface (substrate/cladding). In case of run-outs, cracks are blocked at the interface, even after several 10^9 load cycles. If the applied stress is high enough for fracture at some 10^6 load cycles, cracks can cross the interface and grow further into the substrate, where they induce failure.

In the case of flat material, no specific crack initiation point at the surface can be determined. Cracks occur at various locations at the cladding surface (cf. 6.14a and b). If the surface is riblet structured normal to the sample direction, cracks are exclusively initiated at the riblet valleys due to the notch effect. Apart from this, the failure mechanism is comparable with that of the flat material.

In addition to the standard S/N-curves, measurements of non-structured clad specimens at relatively low load amplitudes, as presented in Fig. 6.15a, were performed up to at least $2\text{x}10^9$ cycles in order to determine the threshold for crack initiation in the clad layer. Surface cracks were identified by optical and electron microscopy. As illustrated in the graph, the threshold for crack formation in the cladding lies

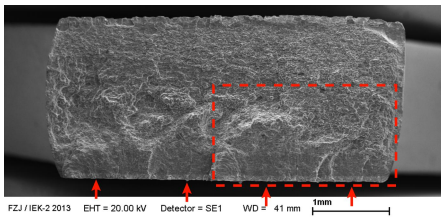

(a) Overview of fracture surface.

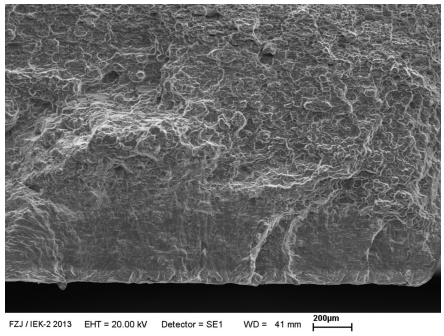

(b) Fatigue fracture from (a) at higher magnification.

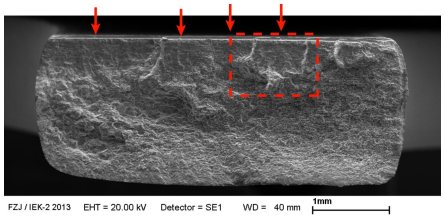

(c) Overview of fracture surface.

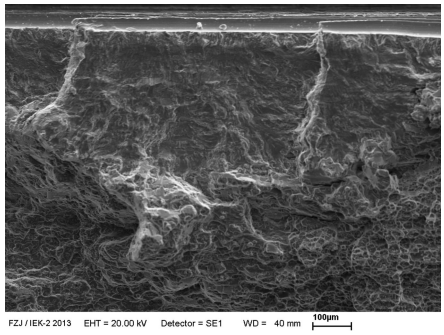

(d) Fatigue fracture from (c) at higher magnification.

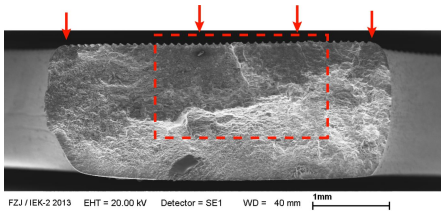

(e) Overview of fracture surface.

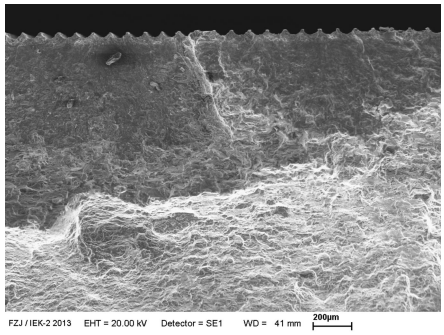

(f) Fatigue fracture from (e) at higher magnification.

Figure 6.13: Fracture surfaces of 2 mm thick Alclad specimens. **(a)** and **(b)** Flat specimen tested at $\sigma_a = 160$ MPa, $N_f = 9.58\text{x}10^5$. **(c)** and **(d)** Structured specimen with riblets normal to load direction tested at $\sigma_a = 140$ MPa, $N_f = 1.09\text{x}10^6$. **(e)** and **(f)** Structured specimen with riblets along load direction tested at $\sigma_a = 120$ MPa, $N_f = 2.22\text{x}10^6$.

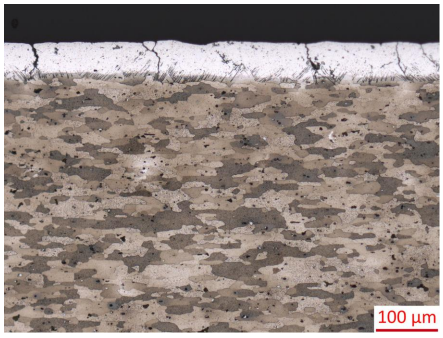

(a) Run-out flat specimen tested at σ_a=105 MPa for N=1.19x10^{10} load cycles.

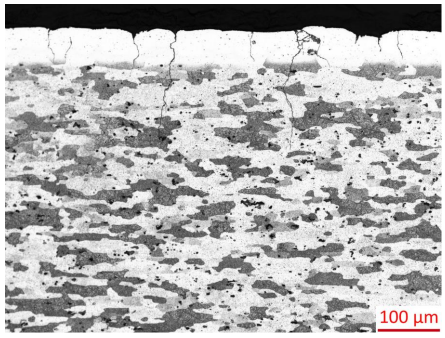

(b) Failed flat specimen tested at σ_a=150 MPa for N_f=1.13x10^{6} load cycles.

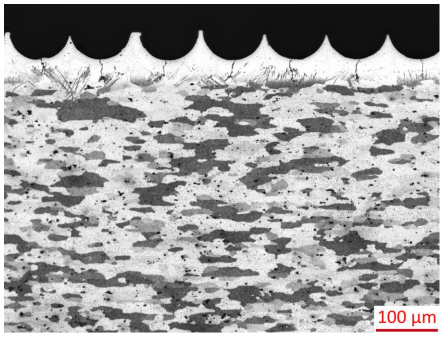

(c) Run-out structured specimen with riblets normal to load direction tested at σ_a=120 MPa for N=4.94x10^{9} load cycles.

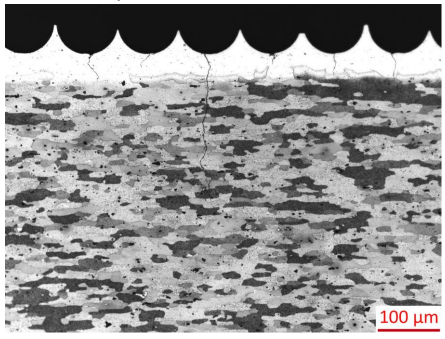

(d) Failed structured specimen with riblets normal to load direction tested at σ_a=140 MPa for N_f=1.09x10^{6} load cycles.

Figure 6.14: Polished cross sections of 2 mm thick Alclad 2024 material.

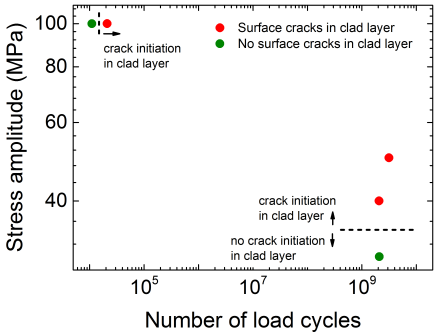

(a) Surface crack initiation in the clad layer.

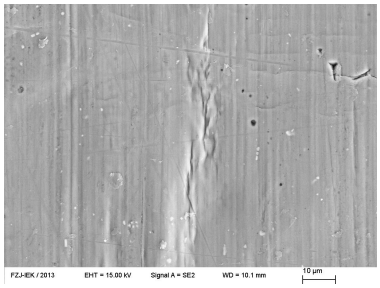

(b) Surface cracks on specimen tested at σ_a= 40 MPa for 2.07x10^9 load cycles.

Figure 6.15: Initiation of surface cracks in Alclad 2024 material.

between σ_a= 30 and 40 MPa. The surface of the specimen tested at 40 MPa is presented in Fig. 6.15b. The observed cracks have lateral dimensions of around 30 μm. Furthermore, for higher stress amplitudes surface cracks in the clad layer are initiated at a very early stage of fatigue loading. One sample tested at 100 MPa showed an undamaged surface at 1.1x10^4 cycles but many small fatigue cracks were found in the clad layer at 2.1x10^4 load cycles. Surface cracks are thus initiated at around 2% of total lifetime if the applied stress is close to the fatigue threshold level for failure. The early crack initiation in the cladding fits well with the observations by Hunter and Fricke [46], who observed crack initiation at around 1% of total lifetime in nominally the same material.

1.6 mm thick sheets

The second type of Alclad 2024 specimen was of 1.6 mm thickness with a relatively thick cladding layer (cf. Fig. 4.4c, p. 39). The respective S/N data are presented in Fig. 6.16 and again fits nicely to the study by Talia and Talia [56]. The qualitative behavior is similar to that of the thicker sheets, i.e. there was a strongly decreasing S/N-curve in the megacycle regime, followed by a sharp transition to life beyond several gigacycles. Quantitatively, the threshold value was with 95 MPa slightly lower than in the previous case. The riblet structure again did not affect fatigue life in the megacycle regime but, as before, raised the fatigue threshold by around 5 MPa to 100 MPa (cf. Fig. 6.17). Contrary to the 2 mm thick sheets, the threshold value for structured material did not depend on the riblet orientation.

Fracture surface, as presented in Fig. 6.18, are comparable to the thicker material in

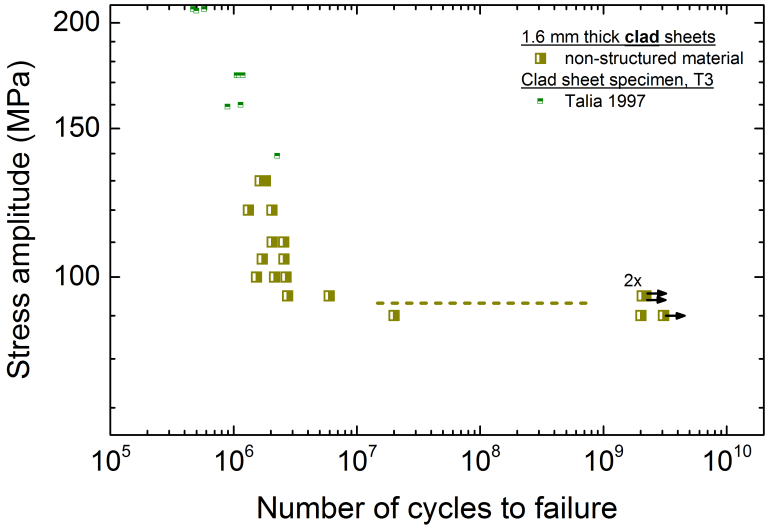

Figure 6.16: S/N-curve for 1.6 mm thick flat Alclad 2024 and comparision to literature data from Talia and Talia [56].

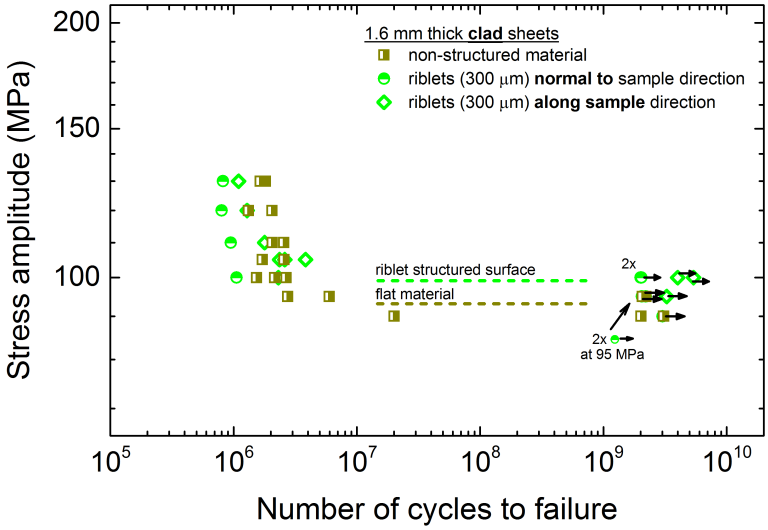

Figure 6.17: S/N-curve for 1.6 mm thick riblet structured Alclad 2024.

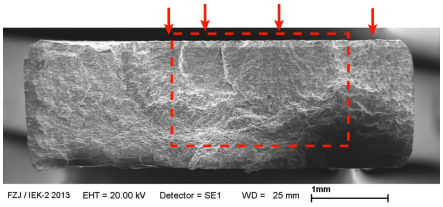

(a) Overview of fracture surface.

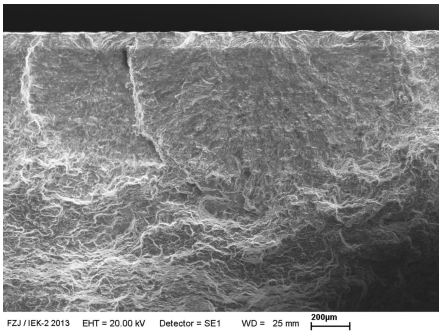

(b) Fatigue fracture from (a) at higher magnification.

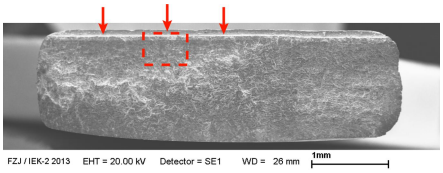

(c) Overview of fracture surface.

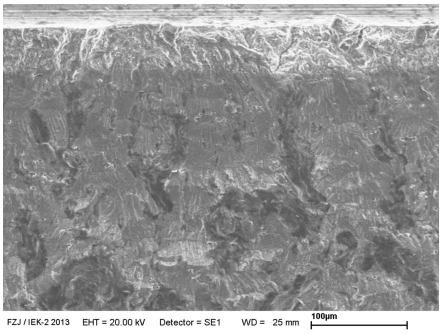

(d) Fatigue fracture from (c) at higher magnification.

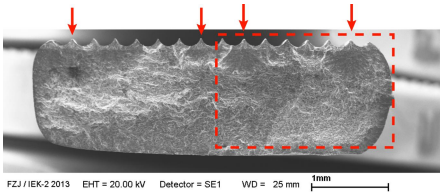

(e) Overview of fracture surface.

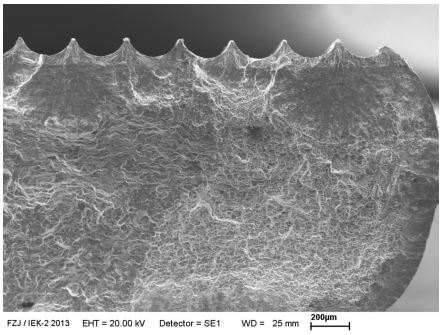

(f) Fatigue fracture from (c) at higher magnification.

Figure 6.18: Fracture surfaces of 1.6 mm thick Alclad 2024 specimens. **(a)** and **(b)** Flat specimen tested at $\sigma_a = 105$ MPa, $N_f = 1.71\text{x}10^6$. **(c)** and **(d)** Structured specimen with riblets normal to load direction tested at $\sigma_a = 100$ MPa, $N_f = 1.06\text{x}10^6$. **(e)** and **(f)** Structured specimen with riblets along load direction tested at $\sigma_a = 110$ MPa, $N_f = 1.78\text{x}10^6$.

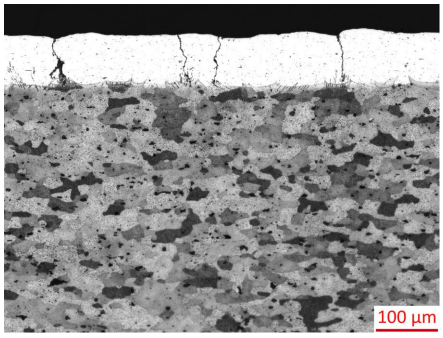

(a) Run-out flat specimen tested at σ_a=95 MPa for N=2.07x10^9 load cycles.

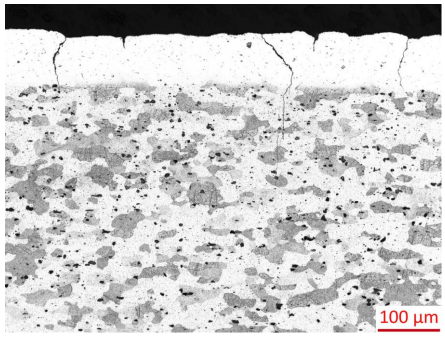

(b) Failed flat specimen tested at σ_a=120 MPa for N_f=1.31x10^6 load cycles.

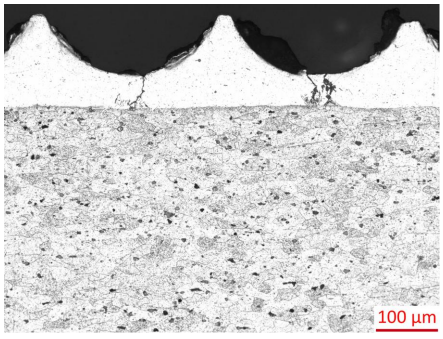

(c) Run-out structured specimen with riblets normal to load direction tested at σ_a=90 MPa for N=3.02x10^9 load cycles.

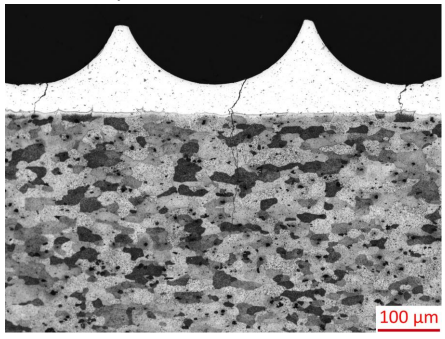

(d) Failed structured specimen with riblets normal to load direction tested at σ_a=120 MPa for N_f=8.01x10^5 load cycles.

Figure 6.19: Polished cross sections of 1.6 mm thick Alclad 2024 material.

the appearance of the fatigue fractures as well as in the fact that they typically show multiple crack initiation. Cracks were again initiated in the clad layer. Considering the polished cross sections as presented in Fig. 6.19, the same damage mechanism is observed for the 1.6 mm thick specimens. During cyclic loading, cracks grow from the cladding surface to the interface. Below the fatigue threshold stress in the S/N-graph, cracks are blocked at the interface. If the threshold stress is exceeded, cracks further propagate into the substrate, where they induce fatigue failure.

6.2.2 Alclad 7075

The third type of clad material evaluated in the present work were 2 mm thick Alclad 7075 sheets. The respective fatigue data is presented in Fig. 6.20. To the knowledge of the author, there is no S/N-data for comparison available in literature yet. As in the case of Alclad 2024, a steep decrease of the S/N-data in the megacycle regime was observed. Likewise, below a certain threshold value only run-outs up to several gigacycles occurred. Compared to both Alclad 2024 sheet types, the fatigue threshold for Alclad 7075 lies significantly lower between 75 and 80 MPa. In case of riblet structured material, presented in Fig. 6.21, no change in the megacycle regime occurred but a quite significant raise in fatigue threshold is observed. The

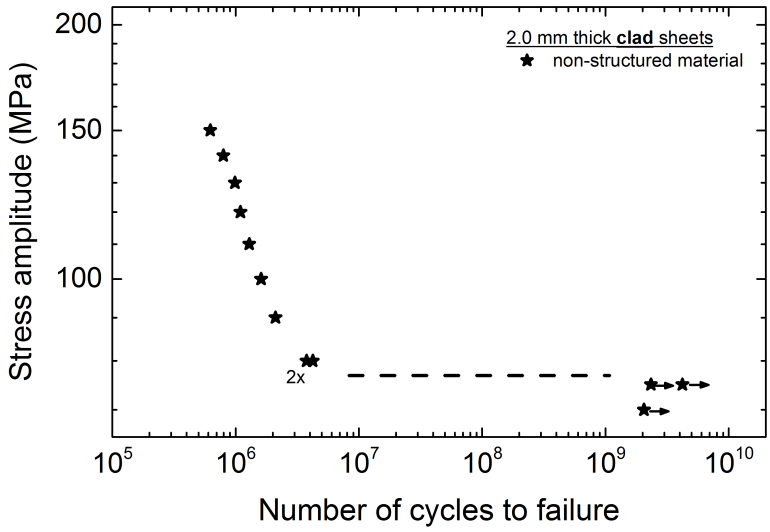

Figure 6.20: S/N-curve for 2 mm thick flat Alclad 7075.

structured material did not fail below a stress amplitude of 115 MPa, which means an increase in threshold stress by around 48%.

Typical fracture surfaces of Alclad 7075 are presented in Fig. 6.22. In all cases, multiple crack initiation, originating from the cladding surface, was observed. Cracks are of elliptical shape and of relatively low roughness. Generally, the forced fracture when breaking the samples after testing in tension are much rougher than for Alclad 2024. Fig. 6.23 presents polished cross sections of Alclad 7075, both run-outs and fractured specimens. It is obvious, that the same failure mechanism is present as in Alclad 2024. Cracks are initiated at the cladding surface and grow until the substrate. Only if the applied stress lies above the threshold value in the S/N-curve, they can cross the interface and induce failure in the substrate. Below the threshold value, cracks are blocked at the interface.

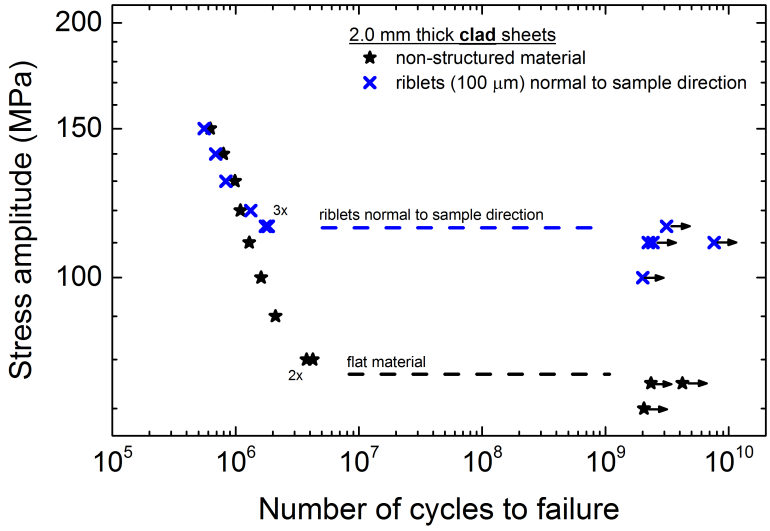

Figure 6.21: S/N-curve for 2 mm thick riblet structured Alclad 7075.

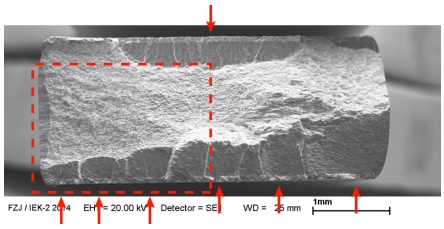

(a) Overview of fracture surface.

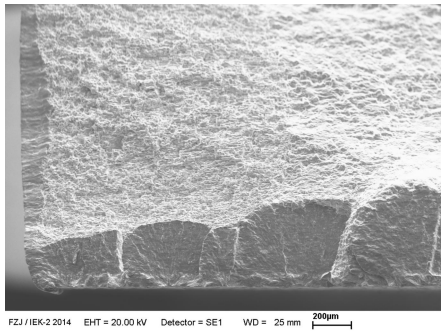

(b) Fatigue fracture from (a) at higher magnification.

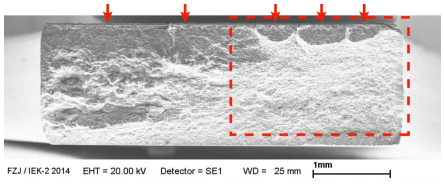

(c) Overview of fracture surface.

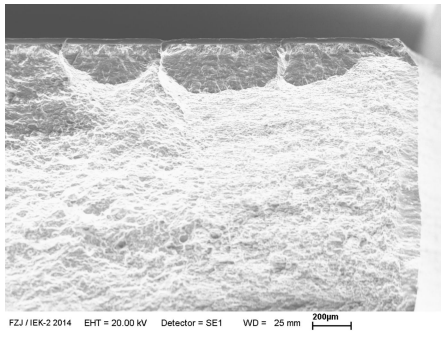

(d) Fatigue fracture from (c) at higher magnification.

Figure 6.22: Fracture surfaces of Alclad 7075 specimens. **(a)** and **(b)** Flat specimen tested at $\sigma_a = 120$ MPa, $N_f = 1.09\text{x}10^6$. **(c)** and **(d)** Structured specimen with riblets normal to load direction tested at $\sigma_a = 150$ MPa, $N_f = 5.55\text{x}10^5$.

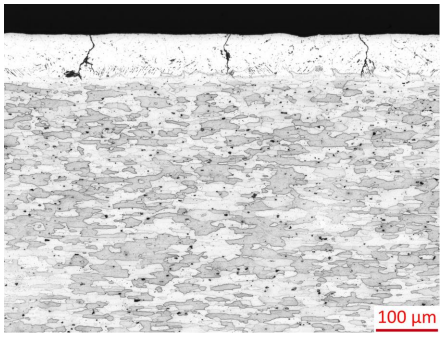

(a) Run-out flat specimen tested at σ_a=75 MPa for N=4.21x10^9 load cycles.

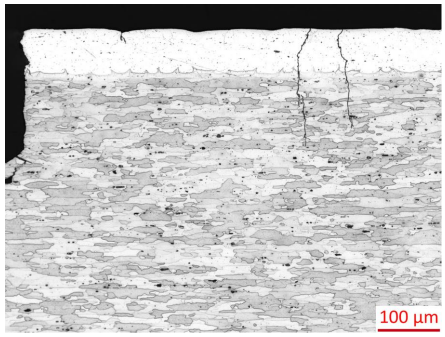

(b) Failed flat specimen tested at σ_a=80 MPa for N_f=4.22x10^6 load cycles.

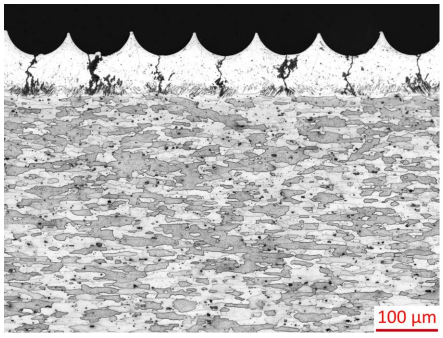

(c) Run-out structured specimen with riblets normal to load direction tested at σ_a=115 MPa for N=3.13x10^9 load cycles.

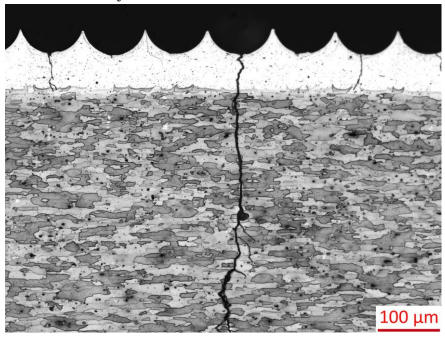

(d) Failed structured specimen with riblets normal to load direction tested at σ_a=120 MPa for N_f=1.33x10^6 load cycles.

Figure 6.23: Polished cross sections of 2 mm thick Alclad 7075 material.

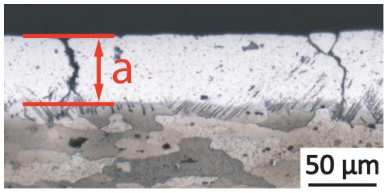

(a) Flat material.

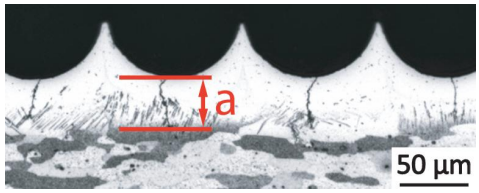

(b) Riblet structure normal to load direction.

Figure 6.24: Definition of the crack length as equal to the local cladding thickness.

6.2.3 Fracture mechanics approach

The different fatigue threshold values for different types of clad specimens can be understood by applying the Kitagawa-Takahashi approach as described in section 2.4 (p. 12). As stated above, cracks in clad material emerge at a very early stage of fatigue life at the outer surface of the cladding. During cyclic loading, these cracks propagate to the interface. Material failure only occurs, if cracks can overcome the interface and further propagate into the substrate.

For crack propagation, threshold values for different materials can be found in literature, as summarized in Tab. 6.3. Since the threshold value for the AA 1050 clad layer is relatively low compared to the substrates' values, crack propagation to the interface is observed in any case, if the applied load is close to the threshold value in the S/N-graph. The resulting crack length then equals the local thickness of the clad layer at the crack location, as indicated in Fig. 6.24. In the non-structured case, this is simply the cladding thickness. For riblet structured specimens, the cladding thickness at the riblet valley has to be taken as crack length. Experimental data for the cladding thickness are summarized in Tab. 6.4.

The resulting Kitagawa diagram for Alclad 2024 is presented in Fig. 6.25. For the specimen types, the same symbols are used like in the S/N-graphs. The El Haddad parameter was calculated according to equation 2.4 (p. 14) as 86.25 μm. For crack lengths below this value, the threshold stress for crack propagation equals

Table 6.3: Threshold values from literature for crack propagation for mode I cracks.

	$K_{\mathrm{max,\,th}}$	Reference
AA 2024	2.1 MPa$\sqrt{m}$	11
AA 7075	1.55 MPa$\sqrt{m}$	15
AA 1050	0.75 MPa$\sqrt{m}$	137

Table 6.4: Thickness of clad layers.

Flat Alclad 2024, 2 mm thick	(59 ± 4) μm
Riblet structured, 80 μm	(29 ± 5) μm
Flat Alclad 2024, 1.6 mm thick	(69 ± 3) μm
Riblet structured, 300 μm	(38 ± 4) μm
Flat Alclad 7075, 2 mm thick	(67 ± 4) μm
Riblet structured, 100 μm	(53 ± 4) μm

the fatigue limit (taken here at N $\approx 10^{10}$) of the bare material, since it is comparable to the substrate. For the fatigue limit of the substrate, the residual stress corrected values from Fig. 6.2 are used and therefore a value of 113.7 MPa is assumed. For crack lengths higher than the El Haddad parameter, the fatigue limit is continuously decreasing, as described by equation 2.5 (p. 14). The transition between microstructurally short and long crack growth can be described by the approximation proposed by El Haddad et al. [53] (equation 2.6, p. 14).

As can be seen, the experimental data is in good agreement with the theoretical predictions. For both sheet thicknesses, the riblet structure leads to an increased fatigue threshold level, which is in good agreement with the prediction using a locally reduced cladding thickness according to Tab. 6.4. Moreover, the influence of riblet orientation can be explained in the following way: in perpendicular riblet orientation, cracks are always initiated in the riblet valleys. Contrary, for riblets along the sample direction, cracks occur across the riblets at many locations in the gauge length. Therefore, one cannot calculate the stress intensity of through-cladding cracks using the remaining cladding thickness below the riblet valleys. Instead of this, an effective cladding thickness has to be used, which will be higher than the local thickness in the valleys, resulting in a higher stress intensity. If one assumes that for structured and flat specimens the same stress intensity threshold ($K_{\mathrm{max,th}}$) has to be exceeded for crack propagation into the substrate, the effective cladding thickness calculates as

$$a_{\mathrm{eff}} = \left(\frac{\sigma_{f,\,\mathrm{flat}}}{\sigma_{f,\,\mathrm{riblets}}} \right)^2 a_{\mathrm{flat}}, \tag{6.2}$$

with: $\sigma_{f,\,\mathrm{flat}}$ and $\sigma_{f,\,\mathrm{riblets}}$: fatigue threshold for flat material and riblets along the sample direction, respectively and a_{flat}: cladding thickness of the flat material. The resulting effective cladding thickness is 51.4 μm for 80 μm riblets and 58.8 μm for 300 μm riblets, respectively. As expected, these values and therefore also the fatigue thresholds lie between the ones for riblets normal to sample direction and the flat material. As presented in the Kitagawa-Takahashi diagram (Fig. 6.25), this

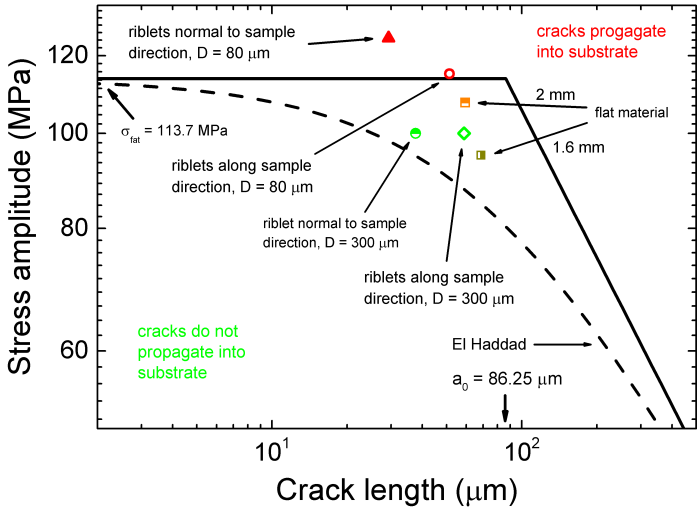

Figure 6.25: Kitagawa-Takahashi diagramm for Alclad 2024.

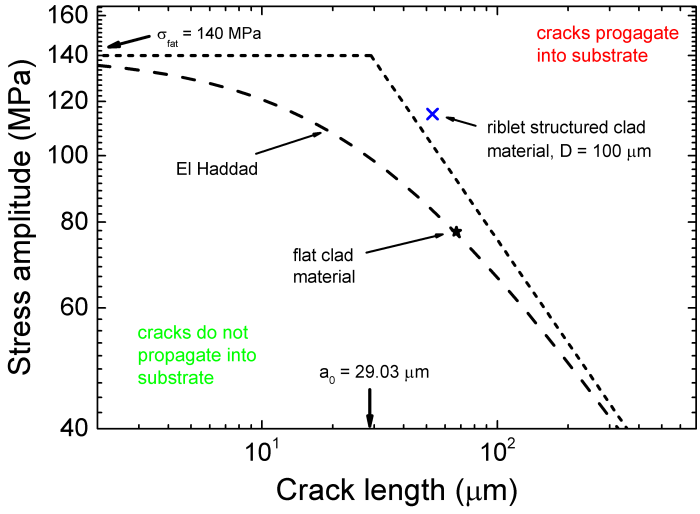

Figure 6.26: Kitagawa-Takahashi diagramm for Alclad 7075.

explanation holds nicely for the 80 μm riblets, where the observed threshold value perfectly fits to the predicted value. For the 300 μm riblets, theoretical prediction and experimental data still show an acceptable agreement.

A corresponding analysis for AA 7075 is presented in Fig. 6.26. The fatigue strength of the substrate is with 140 MPa significantly higher than for the 2024 alloy. Nevertheless, the lower stress intensity threshold value ($K_{\mathrm{max,\,th}} = 1.55$ MPa$\sqrt{m}$, cf. Tab. 6.3) reduces the El Haddad parameter to 27.06 μm. As before, the threshold values in the S/N data are in good agreement with the predicted values in the Kitagawa diagram. Furthermore, also here the tendency is obvious, that the riblet structure reduces the local cladding thickness and therefore leads to a shorter crack length in the the Kitagawa diagram.

The stress intensity, calculated as $K_I = 1.122\sigma\sqrt{\pi a}$, is obviously strongly influenced by the crack length. Nevertheless, it also depends on the occurring local stress amplitude at and close to the cladding/substrate interface. This issue will be addressed in the following chapter by performing finite element calculations of the induced stress levels at the interface.

7 Finite element simulations

The analysis of fatigue failure can be further supported by a finite element (FEM) analysis. On one hand, it can assess the geometrical influence of the riblet structure. On the other hand, it can account for the influence of the different layers in the case of clad material where the interaction of both surface structure and the different material layers plays an decisive role. The results of the FEM simulations are shown and discussed in the following sections.

7.1 Assumptions and modeling

FEM calculations were performed using the commercial software ANSYS [93]. The modeling covered four aspects: (i) the material data, (ii) the geometry, (iii) the meshing, and (iv) the boundary conditions.

Concerning the material data, Young's moduli from pulse excitation measurements were taken from Tabs. 4.2 and 4.6. Since fatigue testing was performed well below the yield strength of the bare material linear elastic behavior was assumed for non-plated sheets as well as for the substrates of clad material. Nevertheless, the CP Al clad layer was expected to show strong plastification at such amplitudes, since its yield strength lies between only 20 and 45 MPa, depending on the amount of cold working [139]. Therefore, for the soft Al cladding isotropic hardening was assumed as presented in Fig. 7.1 using the data from Ref. 138 which assumes a yield strength of 28 MPa. For small strain values, this resulted in a bilinear isotropic hardening behavior, as illustrated in Fig. 7.1b.

The geometry was modeled in 2D assuming plane strain conditions. For each specimen type the surface near region including one riblet was represented in the model. The depth to which the substrate was calculated was adapted to the riblet dimension. In the structured clad case it was twice the riblet diameter. Figure 7.2 presents the geometry model for both clad and bare material. In both cases the riblet shape was fitted to the shape observed on polished cross sections, which means a high form filling for clad and a lower one for bare material [134]. Furthermore, also the cladding thickness was extracted from polished cross sections (cf. Tab. 6.4, p. 77). Calculations were performed for all tested riblet geometries. For the meshing

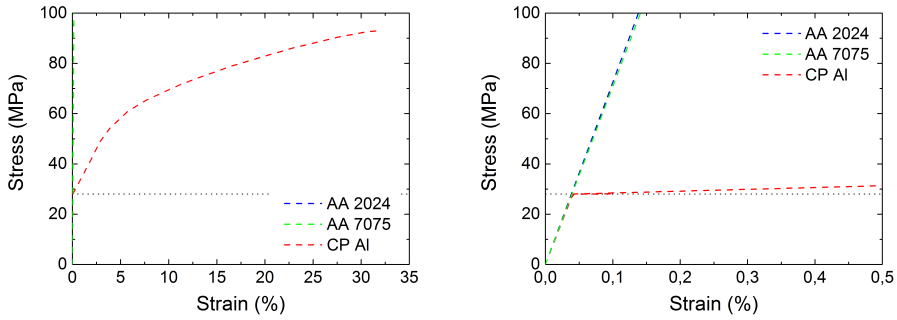

(a) Overview.

(b) Stress strain data for small strain values.

Figure 7.1: Literature data for stress-strain curves [138].

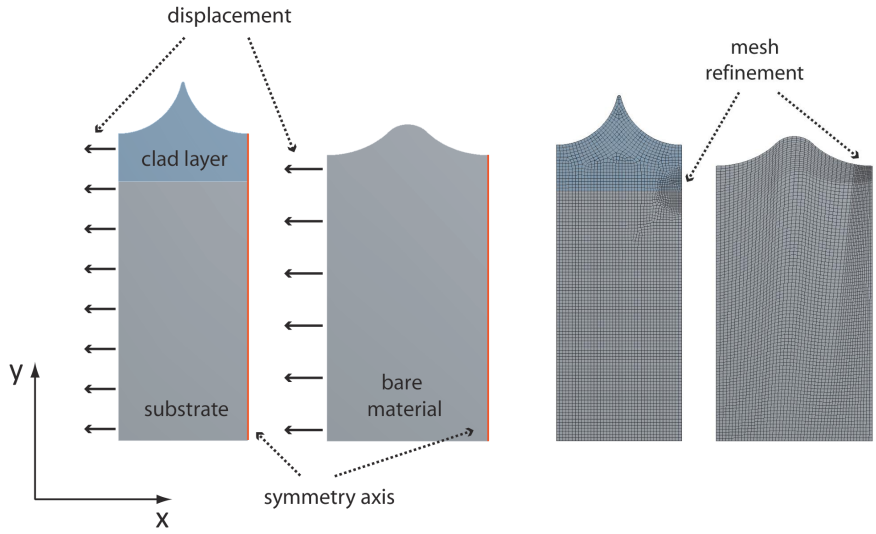

(a) Geometry and boundary conditions.

(b) Meshing.

Figure 7.2: Finite element model for influence of cyclic loading on stress redistribution in the cladding and substrate during cyclic loading. **(left)** Riblet structured 2 mm thick Alclad 2024 sheet. **(right)** Bare 2 mm thick bare sheets.

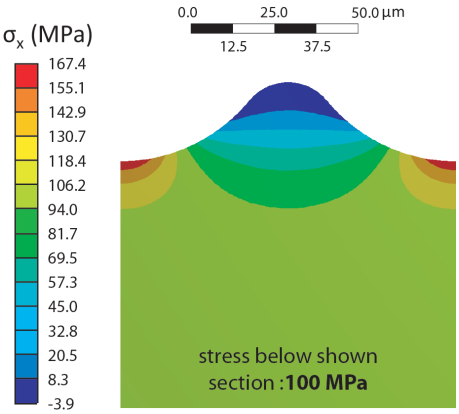

Figure 7.3: Local stress concentration due to the notch effect of the riblet structure.

quadrilateral elements with an edge length of 2 μm were used. In the vicinity of the interface (cladding/substrate) as well as in the riblet valleys of the bare material the edge length of the elements was refined to 1 μm (cf. Fig. 7.2b).

The specimens were exposed to an oscillating displacement on one side, assuming symmetric boundary conditions on the other side. For taking into account cyclic hardening and stress redistribution at the beginning of the test, 500 load cycles were calculated, which was sufficient for saturation in both the substrate and the clad layer as demonstrated in Fig. 7.7. The calculation in total used 10,000 iteration steps. The x component of the stress (σ_x) was used for analysis, since it is the relevant component for crack propagation. Stress levels were considered at maximum load during the corresponding load cycle. The stress amplitude in the substrate, sufficiently far away from the cladding/substrate interface, is referred to as 'nominal' stress amplitude. It was adjusted by choosing an appropriate displacement amplitude. Initial residual stresses in the cladding as determined by XRD measurements were neglected because of their instability due to the high plastic deformation (cf. section 5.3, p. 49).

7.2 Riblet structured bare AA 2024

The resulting stress distribution for structured bare AA 2024 is presented in Fig. 7.3. The displacement amplitude was chosen to adjust the nominal substrate stress to 100 MPa. As a consequence of the surface structure a local increase in stress by around 67.4% occurs. Therefore, cracks are preferentially initiated in the riblet valleys, as observed in the HCF regime during ultrasonic fatigue testing. The choice of 100 MPa nominal stress was arbitrary here, but since the bare material behaves

Table 7.1: Effect of stress redistribution on effective interface stress.

Specimen type	Riblet diameter	Nominal substrate stress $\widehat{=}$ fatigue threshold stress	Effective interface stress
Alclad 2024	80 μm	125 MPa	114.6 MPa
Alclad 2024	300 μm	100 MPa	121.6 MPa
Alclad 7075	100 μm	115 MPa	107.0 MPa

macroscopically fully elastic in the VHCF regime only the relative rise in stress is of potential interest. Especially in the HFC regime, the occurrence of the notch effect is well observed in the fatigue experiments. Nevertheless, despite this good agreement in the HCF regime stress concentration in the riblet valleys becomes less important after several gigacycles because – as discussed earlier – the existence of surface-near inclusions governs the fatigue behavior (cf. p. 54 ff.).

7.3 Riblet structured clad material

More complex than for bare sheets is the behavior of plated material where in addition to the geometric notch effect an interaction between the two layers comes into play. Since the yield strength of the CP Al clad layer lies far below the applied loadings during testing, plastification is expected. The resulting stress distribution in the cladding is presented in Fig. 7.4 for all three tested structured specimen types. The applied norminal stress was adjusted to the corresponding fatigue threshold levels in the S/N-curves ($\sigma_{\max}$= 125 MPa for 80 μm riblets in Alclad 2024, $\sigma_{\max}$= 100 MPa for 300 μm riblets in Alclad 2024, and $\sigma_{\max}$= 115 MPa for 100 μm riblets in Alclad 7075). The repeated mechanical loading induces a stress redistribution as a function of the cycle number. Fig. 7.4 summarizes the findings for N = 1, 5, 20, 50, 100, and 500 load cycles. As can be seen in all three cases, at some distance to the surface, below the riblet valleys a region of peak stress occurs. In case of relatively thick claddings (cf. Fig. 7.4a and c), the region of peak stress lies at a significant distance to the interface. Nevertheless, for the relatively thin cladding of the 300 μm riblets in Alclad 2024 (cf. Fig. 7.4b) this maximum coincides with the interface, which is quite harmful for fatigue performance as will be demonstrated in the following.

Since cracks in the cladding are initiated after a few 10^4 load cycles (cf. Fig. 6.15, p. 68) it is a valid assumption that the described stress redistribution in the cladding occurs well before crack initiation and is therefore not influenced by fracture of the material. As for bare sheets, the stress in clad material is locally raised in the

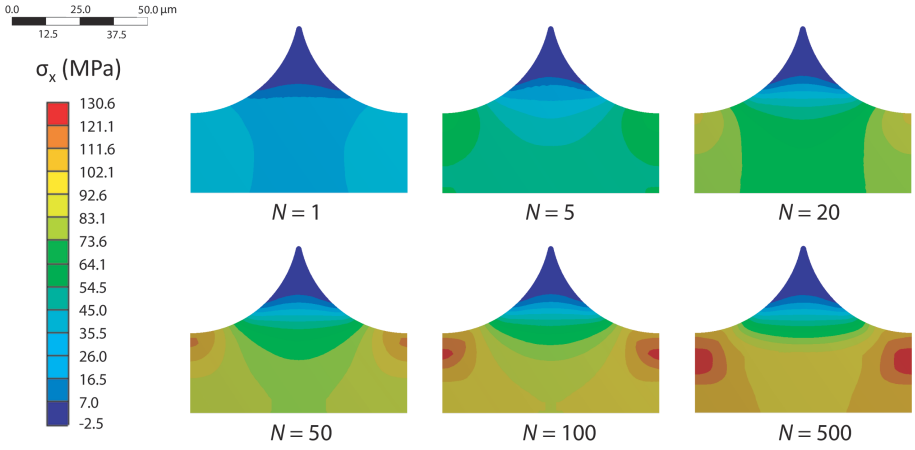

(a) 80 μm riblets in Alclad 2024.

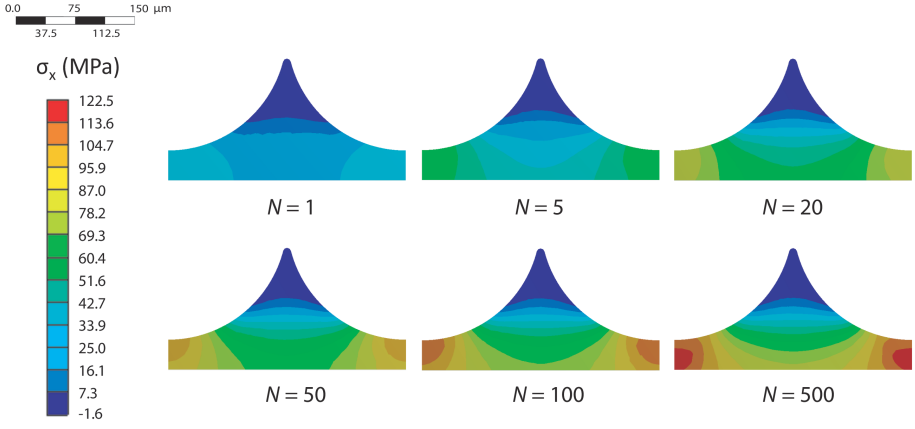

(b) 300 μm riblets in Alclad 2024.

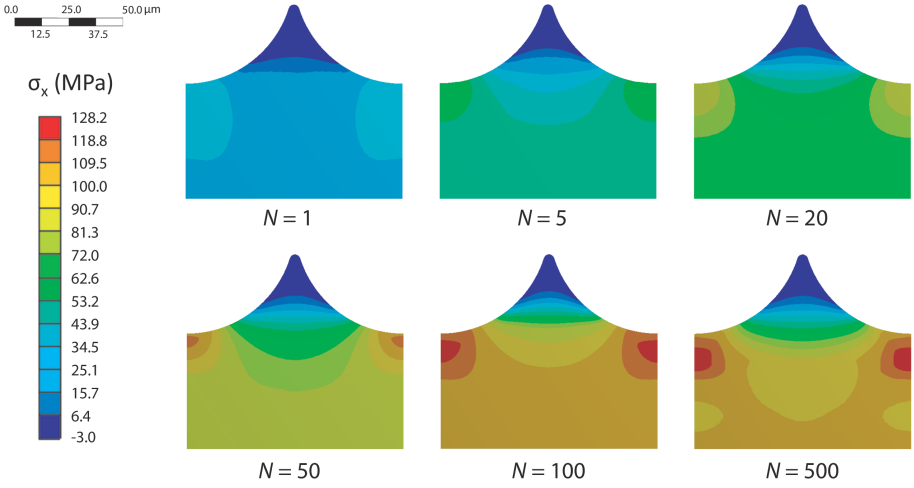

(c) 100 μm riblets in Alclad 7075.

Figure 7.4: Stress redistribution in structured clad layer during cyclic loading. N is the number of load cycles.

riblet valleys where consequently the highest surface stress is located. Since cracks are always initiated at the surface [46, 56, 136], crack initiation occurs exclusively at the riblet valleys and – as demonstrated by fatigue testing – grow easily to the interface. For further crack propagation from the cladding into the substrate the stress at the interface below the riblet valleys has to be considered. This stress is strongly influenced by the stress modification in the cladding and therefore referred to as 'effective' interface stress in the following. The resulting stress arrangements of the substrates of all three specimen types are summarized in Fig. 7.5 for maximum load during the 500th load cycle. For the relatively thick claddings in Fig. 7.5a and c, the region of peak stress is located sufficiently above the interface and therefore lowers the effective interface stress. Nevertheless, if the cladding is relatively thin (as in Fig. 7.5c), the region of peak stress coincides with the interface where it causes a local stress increase.

The effect of stress redistribution on the effective interface stress is summarized in Tab. 7.1. If these corrected stress threshold values are considered in the Kitagawa-Takahashi diagram (cf. 7.6), an even better agreement between measurements and predicted values is achieved. The fact that in one case, a change by more than 20% occurred demonstrates the significance of the stress correction by FEM simulations.

One last question address in this context would be how many load cycles are required in the simulation to reliably describe the influence of stress redistribution

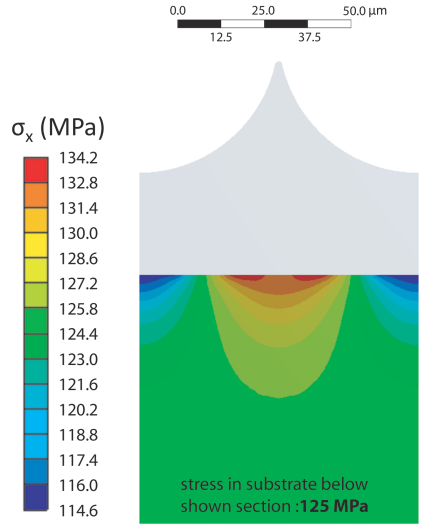

(a) Alclad 2024 with 80 μm riblets.

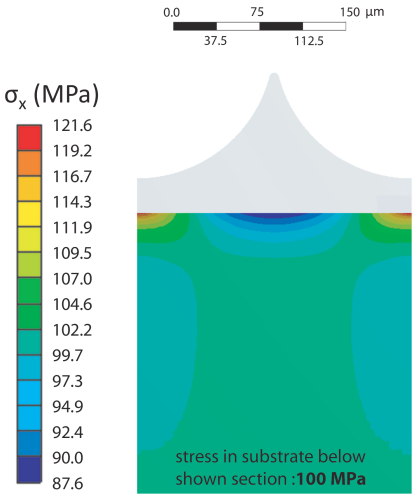

(b) Alclad 2024 with 300 μm riblets.

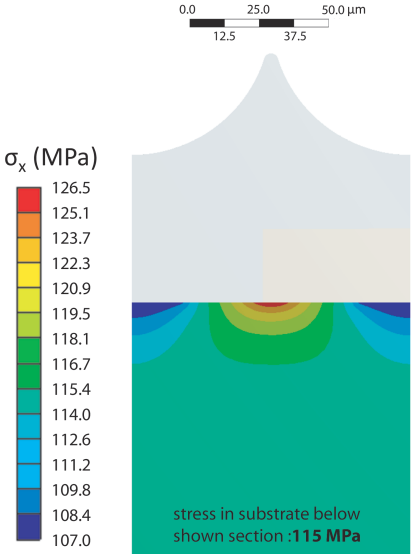

(c) Alclad 7075 with 100 μm riblets.

Figure 7.5: Effect of stress redistribution in the structured clad layer on substrate and interface stress during maximum load during the 500th load cycle.

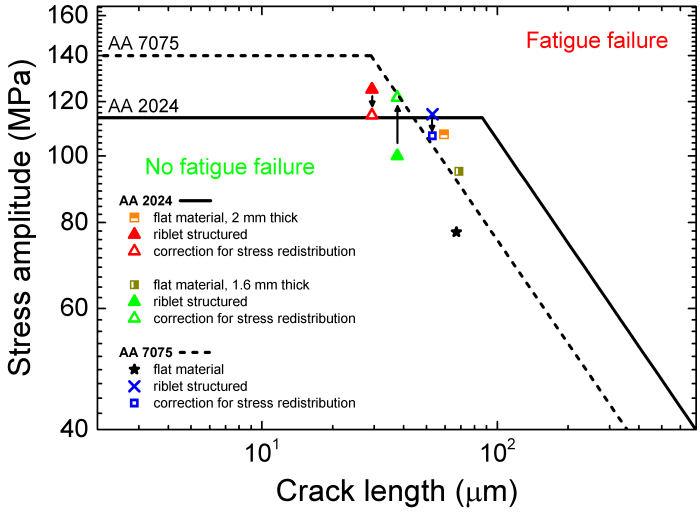

Figure 7.6: Kitagawa-Takahashi diagram accounting for correction of stress redistribution according to FEM calculations.

in the clad layer. To provide an answer to this issue, the evolution of the effective interface stress is presented in Fig. 7.7. As can be seen, the highest portion of the total change already occurs during the first 20 load cycles, followed by a further change of a few MPa during the next few 100 cycles. Nevertheless, after 300 loadings, saturation is achieved in all three cases. Therefore, the consideration of the first 500 load cycles – as done in this work – is sufficient to fully consider the stress redistribution due to the plastification of the clad layer.

7.4 Riblet optimization for Alclad material

The influence of cladding thickness and riblet geometry on stress redistribution raises the question of an optimum riblet geometry with respect to fatigue life. Therefore, a parameter study on the previously used FEM model was conducted as presented in Fig. 7.8. For each specimen type, the nominal substrate stress was adjusted to the fatigue threshold level. Then, the remaining thickness of the clad layer below the riblet valley – considered equal to the crack length (a) – was varied and the effective stress at the interface was calculated after 500 load cycles.

Fig. 7.9 summarizes the effective interface stress as a function of cladding thickness. For very thin clad layers, the interface stress is dominated by the notch effect of

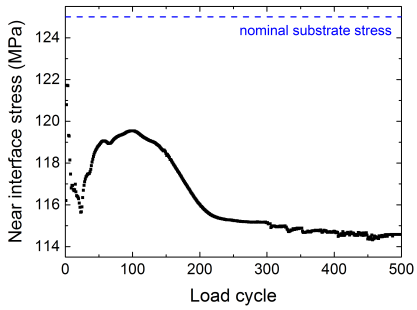

(a) Alclad 2024 with 80 μm riblets.

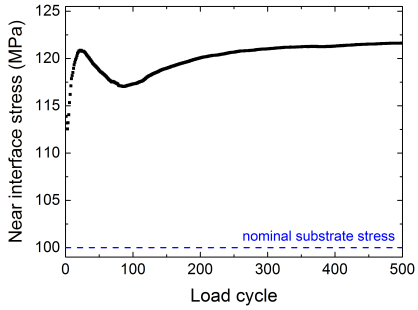

(b) Alclad 2024 with 300 μm riblets.

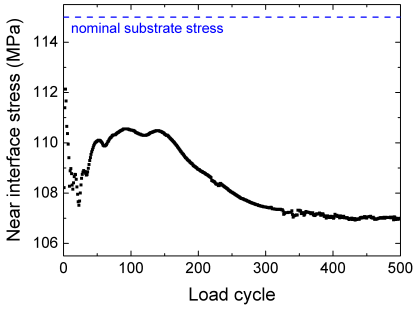

(c) Alclad 7075 with 100 μm riblets.

Figure 7.7: Saturation of stress redistribution in clad layer during cyclic loading.

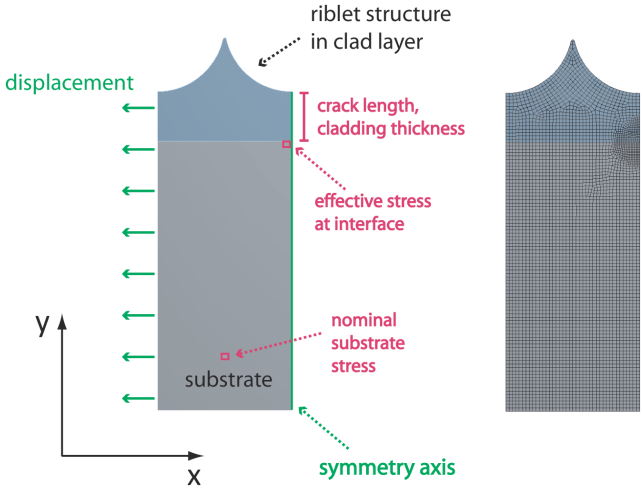

Figure 7.8: Modified FEM model for optimization of the riblet geometry for clad material.

the riblets, i.e. significantly higher interface stresses occur compared to the nominal substrate stress. If the cladding thickness below the riblets reaches around 1/4 of the riblet diameter, the interface stress equals the nominal substrate stress. For the 80 μm riblets in Alclad 2024 (Fig. 7.9a), there is a plateau region up to around 60 μm cladding thickness under the riblet valley where the interface stress is lowered by around 8.4%. For thicker clad layers, the interface stress rises again, even above the nominal level.

The 300 μm big riblets in Alclad 2024 have a slightly different influence on the effective interface stress. Again, for very small cladding thicknesses, the notch effect dominates and strongly raises the interface stress, and – as for the smaller riblets – the interface stress reaches the nominal substrate stress at a remaining cladding thickness of 1/4 of the riblet diameter. The minimum interface stress level, which is 2.3% below the nominal substrate stress, is reached at a cladding thickness below the riblet valley of $d = 120$ μm. For higher cladding thicknesses the interface stress asymptotically approaches to the nominal stress level.

The stress curve for the 100 μm large riblets in Alclad 7075 is qualitatively comparable with the one for the smaller riblets in Alclad 2024 (cf. Fig. 7.9c). In this case, the stress plateau lies around 7.5% below the nominal value. The stress raises again at around 80 μm and exceeds the nominal value when the cladding thickness approaches the riblet diameter. The difference in the shape of the stress curves (and thus the strength of the effect of stress redistribution) might be caused by the different nominal stress amplitude that leads to a different level of cladding plastification, which induces a different stress level in the clad layer and results in

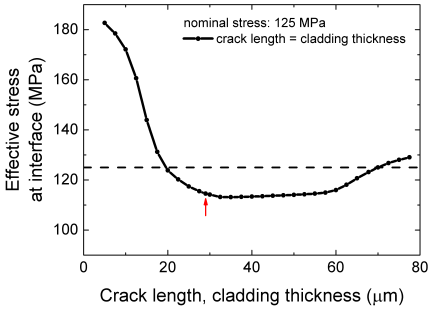

(a) Alclad 2024 structured with 80 μm large riblets.

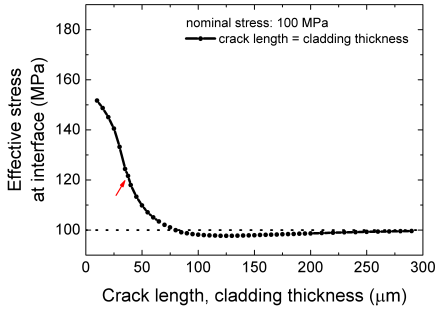

(b) Alclad 2024 structured with 300 μm large riblets.

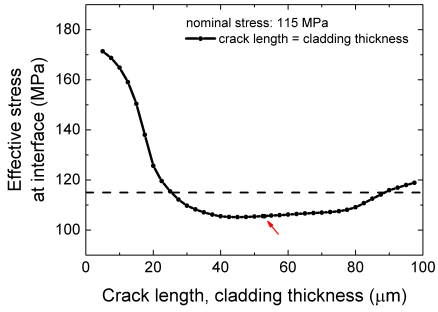

(c) Alclad 7075 structured with 100 μm large riblets.

Figure 7.9: Effective interface stress (σ_x) at nominal maximum stress during the 500th load cycle as a function of cladding thickness below the riblet valley. Red arrows indicate the cladding thickness of the material used in the experimental part.

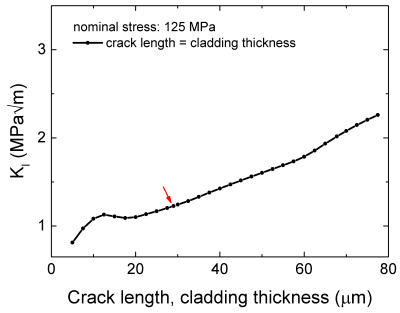

(a) Alclad 2024 structured with 80 μm large riblets.

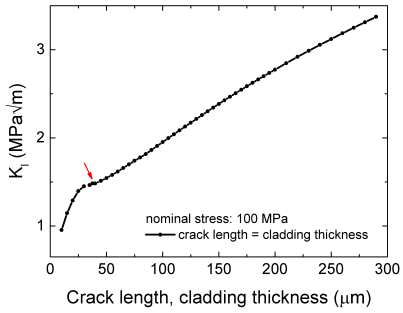

(b) Alclad 2024 structured with 300 μm large riblets.

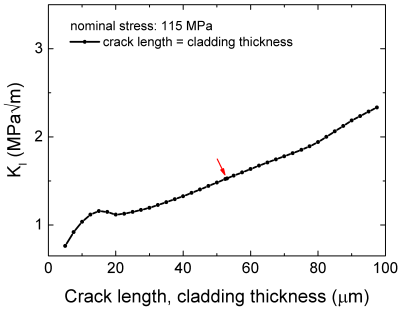

(c) Alclad 7075 structured with 100 μm large riblets.

Figure 7.10: Resulting stress intensity of cracks in the clad layer ranging from the riblet valley to the interface. Red arrows indicate the cladding thickness of the material used in the experimental part.

a different degree of stress modification at the interface.

The resulting stress intensities at the crack tip, calculated as $K_I = 1.122\sigma_x\sqrt{\pi a}$, are plotted for the three specimen types in Fig. 7.10. As mentioned before, a was assumed to be equal to the thickness of the clad layer below the riblet valleys. For σ_x, the effective interface stress from the FEM calculation was chosen. For both Alclad 2024 specimen types, the $K_{\text{max, th}}$-value for the cladding thickness from the experimental part (indicated by red arrows) lies significantly below the literature values for crack growth in AA 2024 (2.1 MPa$\sqrt{\text{m}}$, c.f. Tab. 6.3, p. 76) which fits well to the fact that the cladding thickness is well below the intrinsic length in the Kitagawa-Takahashi diagramm ($a_0 = 86.25$ μm, cf. 6.25, p. 78) and therefore fatigue crack growth is limited by the fatigue strength of the substrate (horizontal line in the Kitagawa diagram). For the tested Alclad 7075 specimens, the cladding thickness exceeds the intrinsic length ($a_0 = 29.03$ μm, cf. 6.26, p. 78) and therefore, contrary to the tested Alclad 2024 material, the $K_{\text{max, th}}$-value extracted from the simulation is in perfect agreement with the literature value of 1.55 MPa$\sqrt{\text{m}}$ (c.f. Tab. 6.3, p. 76).

Having a closer look at the shape of the K_I-a curves, a notable influence of the effective interface stress is observed. In all three cases, the stress intensity has a plateau value for $a = 1/4$ of the riblet diameter (d). If the cladding thickness if further increased, the higher stress intensity leads to an easier fatigue crack propagation into the substrate. Nevertheless, thinner remaining cladding thicknesses than $1/4\,d$ are not recommended due to the previously discussed notch effect and therefore, the optimum cladding thickness below the riblet structure is $a = 1/4\,d$.

8 Bending fatigue

Most fatigue tests of the present study were performed in axial loading at ultrasonic frequency. Nevertheless, material loading in active drag reduction system is not axial but flexural, and at a lower frequency of several 100 Hz. Therefore, the 5-point bending testings device, described in detail in section 3.2, was developed at the Central Institute for Engineering, Electronics and Analytics (ZEA-2, FZ Jülich) to ensure comparability with service relevant loadings. First bending fatigue tests were performed on 1.6 mm thick Alclad 2024 sheets with a riblet diameter of 300 μm (cf. Fig. 8.1). This type of specimen was chosen because bending actuation of thin sheets is easier than for thicker sheets.

Testing was performed at a frequency of around 100 Hz in pulse-pause mode to avoid overheating of the setup. During cyclic loading the displacement amplitude was found to be stable, as proven by a laser vibrometer. To prove the feasibility of the bending testing in the described setup, two measurements – at symmetric bending with a nominal surface stress amplitude of σ_a= 150 and 130 MPa – were performed. As can be seen in Fig. 8.2, the lifetimes fit well with the values from axial testing. Since both stress amplitudes are clearly above the fatigue threshold value, an early failure at slightly below 10^6 load cycles occurred.

The fracture surfaces of both specimens are presented in Fig. 8.3. As in the axial case, multiple crack initiation in the clad layer was observed. Since the applied stress amplitude is quite high in both cases, the clad layer is broken all along the complete sample width.

Figure 8.1: Polished cross section of a specimen used for bending testing. Experiments were performed on riblet structured 1.6 mm thick Alclad 2024 sheets with a riblet diameter of 300 μm. The specimens were of the same type like in Fig. 5.2d (p. 45).

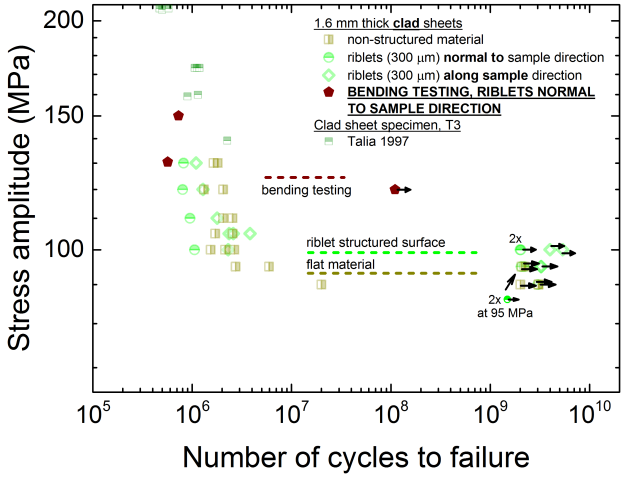

Figure 8.2: Bending fatigue data for riblet structured 1.6 mm thick Alclad 2024 sheets and comparison to fatigue data from axial testing as well as to literature data [56]. Bending testing was performed at 100 Hz.

One advantage of the bending testing compared to axial testing is the fact that the stress is not homogeneously distributed but there are different stress levels at different axial sample positions (cf. Fig. 3.12b, p. 29). Therefore, the stress level for crack initiation in the clad layer can be extracted by observing the surfaces of failed specimens. This analysis was conducted on the flat backside of the specimens (where differently to the axial fatigue tests the clad layer was not removed) since stress values did not have to be corrected by possible notch effects. Close to the fracture surface, many other surface cracks are observed. Nevertheless, at a higher distance to the maximum stress position, the surface crack density is drastically reduced until crack initiation does not occur anymore. The surface cracks most distant from the stress maximum are presented in Fig. 8.4. In both cases, they have a length of some 10 μm at the surface. Beside the crack, imprints of the riblet rolling equipment can be seen as well as surface scratches due to the low strength of the cladding.

Since the cracks are of quite small elongation, it is very likely to miss them when performing the same analysis on polished cross sections. Surface cracks were found up to a distance of 8.0 mm from maximum load for the specimen tested at 150 MPa and at 7.2 mm for the specimen tested at 130 MPa. The corresponding local stress levels at different specimen positions were determined in a FEM calculation

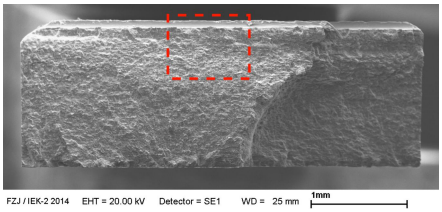

(a) Overview of fracture surface.

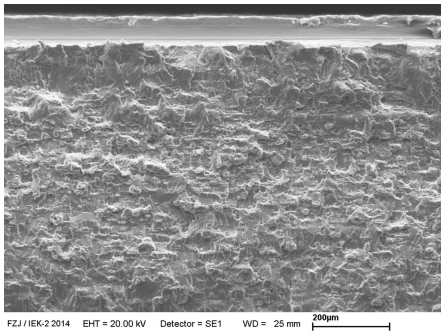

(b) Fatigue fracture from (a) at higher magnification.

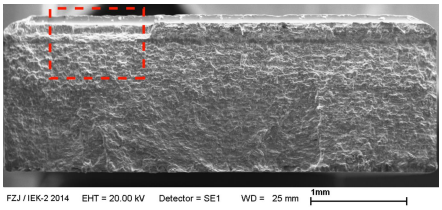

(c) Overview of fracture surface.

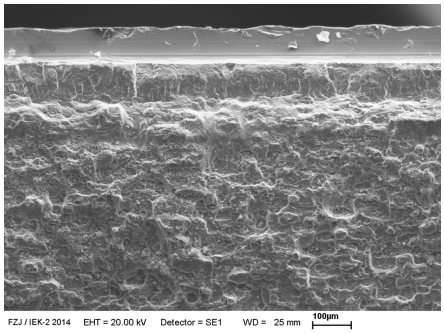

(d) Fatigue fracture from (c) at higher magnification.

Figure 8.3: Fracture planes of failed specimens from bending testing. **(a)** and **(b)** Specimen tested at σ_a= 150 MPa, N_f = 7.27x10^5. **(c)** and **(d)** Specimen tested at σ_a= 130 MPa, N_f = 5.67x10^5.

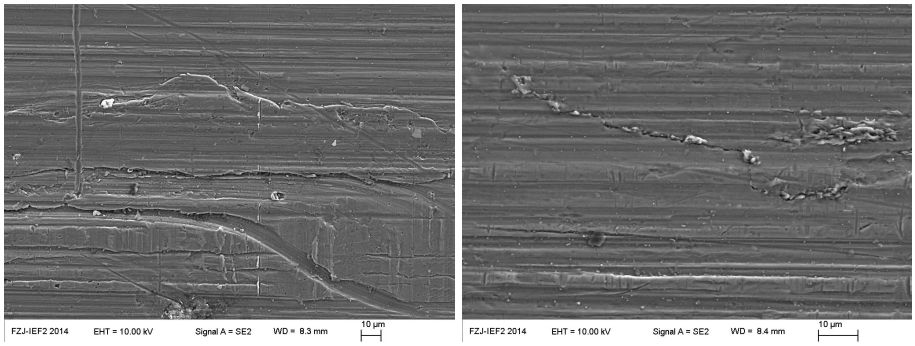

(a) Specimen tested at 150 MPa. **(b)** Specimen tested at 130 MPa.

Figure 8.4: Surface cracks found at most distant position from stress maximum.

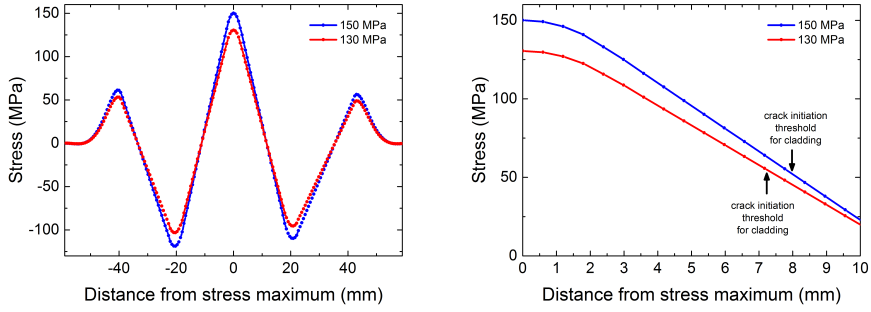

(a) Overview. **(b)** Region near the maximum stress.

Figure 8.5: Longitudinal stress distribution at maximum load in bending testing.

as presented in Fig. 8.5. The stress level at the observed crack was 52 MPa for the specimen tested at the higher load level and 55 MPa for the specimen tested at the lower load level. This value is slightly higher than the one found for flat 2 mm thick Alclad 2024 in axial loading, which showed crack initiation at a stress level between 30 and 40 MPa. Beside the different type of loading (axial vs. flexural), another reason comes into play: whereas the flat material in axial loading was a run-out specimen, tested up to $2\text{x}10^9$ load cycles, in bending testing the experiments could only be conducted until failure at some 10^5 load cycles. It is therefore possible that a significantly higher number of load cycles (several orders of magnitudes) would also lead to crack initiation at smaller stress amplitudes and therefore cracks could be observed at higher distances from the stress maximum in the specimen center.

A third bending test was performed at a load amplitude of σ_a= 120 MPa. No failure occurred up to N= $1.1\text{x}10^8$ load cycles. This clearly points at a threshold behavior as for axial loading. The resulting fatigue threshold stress is between 120 and 130 MPa and therefore a few 10 MPa higher than for axial loading.

To sum up, it can be stated that the failure mechanisms as well as the fatigue life time in the HCF regime are comparable for both, axial and bending loading. In both cases, cracks are initiated at the cladding surface and subsequently grow to the substrate where they induce failure, resulting in a threshold behavior of the S/N-curve. Also the crack initiation threshold for the cladding is comparable considering the mentioned reasons for the small deviation. It can therefore be concluded that the results from axial loading are of high relevance for the question of feasibility of aluminum alloy thin sheets in active drag reduction systems.

9 Summary and conclusions

The present work focuses on the fatigue behavior of the two wrought aerospace Al alloys AA 2024 T351 and AA 7075 T6. By using a flat rolling process developed at the Institute of Metal Forming (IBF, RWTH Aachen University) it is possible to produce riblet structured surfaces on a larger industrial scale. This process is designed to produce semi-circular riblets, which show a good performance for drag reduction. Whereas for clad material, the soft CP Al layer can be structured quite easily, bare material is too hard and the production process thus has to be aided by a further heat treatment, where the sheets are soft annealed prior the rolling process and subsequently precipitation hardened. The T4 state chosen for this purpose in the present work is comparable with the T351 temper with respect to hardness and tensile strength. By choosing the appropriate wire diameter, riblet dimensions can be adapted to the desired cruising speed of the aircraft. Possible riblet dimensions range from several 10 μm to a few 100 μm.

The structuring of clad material causes only slight work hardening and induces compressive residual stresses. Nevertheless, theses stresses were considered to not be stable because of the small yield strength of the CP Al clad layer. The work hardening shows a homogeneous lateral distribution along the riblets for clad material. For the bare material, the heat treatment during riblet production completely eliminates work hardening as well as residual stresses. Only small differences in hardness are observed which are attributed to slightly higher precipitation strengthening of the T4 compared to the T351 state.

Ultrasonic fatigue testing shows a continuous transition from HCF to VHCF for both bare alloys. A correction of residual stresses, induced during specimen preparation, according to Smith-Watson-Topper works well for AA 2024 and is in good agreement with an alternative correction approach which considers the mean stress sensitivity taken from literature. The S/N-curve for AA 2024 thin sheet material lies slightly above literature data for solid cylindrical specimens. Cracks are initiated at near-surface inclusions. On the surfaces of specimens which failed in the VHCF regime, various microcracks are observed, which are not found on polished cross sections and are therefore considered to not have further propagated during cyclic loading.

A riblet structure normal to the loading direction significantly reduces the fatigue strength of bare AA 2024 in the HCF regime. This geometric notch effect is most pronounced at lower cycle numbers ($N \approx 10^6 - 10^7$) and becomes less important with longer specimen lifetime, because in the VHCF regime, crack initiation is no longer limited to the riblet valleys but cracks are initiated everywhere on the surface, predominantly at inclusions.

For AA 7075, a different polishing procedure was applied which did not induce residual stresses. Also for this alloy, a good agreement with literature data is observed. Fracture surfaces show – as in the case of AA 2024 – only one single fatal crack but are – apart from the flat fatigue crack – generally of higher roughness than in AA 2024.

Especially clad material is of high technical relevance because of its improved resistance to corrosion. Plated sheets of both alloys – Alclad 2024 and Alclad 7075 – show comparable characteristic S/N-curves which strongly differ from those of bare sheets. In the HCF regime ($N \approx 10^6 - 10^7$), a steep decrease is observed. Nevertheless, below a certain stress threshold level, fatigue failure does not occur any longer up to several gigacycles. The crack initiation behavior for Alclad 2024 is in good agreement with literature up to a few 10^6 load cycles. Surface cracks are initiated at a very early stage of total lifetime and subsequently grow to the substrate where they induce failure. The threshold behavior can be understood by a fracture mechanics approach, where the cladding thickness is considered to equal the length of the surface cracks. Only if the stress intensity – which is a function of crack length and applied stress – exceeds the threshold for crack growth in the core material, cladding cracks can further propagate beyond the interface and induce failure of the specimen. The occurrence of surface cracks in the cladding is observed not only at low cycle numbers ($N \approx 10^4$) but as well at relatively low stress levels. For 2 mm thick Alclad 2024 sheets, crack initiation in the gigacycle regime is observed down to a stress amplitude of 40 MPa. The total sheet thickness only plays a minor role for clad material since the cladding – and therefore the length of the surface cracks – is much smaller than the overall sheet thickness and therefore the geometry factor of stress intensity – which is a function of crack length to sheet thickness ratio – can be assumed as constant.

The riblet structure in clad material does not negatively affect the lifetime in the HCF regime. Instead, it even increases fatigue performance of the specimens by raising the stress threshold level for fatigue failure. This behavior can be understood by the same fracture mechanics approach used to quantify the behavior of the flat clad material, since the fatigue threshold is governed by the cladding thickness. The riblet structure locally reduces the cladding thickness – and therefore the crack length – in the riblet valleys (which are the locations where cracks are induced) and therefore a higher nominal stress is required to overcome the stress intensity

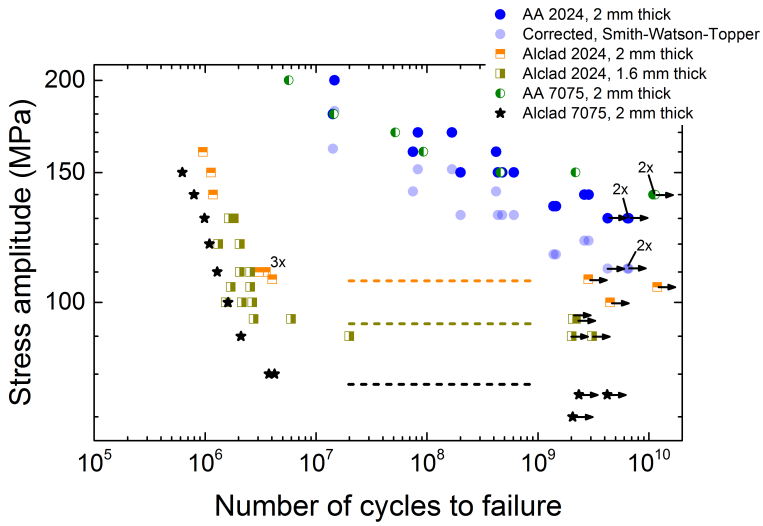

Figure 9.1: Summary of fatigue testing results for flat specimens.

threshold. The raise in threshold value was most pronounced for the Alclad 7075 sheets.

Beside the direct effect of cladding thickness, a second influencing factor on fatigue life is stress redistribution in the clad layer which is subject to pronounced plastic deformations during cyclic loading. An FEM calculation of stress evolution in the clad layer yielded that before cracks are initiated, a region of peak stress – located a few 10 μm below the surface of the riblet valleys – is induced. This region of higher stress contrary leads to a stress reduction further below the surface. Depending on the thickness of the clad layer, this stress arrangement can significantly modify the effective stress at the interface. In case of the studied 80 and 100 μm riblets it lowers the effective interface stress whereas for the 300 μm riblets it leads to a stress raise and therefore facilitates crack propagation into the substrate. The consideration of the stress distribution achieves an even better agreement of the observed fatigue threshold levels with predicted values from the fracture mechanics approach.

The thickness of the CP Al layer on clad material effects both, crack length and stress redistribution. While the crack length is equal to the total cladding thickness in case of flat, and equals the remaining clad thickness under the riblet valleys in case of the structured material, the stress redistribution is determined by the relative cladding thickness in comparison to the riblet dimensions. The interaction

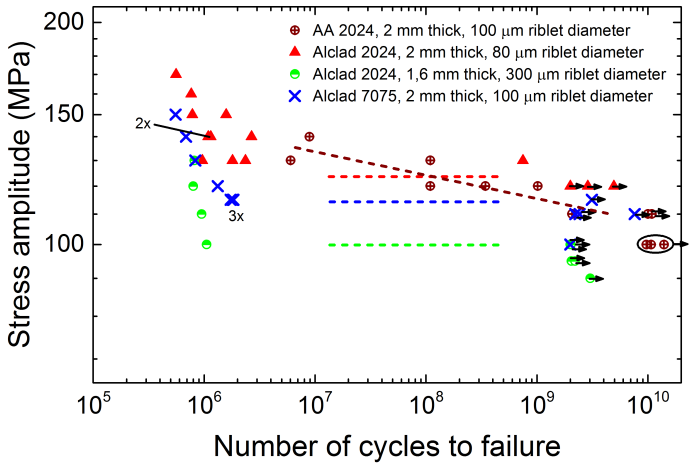

Figure 9.2: Summary of fatigue testing results for surface structured specimens with riblets normal to the loading direction.

of both effects raises the question of an optimal remaining cladding thickness below the riblet valleys. On one hand, if the cladding would be extremely thin, the crack length would be very short, keeping the stress intensity at a low level. Nevertheless, the local stress would be strongly increased in this case – even exceeding the fatigue strength of the bare material – which would effect crack initiation in the substrate. On the other hand, if the cladding would be too thick, the higher crack length in the cladding would result in high stress intensity factors and an easier crack penetration into the substrate. FEM simulations in the present study show that for all three tested specimen types, an optimum for the cladding thickness is achieved, if the remaining cladding thickness is 25% of the riblet diameter.

Beside the fatigue tests in axial loading a bending testing device was developed together with the Central Institute for Engineering, Electronics and Analytics (ZEA-2, FZ Jülich) which simulates the bending loading in the active drag reduction application. It turned out, that fatigue lifetime in the HCF regime is comparable with axial loading. Furthermore, the same damage mechanisms occur leading to a comparable threshold behavior in the S/N-curve.

As a final conclusion, a suggestion should be made which type of sheets should be preferred for the use in active drag reduction systems. Fig. 9.1 summarizes the S/N-curves for flat material. It is obvious, that the bare material has a higher fatigue

strength and should therefore be the preferred choice. Nevertheless, if one considers the riblet structured sheets – as in Fig. 9.2 – this suggestion can change if one focuses on the fatigue performance in the VHCF regime. If riblets are designed in a poor way, like the 300 μm large riblets which result in a quite low relative cladding thickness below the riblet valleys, the fatigue performance is still much below the structured bare sheets. Nevertheless, if riblets are designed in a optimized way, like the 80 μm large riblets, the stress redistribution lowers the effective interface stress and therefore reduces the interface stress intensity factor. Consequently, riblet structured clad material can outperform even riblet structured bare material. It is therefore a clear suggestion to use clad instead of bare sheets not only because of the easier producibility of riblet surface structures but also because of the higher fatigue performance in the VHCF regime if cladding dimensions are designed with care.

Bibliography

[1] G. Schrauf, B. Gölling, N. Wood. Key aerodynamic technologies for aircraft performance improvement. In 5th Community Aeronautical Days (2006).

[2] J. P. Marec. Drag Reduction: a Major Task for Research, volume 76 of *Notes on Numerical Fluid Mechanics (NNFM)*, chapter 3, pp. 17–27. Springer Berlin Heidelberg (2001).

[3] P. R. Viswanath. Aircraft viscous drag reduction using riblets. Progress in Aerospace Sciences **38** 6-7 pp. 571–600 (2002).

[4] D. W. Bechert, M. Bruse, W. Hage, J. G. T. Van Der Hoeven, G. Hoppe. Experiments on drag-reducing surfaces and their optimization with an adjustable geometry. Journal of Fluid Mechanics **338** pp. 59–87 (1997).

[5] Y. Du, G. E. Karniadakis. Suppressing wall turbulence by means of a transverse traveling wave. Science **288** 5469 pp. 1230–1234 (2000).

[6] G. Karniadakis, K.-S. Choi. Mechanisms on transverse motions in turbulent wall flows. Annual Review of Fluid Mechanics **35** 1 pp. 45–62 (2003).

[7] H. Zhao, J. Z. Wu, J. S. Luo. Turbulent drag reduction by traveling wave of flexible wall. Fluid Dynamics Research **34** 3 pp. 175–198 (2004).

[8] M. Itoh, S. Tamano, K. Yokota, S. Taniguchi. Drag reduction in a turbulent boundary layer on a flexible sheet undergoing a spanwise traveling wave motion. Journal of Turbulence **7** N27 (2006).

[9] J. Schijve, F. A. Jacobs. Fatigue Tests on Unnotched and Notched Specimens of 2024-T3 Alclad, 2048-T8 Alclad and 7178-T6 Extruded Material, Report TR68017 U. Nat. Aerospace Laboratory, Amsterdam (1968).

[10] P. R. Edwards, M. G. Earl, A. R. C. Britain. A comparative study of the fatigue performance of notched specimens of clad and unclad aluminium alloy, with and without a pre-stress. Technical report, London: Aeron. Res. Council (1977).

[11] S. Stanzl-Tschegg. Fracture mechanisms and fracture mechanics at ultrasonic frequencies. Fatigue Fract Engng Mater Struct **22** pp. 567–579 (1999).

[12] T. Li, J. Liu, Q. Y. Wang. Notch size effect on very high cycle fatigue behavior of 2024-T4 aluminum alloy. In 5th Int. Conf. Very High Cycle Fatigue, Berlin, pp. 327–332 (2011).

[13] Q. Y. Wang, T. Li, X. G. Zeng. Gigacycle fatigue behavior of high strength aluminum alloys. Procedia Engineering **2** pp. 65–70 (2010).

[14] H. Mayer, R. Schuller, M. Fitzka. Fatigue of 2024-T351 aluminium alloy at different load ratios up to 10^{10} cycles. International Journal of Fatigue **57** pp. 113–119 (2013).

[15] H. R. Mayer, M. Papakyriacou, R. Pippan, S. Stanzl-Tschegg. Influence of loading frequency on the high cycle fatigue properties of AlZnMgCu1.5 aluminium alloy. Materials Science and Engineering A **314** pp. 48–54 (2001).

[16] H.-J. Christ. Materialermüdung - Einführung und Überblick. In Ermüdungsverhalten metallischer Werkstoffe, edited by H.-J. Christ. Wiley-VCH (2009).

[17] H. Mughrabi. Specific features and mechanisms of fatigue in the ultrahigh-cycle regime. International Journal of Fatigue **28** 11 pp. 1501–1508 (2006).

[18] C. Bathias, L. Drouillac, P. le François. How and why the fatigue S–N curve does not approach a horizontal asymptote. International Journal of Fatigue **23** pp. 143–151 (2001).

[19] I. Marines. An understanding of very high cycle fatigue of metals. International Journal of Fatigue **25** 9-11 pp. 1101–1107 (2003).

[20] C. Berger, B. Pyttel, D. Schwerdt. Beyond HCF - is there a fatigue limit? Materialwissenschaft und Werkstofftechnik **39** 10 pp. 769–776 (2008).

[21] T. Sakai. Review and prospects for current studies on very high cycle fatigue of metallic materials for machine structural use. Journal of Solid Mechanics and Materials Engineering **3** 3 pp. 425–439 (2009).

[22] H. Mughrabi. Cyclic slip irreversibilities and the evolution of fatigue damage. Metallurgical and Materials Transactions A **40** 6 pp. 1257–1279 (2009).

[23] H. Mughrabi. Fatigue, an everlasting materials problem - still en vogue. Procedia Engineering **2** 1 pp. 3–26 (2010).

[24] S. X. Li. Effects of inclusions on very high cycle fatigue properties of high strength steels. International Materials Reviews (2011).

[25] M. Zimmermann. Diversity of damage evolution during cyclic loading at very high numbers of cycles. International Materials Reviews (2011).

[26] H. Mughrabi. Dislocations and properties of real materials. In Book No. 323, The institute of Metals, London, pp. 244–262 (1985).

[27] M. Klesnil, P. Lukáš. Fatigue of metallic materials. Elsevier, 2nd edition (1992).

[28] S. S. Manson. Behaviour of materials under conditions of thermal stress. Technical report, National Advisory Commision on Aeronautics (1954).

[29] L. F. Coffin. Transaction of the American Society of Mechanical Engineers **76** (1954).

[30] H. Mughrabi. On the life-controlling microstructural fatigue mechanisms in ductile metals and alloys in the gigacycle regime. Fatigue & Fracture of Engineering Materials & Structures **22** 7 pp. 633–641 (1999).

[31] S. Nishijima, K. Kanazawa. Stepwise S-N curve and fish-eye failure in gigacycle fatigue. Fatigue Fract. Engng. Mater. Struct. **22** pp. 601–607 (1999).

[32] H. Tian, M. Kirkham, L. Jiang, B. Yang, G.Wang, P. Liaw. A review of failure mechanisms of ultra high cycle fatigue in engineering materials. In 4th international conference on very high cycle fatigue (VHCF-4), Ann Arbor, pp. 437–444 (2007).

[33] S. Kovacs, T. Beck, L. Singheiser. Influence of mean stresses on fatigue life and damage of a turbine blade steel in the vhcf-regime. International Journal of Fatigue **49** pp. 90–99 (2013).

[34] Y. Murakami, T. Nomoto, T. Ueda, Y. Murakami. On the mechanism of fatigue failure in the superlong life regime (N>10^7 cycles). Part I: Influence of hydrogen trapped by inclusions. Fatigue and Fracture of Engineering Materials and Structures **23** 11 pp. 893–902 (2000).

[35] Y. Murakami, T. Nomoto, T. Ueda, Y. Murakami. On the mechanism of fatigue failure in the superlong life regime (N>10^7 cycles). Part II: A fractographic investigation. Fatigue and Fracture of Engineering Materials and Structures **23** 11 pp. 903–910 (2000).

[36] Y. Murakami, S. Matsuoka. Effect of hydrogen on fatigue crack growth of metals. Engineering Fracture Mechanics **77** 11 pp. 1926–1940 (2010).

[37] K. Shiozawa, Y. Morii, S. Nishino, L. Lu. Subsurface crack initiation and propagation mechanism in high-strength steel in a very high cycle fatigue regime. International Journal of Fatigue **28** 11 pp. 1521–1532 (2006).

[38] P. Grad, B. Reuscher, A. Brodyanski, M. Kopnarski, E. Kerscher. Mechanism of fatigue crack initiation and propagation in the very high cycle fatigue regime of high-strength steels. Scripta Materialia **67** 10 pp. 838–841 (2012).

[39] J. C. Grosskreutz, G. G. Shaw. Critical mechanisms in the development of fatigue cracks in 2024-t4 aluminium. Technical report (1968).

[40] T. Williams, J. Sova. Studies of fatigue damage in alluminium alloys. J. Sound. Vib. **16** p. 283 (1971).

[41] H. Mayer. Ultrasonic torsion and tension–compression fatigue testing: Measuring principles and investigations on 2024-t351 aluminium alloy. International Journal of Fatigue **28** 11 pp. 1446–1455 (2006).

[42] H. Mayer, S. Stanzl-Tschegg. High frequency torsional and axial fatigue loading of al 2024-T351. In Proc. of 6th Int. Fatigue Congress, Berlin, volume 1, pp. 691–696 (1996).

[43] H. Mayer. Fatigue crack growth and threshold measurements at very high frequencies. International Materials Reviews **44** 1 pp. 1–34 (1999).

[44] D. G. Harlow, J. Nardiello, J. Payne. The effect of constituent particles in aluminum alloys on fatigue damage evolution: Statistical observations. International Journal of Fatigue **32** 3 pp. 505–511 (2010).

[45] A. Bonakdar, F. Wang, J. J. Williams, N. Chawla. Environmental effects on fatigue crack growth in 7075 aluminum alloy. Metallurgical and Materials Transactions A: Physical Metallurgy and Materials Science **43** 8 pp. 2799–2809 (2012).

[46] M. S. Hunter, W. G. Fricke Jr. Metallographic aspects of fatigue behavior of aluminium. Technical report, American Society for Testing materials (1954).

[47] E. E. Gdoutos. Fracture mechanics, volume 2. Springer, Dorbrecht (2005).

[48] D. Gross, T. Seelig. Bruchmechanik, volume 4. Springer, Berlin (2011).

[49] C.-P. Fritzen. Grundlagen der Bruchmechanik. In Ermüdungsverhalten metallischer Werkstoffe, edited by H.-J. Christ. Wiley-VCH (2009).

[50] H. A. Richard, M. Sander. Ermüdungsrisse. Vieweg + Teubner, Wiesbaden (2009).

[51] P. C. Paris, M. P. Gomez, W. P. Anderson. A rational analytic theory of fatigue. The Trend in Engineering **13** pp. 9–14 (1961).

[52] H. Kitagawa, S. Takahashi. Applicability of fracture mechanics to very small cracks or the cracks in the early stages. In 2nd International Conference on Mechanical Behavior of Materials, pp. 627–631 (1976).

[53] M. El Haddad, T. Topper, K. Smith. Prediction of non propagating cracks. Eng Fract Mech **11** pp. 573–584 (1979).

[54] H. Neuber. Kerbspannungslehre, volume 4. Springer, Berlin (2001).

[55] D. L. Du Quesnay, M. T. Yu, T. H. Topper. An analysis of notch-size effects at the fatigue limit. Journal of Testing and Evaluation **16** 4 pp. 375–385 (1988).

[56] M. Talia, J. E. Talia. Crack propagation modeling for surface generated scratches in al 2024-T3 clad alloy. Journal of the Mechanical Behavior of Materials **8** 2 pp. 117–140 (1997).

[57] E. J. Dolley, B. Lee, R. P. Wei. The effect of pitting corrosion on fatigue life. Fatigue & Fracture of Engineering Materials & Structures **23** 7 pp. 555–560 (2000).

[58] K. K. Sankaran, R. Perez, K. V. Jata. Effects of pitting corrosion on the fatigue behavior of aluminum alloy 7075-T6: modeling and experimental studies. Materials Science and Engineering A **297** (2001).

[59] Q. Wang, N. Kawagoishi, Q. Chen. Effect of pitting corrosion on very high cycle fatigue behavior. Scripta Materialia **49** 7 pp. 711–716 (2003).

[60] K. Genel. The effect of pitting on the bending fatigue performance of high-strength aluminum alloy. Scripta Materialia **57** 4 pp. 297–300 (2007).

[61] M. Zimmermann, H. J. Christ. Influence of macroscopic and microscopic notch effects on the vhcf behaviour of a precipitation-hardenend aluminium alloy. In 4th international conference on very high cycle fatigue (VHCF-4), Ann Arbor, pp. 295–301 (2007).

[62] B. Pyttel, B. Kaiser, D. Schwerdt, T. Trossmann. Ermüdungsverhalten ausgewählter Werkstoffe und Bauteile bei sehr hohen Schwingspielzahlen. Materialwissenschaft und Werkstofftechnik **37** 10 pp. 820–832 (2006).

[63] C. Berger, B. Pyttel, T. Trossmann. Very high cycle fatigue tests with smooth and notched specimens and screws made of light metal alloys. International Journal of Fatigue **28** 11 pp. 1640–1646 (2006).

[64] S. E. Stanzl, E. Tschegg. Influence of environment on fatigue crack growth in the threshold region. Acta Metall. **29** pp. 21–32 (1981).

[65] S. E. Stanzl, H. R. Mayer, E. Tschegg. The influence of air humidity on near-threshold fatigue crack growth of 2024-T3 aluminum alloy. Material Science and Engineering **A147** pp. 45–54 (1991).

[66] N. Ranganathan, B. Bouchet, J. Petit. Fractographic aspects of the effect of the environment on the fatigue propagation mechanism in a high-strength aluminum alloy, pp. 424–446. Fractography of modern engineering materials: Composites and Metals. ASTM STP 948 (1987).

[67] H. Mughrabi. On multi-stage fatigue life diagrams and the relevant life-controlling mechanisms in ultrahigh-cycle fatigue. Fatigue & Fracture of Engineering Materials & Structures **25** pp. 755–764 (2002).

[68] H. Xue, Q. Tao, W. Chen, C. Bathias. Analysis of fatigue crack initiation and size effect on fatigue life of a cast aluminum alloy in very long life cycles. In 6th international conference on very high cycle fatigue (VHCF-6), Chengdu (2014).

[69] J. E. LaRue, S. R. Daniewicz. Predicting the effect of residual stress on fatigue crack growth. International Journal of Fatigue **29** 3 pp. 508–515 (2007).

[70] B. Leis. Effect of surface conditioning and processing on fatigue performance, p. 19. ASM handbook, fatigue and fracture (1997).

[71] SAE fatigue design and evaluation steering committee. Fatigue design handbook. Society of automotive Engineers, 3rd edition (1997).

[72] R. I. Stephens, A. Fatemi, R. R. Stephens, H. Fuchs. Metal fatigue in engineering. Wiley and sons, New York (2001).

[73] A. Todoroki, H. Kobayashi. Prediction of fatigue crack growth rate in residual stress fields. Key Engineering Materials **51-52** pp. 367–372. Cited By (since 1996):1 Export Date: 15 January 2014 Source: Scopus (1991).

[74] K. N. Smith, P. Watson, T. H. Topper. A stress-strain function for the fatigue of metals. Journal of Materials **4** pp. 767–778 (1970).

[75] B. P. Haigh. Report on alternating stress tests of a sample of mild steel, BASC Rep. **85** pp. 163–170 (1915).

[76] T. Shimokawa, Y. Hamaguchi. Relationship between fatigue life distribution, notch configuration, and S-N curve of a 2024-T4 aluminum alloy. Journal of Engineering Materials and Technology, Transactions of the ASME **107** 3 pp. 214–220 (1985).

[77] J. X. Li, T. Zhai, M. D. Garratt, G. H. Bray. Four-point-bend fatigue of AA 2026 aluminum alloys. Metallurgical and Materials Transactions A: Physical Metallurgy and Materials Science **36** 9 pp. 2529–2539 (2005).

[78] S. A. Fawaz, J. J. M. De Rijck. A thin-sheet, combined tension and bending specimen. Experimental Mechanics **39** 3 pp. 171–176 (1999).

[79] M. Benachour, A. Hadjoui, M. Benguediab, N. Benachour. Effect of the amplitude loading on fatigue crack growth. Procedia Engineering **2** 1 pp. 121–127 (2010).

[80] C.-M. Suh, S.-H. Nahm, M.-S. Suh, Y.-S. Suh, Y.-S. Pyun, H.-K. Yoon. Fatigue characteristics of UNSM treated aluminum alloy (A7075-T651) using ultrasonic (20 kHz) and rotary bending (53 Hz) fatigue testing machines. In 6th international conference on very high cycle fatigue (VHCF-6), Chengdu (2014).

[81] Y. G. Wang, Z. X. Jiang, L. L. Wang. Dynamic tensile fracture behaviours of selected aluminum alloys under various loading conditions. Strain **49** 4 pp. 335–347 (2013).

[82] E. Haibach. Ermüdungsfestigkeit - Verfahren und Daten zur Bauteilberechnung. VDI, Düsseldorf (2002).

[83] M. Zimmermann. Statistische Auswertung von Dauerschwingversuchen. In Ermüdungsverhalten metallischer Werkstoffe, edited by H.-J. Christ. Wiley-VCH (2009).

[84] D. Dengel. Die $\arcsin\sqrt{P}$-Transformation – ein einfaches Verfahren zur graphischen und rechnerischen Auswertung geplanter Wöhlerversuche. Journal of Materials Technology **6** 8 pp. 253–288 (1975).

[85] C. Bathias. Piezoelectric fatigue testing machines and devices. International Journal of Fatigue **28** 11 pp. 1438–1445 (2006).

[86] L. E. Willertz. Ultrasonic fatigue. International metals reviews **25** 2 pp. 65–78 (1980).

[87] S. E. Stanzl-Tschegg. Ultrasonic fatigue. In 6th Int. Fatigue Congress, edited by G. Lütjering, H. Nowack, volume III, pp. 1887–1898 (1996).

[88] C. Bathias, N. Jingang. Determination of fatigue limit between 10^5 and 10^9 cycles using an ultrasonic fatigue device. In ASTM Special Technical Publication, 1211, pp. 141–152 (1993).

[89] K. Ishii, Y. Kaga, T. Ono. Internal friction in carbon steels under high loading frequencies. Nippon Kikai Gakkai Ronbunshu, A Hen/Transactions of the Japan Society of Mechanical Engineers, Part A **56** 527 pp. 1672–1676 (1990).

[90] Puskár. Ultrasonic fatigue testing equipment and new procedures for complex material evaluation. Ultrasonics **31** (1993).

[91] M. Koster, G. Wagner, F. Walther, D. Eifler. New measuring methods for the fatigue assessment of metals in the very high cycle regime. In 4th international conference on very high cycle fatigue (VHCF-4), Ann Arbor, pp. 347–352 (2007).

[92] A. Kumar, C. J. Torbet, J. W. Jones, T. M. Pollock. Nonlinear ultrasonics for in situ damage detection during high frequency fatigue. Journal of Applied Physics **106** 2 p. 024904 (2009).

[93] ANSYS® Academic Research, Release 15.0.

[94] A. Blanche, C. Wang, N. L. Phung, N. Ranc, V. Favier, D. Wagner, C. Bathias, A. Chrysochoos. Dissipation in very high cycle fatigue for single phase ductile metals: comparison between b.c.c. and f.c.c. structures. In 6th international conference on very high cycle fatigue (VHCF-6), Chengdu (2014).

[95] D. Roggenkamp, W. Jessen, W. Li, M. Klaas, W. Schröder. Experimental investigation of turbulent boundary layers over transversal moving surfaces. (submitted) (2014).

[96] W. Li, W. Jessen, D. Roggenkamp, M. Klaas, W. Silex, M. Schiek, W. Schröder. Turbulent drag reduction by spanwise traveling ribbed surface waves. (submitted) (2014).

[97] A. Elmustafa, J. Eastman, M. Rittner, J. Weertman, D. Stone. Indentation size effect: large grained aluminum versus nanocrystalline aluminum-zirconium alloys. Scripta Materialia **43** 10 pp. 951–955 (2000).

[98] A. Iost, R. Bigot. Indentation size effect: Reality or artefact? Journal of Materials Science **31** 13 pp. 3573–3577 (1996).

[99] A. Elmustafa, D. Stone. Nanoindentation and the indentation size effect: Kinetics of deformation and strain gradient plasticity. Journal of the Mechanics and Physics of Solids **51** 2 pp. 357–381 (2003).

[100] A. Elmustafa, D. Stone. Stacking fault energy and dynamic recovery: Do they impact the indentation size effect? Materials Science and Engineering A **358** 1-2 pp. 1–8 (2003).

[101] D. Stegall, A. Elmustafa. Investigation of the indentation size effect in FCC metals using activation volume analysis. volume 2, pp. 747–752 (2012).

[102] V. M. Hauck, E. Macherauch. Advances in x-ray analysis (1983).

[103] E. Macherauch. X-ray stress analysis. Experimental Mechanics **6** pp. 140–153 (1966).

[104] J. Dix, E.H., F. Keller. Mining and Metallurgy **9** p. 327 (1929).

[105] G. Petzow. Metallographic etching: techniques for metallography, ceramography, plastography. ASM international (1999).

[106] E. A. Starke Jr, J. T. Staley. Application of modern aluminum alloys to aircraft. Progress in Aerospace Sciences **32** 2–3 pp. 131–172 (1996).

[107] M. E. Fine. Precipitation hardening of aluminum alloys. Metallurgical Transactions A **6** 4 pp. 625–630 (1975).

[108] A. Baldantoni. On the microstructural changes during the retrogression and re-aging of 7075 type aluminium alloys. Materials Science and Engineering **72** 1 pp. L5 – L8 (1985).

[109] Alcoa Mill Products INC. Alloy 2024 – sheet and plate (technical data sheet) (2014).

[110] Alcoa Mill Products INC. Alloy 7075 – plate and sheet (technical data sheet) (2014).

[111] C. Kammer. Aluminium Taschenbuch: Band 1: Grundlagen und Werkstoffe. Alu Media, Düsseldorf, 16th edition (2009).

[112] G. Drossel, S. Friedrich, C. Kammer, W. Lehnert, O. Liesenberg. Aluminium Taschenbuch: Band 2: Umformung von Aluminium-Werkstoffen, Gießen von Aluminium-Teilen, Oberflächenbehandlung von Aluminium, Recycling und Ökologie. Alu Media, Düsseldorf, 16th edition (2009).

[113] N. D. Alexopoulos. On the corrosion-induced mechanical degradation for different artificial aging conditions of 2024 aluminum alloy. Materials Science and Engineering A **520** pp. 40–48 (2009).

[114] C. Vargel. Corrosion of Aluminium. Elsevier (2004).

[115] D. Dzhurinskiy, E. Maeva, E. Leshchinsky, R. Maev. Corrosion protection of light alloys using low pressure cold spray. Journal of Thermal Spray Technology **21** 2 pp. 304–313 (2012).

[116] N. Birbilis, R. G. Buchheit. Electrochemical characteristics of intermetallic phases in aluminum alloys an experimental survey and discussion. Journal of The Electrochemical Society **152** 4 pp. B140–B151 (2005).

[117] C. Subramanian, K. N. Strafford, T. P. Wilks, L. P. Ward. On the design of coating systems: Metallurgical and other considerations. Journal of Materials Processing Technology **56** 1–4 pp. 385–397 (1996).

[118] S. Stewart, R. Ahmed. Rolling contact fatigue of surface coatings—a review. Wear **253** 11–12 pp. 1132–1144 (2002).

[119] H. Herman, S. Sampath, R. McCune. Thermal spray: Current status and future trends. MRS Bulletin **25** 7 pp. 17–25 (2000).

[120] J. Kawakita, S. Kuroda, T. Fukushima, T. Kodama. Development of dense corrosion resistant coatings by an improved hvof spraying process. Science and Technology of Advanced Materials **4** 4 pp. 281–289 (2003).

[121] J. Xu, W. Liu, Y. Kan, M. Zhong. Microstructure and wear properties of laser cladding ti–al–fe–b coatings on aa2024 aluminum alloy. Materials & Design **27** 5 pp. 405–410 (2006).

[122] K. Uenishi, K. F. Kobayashi. Formation of surface layer based on al3ti on aluminum by laser cladding and its compatibility with ceramics. Intermetallics **7** 5 pp. 553–559 (1999).

[123] F. Audebert, R. Colaço, R. Vilar, H. Sirkin. Laser cladding of aluminium-base quasicrystalline alloys. Scripta Materialia **40** 5 pp. 551–557 (1999).

[124] F. Findik. Recent developments in explosive welding. Materials & Design **32** 3 pp. 1081–1093 (2011).

[125] M. Acarer, B. Gülenç, F. Findik. Investigation of explosive welding parameters and their effects on microhardness and shear strength. Materials & Design **24** 8 pp. 659–664 (2003).

[126] F. Grignon, D. Benson, K. S. Vecchio, M. A. Meyers. Explosive welding of aluminum to aluminum: analysis, computations and experiments. International Journal of Impact Engineering **30** 10 pp. 1333–1351 (2004).

[127] J. Liu, M. Li, S. Sheu, M. E. Karabin, R. W. Schultz. Macro- and microsurface engineering to improve hot roll bonding of aluminum plate and sheet. Materials Science and Engineering: A **479** 1–2 pp. 45–57 (2008).

[128] J. Liu, M. Li, S. Sheu, M. E. Karabin, R. W. Schultz. Effect of surface engineering on roll bonding of the AA 2024 Alclad plate, TMS Light Metals (2008).

[129] H. Yan, J. G. Lenard. A study of warm and cold roll-bonding of an aluminium alloy. Materials Science and Engineering: A **385** 1–2 pp. 419–428 (2004).

[130] F. P. Bowden, D. Tabor. The Friction and Lubrication of Solids. Clarendon Press, Oxford (1950).

[131] N. Bay. Cold welding: Part 1. characteristics, bonding mechanisms, bond strength. Metal construction **18** 6 pp. 369–372 (1986).

[132] G. Hirt, M. Thome. Rolling of functional metallic surface structures. CIRP Annals - Manufacturing Technology **57** pp. 317–320 (2008).

[133] G. Hirt, M. Thome. Large area rolling of functional metallic micro structures. Prod. Eng. Res. Devel. **1** pp. 351–356 (2007).

[134] J. Pöplau, S. Stille, T. Romans, T. Beck, L. Singheiser, G. Hirt. The inluence of process parameters on the forming of riblets during riblet rolling. Key Engineering Materials **611-612** pp. 715–722 (2014).

[135] S. Stille, J. Pöplau, T. Beck, M. Bambach, G. Hirt, L. Singheiser. Very high cycle fatigue behavior of riblet structured alclad 2024 thin sheets. International Journal of Fatigue **63** pp. 183–190 (2014).

[136] A. Merati. A study of nucleation and fatigue behavior of an aerospace aluminum alloy 2024-T3. International Journal of Fatigue **27** 1 pp. 33–44 (2005).

[137] S. Usami. Applications of threshold cyclic-plastic-zone-size criterion to some fatigue limit problems. In Int. Symposium on Fatigue Thresholds, pp. 205–238 (1981).

[138] C. Moosbrugger (editor). Atlas of Stress-Strain curves. ASM International, 2nd edition (2002).

[139] S. D. Henry, F. Reidenbach (editors). Fatigue Data Book: Light Structural Alloys. ASM International (1995).

List of figures

List of tables

Band / Volume 248
Stoffliche Charakterisierung radioaktiver Abfallprodukte durch ein Multi-Element-Analyseverfahren basierend auf der instrumentellen Neutronen-Aktivierungs-Analyse – MEDINA –
A. W. Havenith (2015), 311 pp
ISBN: 978-3-95806-033-3

Band / Volume 249
Quantitative Two-Layer Inversion and Customizable Sensor-Array Instrument for Electromagnetic Induction based Soil Conductivity Estimation
A. T. Mester (2015), viii, 119 pp
ISBN: 978-3-95806-035-7

Band / Volume 250
Partial Neutron Capture Cross Sections of Actinides using Cold Neutron Prompt Gamma Activation Analysis
C. Genreith (2015), vii, 166, XXXII pp
ISBN: 978-3-95806-036-4

Band / Volume 251
Long Term Aerosol Composition Measurements at the CESAR Tower at Cabauw, NL
P. Schlag (2015), iii, 228 pp
ISBN: 978-3-95806-037-1

Band / Volume 252
Modellbasierte Spezifikationsmethodik zur effizienten Systementwicklung von Brennstoffzellenantrieben
R. Biurrun Sotelo (2015), 255 pp
ISBN: 978-3-95806-038-8

Band / Volume 253
Three-dimensional ray-tracing simulations of convective gravity waves
S. Kalisch (2015), iii, 183 pp
ISBN: 978-3-95806-040-1

Band / Volume 254
First-Principles Study on Pyrites and Marcasites for Photovoltaic Application
T. Schena (2015), 206 pp
ISBN: 978-3-95806-041-8

Band / Volume 255
Glass-Ceramic Sealant Reinforcement for High-Temperature Applications
B. Cela Greven (2015), xi, 119 pp
ISBN: 978-3-95806-042-5

Band / Volume 256
Entwicklung planarer $Ba_{0,5}Sr_{0,5}Co_{0,8}Fe_{0,2}O_{3-\delta}$-Membranmodule zur Sauerstoffabtrennung und Analyse ihres Transportverhaltens
P. Niehoff (2015), VIII, 134 pp
ISBN: 978-3-95806-044-9

Band / Volume 257
Extension of the Reactor Dynamics Code MGT-3D for Pebble-bed and Block-type High-Temperature-Reactors
D. Shi (2015), x, 162 pp
ISBN: 978-3-95806-045-6

Band / Volume 258
Failure Analysis of Thin Film Solar Modules using Lock-in Thermography
M. Siegloch (2015), XIII, 131 pp
ISBN: 978-3-95806-047-0

Band / Volume 259
Relation between growth rate, material quality, and device grade condition for intrinsic microcrystalline silicon:
From layer investigation to the application to thin-film tandem solar cells
S. Michard (2015), vi, 184 pp
ISBN: 978-3-95806-048-7

Band / Volume 260
Quantitative analysis of spatially resolved electroluminescence of Cu(In,Ga)Se_2 and a-Si:H thin-film solar cells and modules
T. Tran (2015), iii, 161 pp
ISBN: 978-3-95806-050-0

Band / Volume 261
Influence of the surface composition and morphology on the reflectivity of diagnostic mirrors in a fusion reactor
M. Matveeva (2015), 158 pp
ISBN: 978-3-95806-051-7

Band / Volume 262
Very High Cycle Fatigue Behavior of Riblet Structured High Strength Aluminum Alloy Thin Sheets
S. Stille (2015), XII, 123 pp
ISBN: 978-3-95806-054-8

Energie & Umwelt /
Energy & Environment
Band / Volume 262
ISBN 978-3-95806-054-8